Université de Sherbrooke

Quantification of atherosclerotic plaque in the elderly with positron emission
tomography/computed tomography

Par

Mamdouh Saud A. Al-Enezi
Programme de sciences des radiations et imagerie biomédicale

Thèse présentée à la Faculté de médecine et des sciences de la santé
en vue de l'obtention du grade de philosophiae doctor (Ph.D.)
en sciences des radiations et imagerie biomédicale

Sherbrooke, Québec, Canada
mars 2021

Membres du jury d'évaluation

Jean-Francois Carrier, Ph.D., Département de radiologie, radio-oncologie et médecine
nucléaire, Faculté de médecine, Université de Montréal.

Réjean Fontaine, Ph.D., Faculté de génie, Département de génie électrique et de génie
informatique, Université de Sherbrooke.

Kevin Whittingstall, Ph.D., Programme de sciences des radiations et imagerie
biomédicale.

M'hamed Bentourkia, Ph.D., Programme de sciences des radiations et imagerie
biomédicale.

Praises and thankful to Almighty God.

*Challenges are what make life interesting,
overcoming them is what makes life meaningful.*
Joshua J. Marine

RÉSUMÉ

Quantification de la plaque athérosclérotique chez les personnes âgées avec la tomographie d'émission par positrons et la tomodensitométrie

Par

Mamdouh Saud A. Al-Enezi

Programme de sciences des radiations et imagerie biomédicale

Thèse présentée à la Faculté de médecine et des sciences de la santé en vue de l'obtention du diplôme de philosophiae doctor (Ph.D.) en science des radiations et imagerie biomédicale, faculté de médecine et des sciences de la santé, université de Sherbrooke, Sherbrooke, Québec, Canada, J1H 5N4

L'athérosclérose est une maladie cardiovasculaire inflammatoire qui est devenue la première cause de morbidité et de mortalité dans les pays développés et parmi les principales causes d'invalidité au monde. Elle se caractérise par l'épaississement de la paroi vasculaire artérielle suite à l'accumulation de lipides et le dépôt d'autres substances au niveau de l'intima (endothélium) pour former la plaque d'athérome. Avec l'âge, cette plaque peut grossir, se calcifier et ainsi rétrécir le calibre de l'artère pour diminuer son débit et à un stade avancé de la maladie, elle peut se rompre et obstruer les petites artères dans n'importe quelle partie du corps causant des complications aigues, y compris la mort soudaine.

L'objectif de cette thèse est de pouvoir détecter l'inflammation de la plaque athérosclérotique quantitativement avec la TEP/TDM dans le but de prévenir son détachement. Les mesures avec la TDM et la TEP avec le ^{18}F-FDG ont été acquises chez des sujets humains âgés de 65 à 85 ans. Des analyses quantitatives ont été conduites sur les images de TDM en fonction de l'intensité et des étendues des calcifications, et sur les images de la TEP pour évaluer le métabolisme des plaques. L'effet des traitements par les statines a aussi été étudié. Au-delà la couverture de cette étude de façon détaillée au niveau physiologique en corrélant différents paramètres des plaques, et au niveau méthodologique en utilisant de nouvelles approches pour l'analyse pharmacocinétique, il en ressort principalement la suggestion de la détection de la vulnérabilité de la plaque artérielle par la TDM, plus disponible et moins coûteuse, en remplacement des analyses biochimiques, surtout la protéine C-réactive (CRP) considérée être la méthode standard.

Mots clés : TEP/TDM; Athérosclérose; Inflammation; Calcification; Plaque; Plaque non calcifiée; ^{18}F-FDG; ^{18}F-NaF.

SUMMARY

Quantification of atherosclerotic plaque in the elderly with positron emission tomography/computed tomography

By

Mamdouh Saud A. Al-Enezi

Program of radiation sciences and biomedical imaging

Thesis presented at the Faculty of medicine and health sciences for the obtention of Doctor degree diploma philosophiae doctor (Ph.D.) in Radiation sciences and biomedical imaging, Faculty of medicine and health sciences, Université de Sherbrooke, Sherbrooke, Québec, Canada, J1H 5N4

Atherosclerosis is an inflammatory cardiovascular disease considered the leading cause of morbidity and mortality in developed countries and among the leading causes of disability worldwide. It is characterized by the thickening of the arterial vascular wall due to the accumulation of lipids and the deposition of other substances in the intima (endothelium) to form atheroma plaque. With age, this plaque can grow larger, calcify and thus narrow the size of the artery to decrease blood flow and at an advanced stage of the disease, it can rupture, be transported by blood and block the small arteries in any part of the body causing acute complications, including sudden death.

The objective of this thesis was to be able to detect the inflammation of the atherosclerotic plaque quantitatively with PET/CT in order to prevent its detachment. Measurements with CT and PET with ^{18}F-FDG were acquired in human subjects aged 65 to 85 years. Quantitative analyzes were performed on CT images based on the intensity and extent of calcifications, and on PET images to assess plaque metabolism. The effect of statin treatments has also been studied. Beyond the coverage of this study in a detailed manner at the physiological level by correlating different parameters of the plaques, and at the methodological level by using new approaches for pharmacokinetic analysis, it mainly emerges the suggestion for the detection of the vulnerability of the arterial plaque by CT alone, more available and less expensive, replacing biochemical analyzes, especially C-reactive protein (CRP) considered to be the standard method.

Keywords: PET/CT; Atherosclerosis; Inflammation; Calcification; Plaque; Non-calcified plaque; ^{18}F-FDG; ^{18}F-NaF.

TABLE OF CONTENTS

LIST OF FIGURES

LIST OF TABLES

LIST OF ABBREVIATIONS

^{18}F-FDG	^{18}F-fluorodeoxyglucose
^{18}F-NaF	^{18}F-Sodium Fluoride
CRP	C-reactive Protein
CT	Computed Tomography
CTA	Computed tomography angiography
DSA	Digital Subtraction Angiography
FA	Factor Analysis
FUR	Fractional Uptake Rate
HDL	High-Density-Lipoprotein
IF	Input Function
IVUS	Intravascular Ultrasound
Ki	Net Flux Rate
LDL	Low-Density-Lipoprotein
MMP	Metalloproteinase
MRG	Metabolic Rate of Glucose
MRI	Magnetic Resonance Imaging
NCP	Non-calcified plaque
NIRS	Near Infrared Spectroscopy
OCT	Optical Coherence Tomography
PET	Positron emission tomography
PVE	Partial Volume Effect
RC	Recovery Coefficient
SMC	Smooth Muscle Cell
SPECT	Single Photon Emission Computed Tomography
SUV	Standard Uptake Value
TAC	Time Activity Curve
TBR	Tissue to Background Ratio
TBV	Tissue Blood Volume
WOBS	Modified 2-tissue compartmental modeling without blood sampling
SS	Single spot of calcification
MS	Multi-spots of calcification

WT	Wall thickness
DWR	Diameter to wall thickness ratio
NCST	Total-non-calcified segments
CST	Total calcified segments
NCSN	Normal-non-calcified segments

1. INTRODUCTION

Atherosclerosis is an old disease recognized since antiquity. Leonardo da Vinci (1452–1519) is among the first who described atherosclerosis disease by stating that "vessels in the elderly restrict the transit of blood through thickening of the tunics." (Davies and Eollman, 1996). It was then known as atheroma, a Latin word which was first used by Albrecht von Halles in 1755 to designate the plaque attached to the innermost layer of the arterial wall (Meyer, 2001). In 1768 the British William Heberden described angina symptoms and in 1799 his compatriot Caleb Hillier Parry recognized the cause of angina as impairment of the vascular supply by conducting experiments on sheep (Slijkhuis, Mali and Appelman, 2009). The word atherosclerosis, however, is a Greek word introduced by Marchand in 1940 (Konstantinov, Mejevoi and Anichkov, 2006) to describe the association of fatty degeneration and vessel stiffening which are the two main plaque components, because of this, the name "Atherosclerosis" is nowadays the mostly used term. "Athero" means gruel or porridge and it refers to soft lipid rich material in the center of the plaque (atheroma) and sclerosis means scarring and refers to connective tissue in the plaque (Virmani *et al.*, 2006). Atherosclerosis was generally identified as a stenosis phenomenon.

Flow-limiting stenosis is affected by both the outward and inward progressive growth of the plaque. This is known as an arterial remodeling and it was first explored by Seymour Glagov (Glagov *et al.*, 1987), who demonstrated that as long as the stenosis of lumen is less than 30-40% of lumen area, the lumen area is independent of the stenosis "plaque", suggesting a correspondence enlargement of the arterial lumen (remodeling). However, the arterial enlargement would not pace with the increased stenosis afterword.

In physiological point of view, atherosclerosis has been described throughout different theories starting from thrombogenic theory that was developed by Carl von Rokitansky based on the roles of thrombosis and platelets in the initiation of atherosclerosis (Mayerl *et al.*, 2006). The second theory was a lipid infiltration theory by Anitschkov and Chalatov, that is based on the plasma lipids and their contribution in the initiation of plaques (Westerlind *et al.*, 2019). The advanced theories incorporated the role of the immune response with a complexity processes involving various types of immune cells (inflammation) including

monocyte-derived macrophage, which forms foam cells in the arterial intima, T lymphocytes, mast cells, coagulation proteins and atherosclerosis signaling molecules, all of which change over time. Inflammatory theory proposed by Rudolf Virchow was stating that atherosclerotic plaque is a result of an inflammatory process within the intima (Westerlind *et al.*, 2019). The response-to-injury theory by Russel Ross, which is the last and most accepted theory stated that the endothelial layer injury is the first step in atherosclerosis, which could be caused by several factors including hyperlipidemia and shear stress in hypertension. Focal endothelium damage causes massive infiltration of platelet factors, plasma lipoproteins (low density lipoprotein "LDL") and others in the circulation at the site of injury leading to focal proliferation of smooth muscle cells (SMCs) and deposition of oxidized LDL (ox-LDL). Regression of the lesion occurs only if there is a balance between injury and tissue response, while the imbalance would lead to the progression. This imbalance caused by chronic inflammatory response (gradual onset and long duration) which results in an advanced and complicated lesion (Ross, 1999).

Summarily, atherosclerosis is a disease characterized by chronic inflammation of the arterial wall. The inflammation is initiated as a result of endothelial dysfunction, in the response to platelets aggregation and subendothelial retention of plasma-derived apolipoprotein B containing lipoproteins (oxidatively modified) (Yia-Herttuala *et al.*, 1989; Williams and Tabas, 1995, 1998; Tabas, Williams and Borén, 2007; DuRose *et al.*, 2012). The consequence is atherosclerotic plaque formation and progression (Figure 1.1).
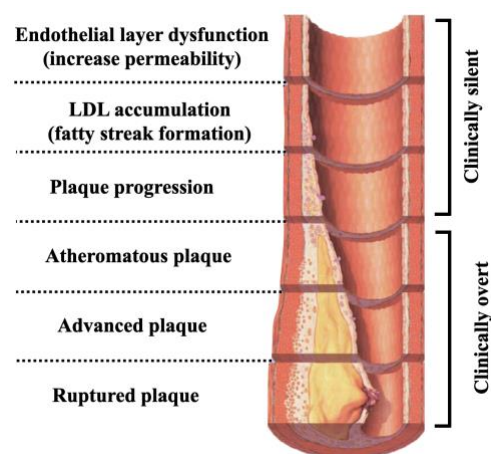
Figure 1.1 A display of atherosclerosis progression steps (adapted from https://en.wikipedia.org/wiki/Atherosclerosis).

Parallel with efforts made in studying a cause of plaque formation and since the plaque could be asymptomatic or symptomatic under specific physiological and mechanical conditions (Figure 1.2), vulnerable plaque concept was introduced as non-obstructive lesion (Muller, Tofler and Stone, 1989).
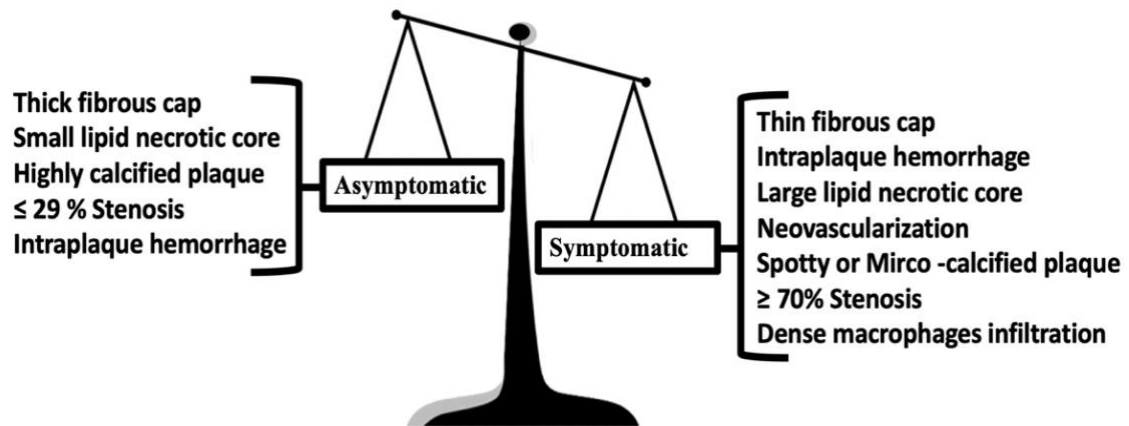
Figure 1.2 Signs of asymptomatic and symptomatic atherosclerotic plaque.

The vulnerable plaque is characterized by a large necrotic core with a thin cap (Virmani *et al.*, 2006), macrophage infiltration, outward remodeling, micro-calcification, intraplaque neovascularization (Dweck *et al.*, 2016a), hemorrhage (Michel *et al.*, 2014), and a large stenosis > 70% (Narula *et al.*, 2013; Hori *et al.*, 2019). Histological studies of coronary arteries extracted from patients who passed-away of acute atherosclerotic coronary syndromes demonstrated that the vulnerable plaques are also characterised by the presence of macrophages, lymphocytes, and mast cells (Kohichi *et al.*, 1985). Their presence indicates the ongoing inflammatory cascade, which could be a cause of disrupted plaque (Figure 1.3).
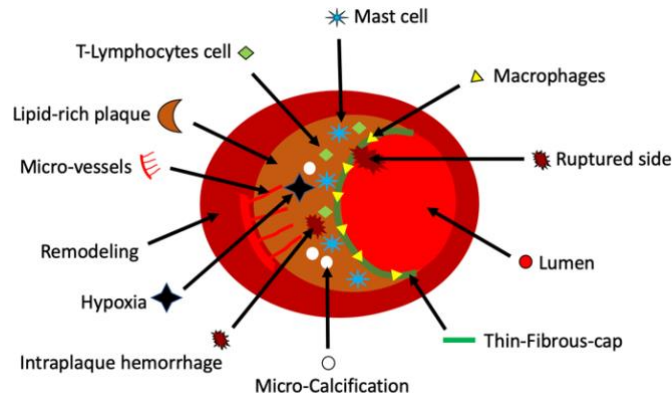
Figure 1.3 Major vulnerable plaque characteristics.

Atherosclerosis remains a major cause of morbidity and mortality worldwide (Figure 1.4), despite tremendous effort of diagnosing, prevention and treatment (Benjamin et al., 2018). The key step toward the prevention of atherosclerosis complication and yielding better outcomes for patients is the early detection and high-risk plaque identification. Identifying high risk plaque went through several approaches including risk stratification, presence, and level of specific biomarkers as well as imaging some crucial features, such as plaque calcification.
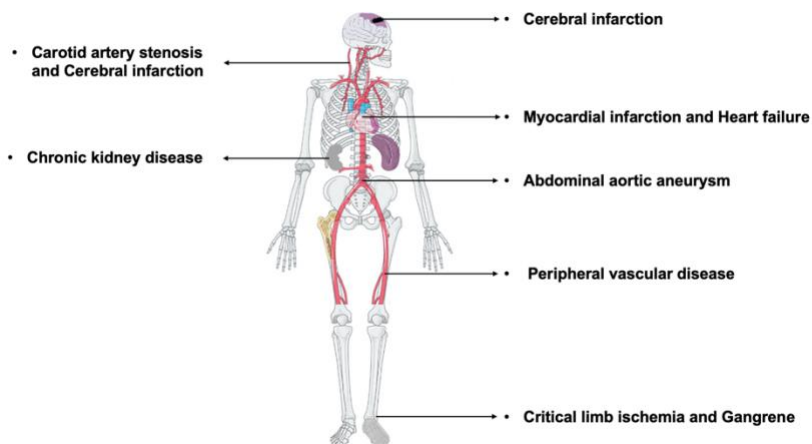
Figure 1.4 A display of major complication sites of Atherosclerosis, adapted from (Calcagno and Fayad, 2020) with permission from Edizioni Minerva Medica.

1.1 Risk scores

The accurate identification of individuals at risk is a fundamental goal to prevent such complications and offers an appropriate treatment in an appropriate time, based upon known

risk factors. In this context, there are about 110 different risk score methods (Liew, Doust and Glasziou, 2011; Ruwanpathirana, Owen and Reid, 2015), all of which depend upon some traditional factors such as smoking, high blood pressure, and high cholesterol.

The reference standard score is Framingham Risk Score (FRS), which was first published in 1976 (Kannel, McGee and Gordon, 1976) to measure the risk estimation over 10 years. However, all risk factors including FRS are predictors of cardiovascular events in 10 to 30 years and not at the time of examination and do not perform well for an individual patient.

1.2 Biomarkers

Atherosclerosis is a systemic inflammatory disease (Ross, 1999), where in every step of atherosclerosis process, the immune cells are directly involved. Therefore, a wide variety of systemic biomarkers are available for atherosclerosis. The measure of biomarkers in the blood is easy with low cost and widely available. These particular merits make them of great interest for atherosclerosis and efficacy of therapy, thus, there are on regular basis new biological markers being discovered. The most popular are individually discussed in the next paragraphs.

Lipoprotein: the initial step of atherosclerotic plaque formation is a focal accumulation of lipids. The lipids usually carried in association with a specific protein called apoprotein and the mix of those known as lipoprotein. The lipoproteins are categorised based on the density as very-low-density lipoprotein (VLDL), low-density lipoprotein (LDL) and high-density lipoprotein (HDL).

Myeloperoxidase and triglycerides: the role of oxidized LDL in the formation of atherosclerotic plaque was validated (Goldstein and Brown, 2015) and shown to be internalized by macrophage scavengers which led to the formation of foam cells (Birukov, 2006). Myeloperoxidase levels was shown to be linked to elevated oxidative stress, inflammation and the mortality rate (Ramachandra *et al.*, 2020). Elevated triglycerides were also suggested to be another independent risk factor for atherosclerosis complication (Sarwar *et al.*, 2007).

High-density lipoprotein (HDL): HDL is thought as a protective by promoting lipid efflux and reduce plaque size (Linton *et al.*, 1950). Adiponectin may also be considered a

protective against atherosclerosis by decreasing endothelial damage (Ekmekci and Ekmekci, 2006).

C-reactive protein (CRP): CRP is a plasma protein involved in acute inflammatory response and it is extensively used as a marker for inflammation and CRP has been found colocalized with macrophages in vitro and in vivo study of atherosclerotic lesions in humans (Torzewski *et al.*, 2000). In the analysis of 47 patients of unstable angina, CRP and leptin were reported an independent predictor for complex lesion morphology (Dubey *et al.*, 2008). CRP was also shown to be independent of the LDL level for an increased risk of cardiovascular events. However, it lacks the specificity for inflammation of atherosclerotic plaques. Also, CRP influenced by substantial heritability and can have dual-phase activities for inflammation (pro- and anti-inflammatory) (Singh *et al.*, 2008). Interleukin (IL)-1 and IL-6 are of the main initiator for CRP secretion (Lind, 2003). IL-6 was also reported to be an independent predictor of plaque progression (Eltoft *et al.*, 2018).

Matrix metalloproteinase (MMPs): MMPs secretion is associated with the recruitment of macrophages, mast cells as well as ox-LDL during the atherosclerotic plaque progression (Newby, 2005; Müller *et al.*, 2014). The serum level of MMP-1, MMP-9, MMP-12 and MMP-14 were reported to be significantly elevated in vulnerable plaques compared to the stable plaques (Müller *et al.*, 2014). Additionally, elevated serum of MMP-1 was reported to serve as a predictor of advanced coronary atherosclerosis with more specificity compared to CRP (Hwang *et al.*, 2009).

Inflammatory cells such as macrophages, lymphocytes and mast cells, can express high levels of some cathepsins (such as cathepsin-K), therefore, the level of cathepsins may serve predicting the on-going inflammation for atherosclerosis (Wu *et al.*, 2018).

The selectins are a family of cell adhesion molecules found on the surface of activated endothelial cells and platelets, they also mediate the proliferation of leukocytes in the inflammatory process. P- and E-selectins in mice were reported to play an important role in both early and advanced stages of atherosclerosis development (Dong *et al.*, 1998).

Fibrinogen: fibrinogen may be used as a predictor of atherosclerosis. High concentrations of fibrinogen were reported in peripheral atherosclerosis patients compared to controls (Fowkes *et al.*, 1992). Leptin, in addition to its association to obesity, hyperleptinemia (in

high level) has also been suggested to play an important role in atherosclerosis (Beltowski, 2006).

White blood cells and uric acid: recently, white blood cells and elevated uric acid have shown to be associated to severe coronary artery disease (Kim *et al.*, 2017) and vulnerable carotid plaque in middle-aged adults (Li *et al.*, 2015).

To date, there is no strong evidence to prefer one biomarker to be the most predictive of cardiovascular events. Further studies on the pathogenesis of atherosclerosis may allow new biomarkers of atherosclerosis. Other obstacles for biomarkers are the non-specificity to atherosclerotic inflammation as well as the level of stabilization and lack of plaque localization.

1.3 Medical imaging

Atherosclerosis imaging encompasses a variety of imaging techniques already used to assess atherosclerosis (Figure 1.5). Together, these imaging modalities are indispensable to daily clinical practice and research to provide information of plaque compositions, measurement of molecular activity and disease status as well as the level of severity with or without the link of biological markers. However, vulnerable plaque identification is yet a major hindrance.
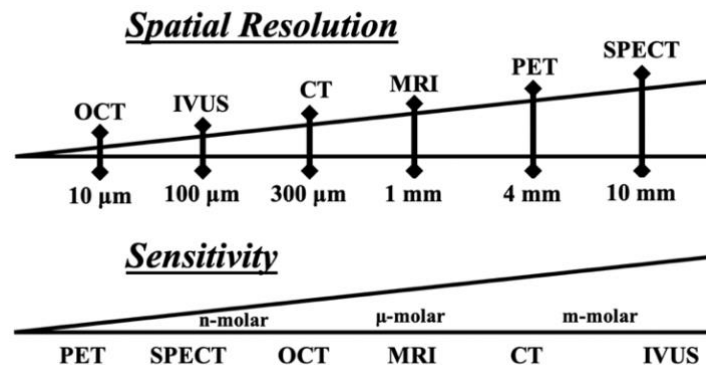
Figure 1.5 Illustration of spatial resolution and sensitivity of common imaging modalities utilized for vulnerable plaque identification (Sadeghi *et al.*, 2010).

Anatomical imaging helps delineating vascular anatomy and identify atherosclerosis stenosis severity. There are different imaging modalities providing plaque anatomical

features. Positron emission tomography (PET) and computed tomography (CT) imaging are the imaging modalities used in this thesis and they will be covered in next section.

Digital subtraction angiography (DSA) is traditionally considered as the gold standard of imaging of vascular disease (Mistretta and Crummy, 1986; Hill, Demchuk and Frayne, 2007), however, DSA lacks information beyond the luminal narrowing and with measurable risks that hinder its use to design a prospective study of healthy volunteers. Yet, there are other non-invasive vascular imaging techniques including magnetic resonance angiography (MRA), computed tomography angiography (CTA), and transcranial doppler (TCD) ultrasonography and their ease of use with low adverse events.

Other advantages of noninvasive imaging, especially TCD ultrasonography, is that it can be repeated in time, although these imaging modalities could not be accurate enough to replace DSA (Patel *et al.*, 2002). Additionally, atherosclerotic plaque would grow outward rather than inward for much of its life, so that substantial atherosclerosis can exist without producing stenosis in DSA (Glagov *et al.*, 1987). Nonetheless, several diagnostic and pathologic studies have shown that an acute event does not clearly associate with the degree of stenosis, insisting that inflammation but not stenosis could predict the plaque vulnerability. Subsequently, angiography alone may not be adequate for plaque vulnerability identification (Falk, Shah and Fuster, 1995; Pasterkamp *et al.*, 1998; Naghavi *et al.*, 2003; Kelly P and Bhatt DL, 2007).

Magnetic Resonance Imaging (MRI) is the most favorable non-invasive imaging to evaluate the thickness and integrity of the fibrous cap, intra-plaque hemorrhage, lipid-rich-necrotic-core (Briley-Saebo *et al.*, 2007; Anderson and Kramer, 2007). Non-invasive angiography can also be performed with MRI (Saba *et al.*, 2019). Additionally, MRI has shown to be comparable to CTA for stenosis, although the latter showed a favorable trend toward higher diagnostic performance (Hamdan *et al.*, 2011).

Moreover, MRI suffered low sensitivity compared to PET, as it requires the administration of contrast agents such as gadolinium, to alter the properties of hydrogen atoms and their local environment indirectly, so that changing their relaxation characteristics (Choudhury and Fisher, 2009). Plus, it has demonstrated that MRI is more challenging to identify spotty calcification compared with CT (Zhang *et al.*, 2019). Yet, artifacts resulting

from the air to tissue interface in the cavernous sinus area can negatively affect the evaluation of internal carotid arteries (Li *et al.*, 1996). Lastly, high-resolution MRI requires specialized receiver coils, unreasonably long imaging time and lack of generally accepted protocol for vascular imaging, making it less applicable compared with CT in clinical settings (Corti and Fuster, 2011; Mori *et al.*, 2016).

Recently, ultra-small superparamagnetic particles of iron oxide (USPIO) has been used as 'smart' contrast agents in patients with symptomatic carotid plaques and has shown to be correlated to macrophage-rich plaque area, where the MRI signal drops when USPIO are internalized by macrophages, thus identifying the cellular inflammation (Trivedi *et al.*, 2006; Howarth *et al.*, 2009; Morishige *et al.*, 2010; Richards *et al.*, 2011; Makowski *et al.*, 2013). But, USPIO were reported to accumulate 1.4-fold higher in anti-inflammatory M2 macrophages than in proinflammatory M1 macrophages, which favor ^{18}F-fluorodeoxyglucose (^{18}F-FDG) and PET over USPIO (Satomi *et al.*, 2013). Low contrast-to-noise ratio of USPIO might improve using larger microparticles of iron oxide (MPIO) compared to those for USPIO, although this agent has yet to be tested clinically for the evaluation of atherosclerosis inflammation (Lewis, Burrage and Ferreira, 2020). Addedly, CT is recognized to be superior in detecting and quantifying calcification than MRI (van den Bouwhuijsen *et al.*, 2015). It is noteworthy that 3T MRI with conventional neurovascular coils was reported to afford a high sensitivity, specificity, and accuracy in terms of identifying lipid rich necrotic core and IPH (Brinjikji *et al.*, 2018), and artificial intelligence algorithms for lumen and wall boundaries identification may enhance reproducibility and improve its general performances (van 't Klooster *et al.*, 2012; Saba *et al.*, 2014). Other imaging techniques reported in the literature being used for atherosclerosis are discussed in next paragraphs.

Intravascular ultrasound (IVUS): IVUS allows visualization of the arterial wall with high spatial resolution invasively (Priester and Litwin, 2009), and identifies plaque lipid core, remodeling and spotty pattern of calcification (Ehara *et al.*, 2004). It also revealed the size of the plaque (Ishino *et al.*, 2014). IVUS is usually only performed in the proximal vessels and in addition to its invasiveness, it is not suitable for imaging atherosclerotic plaques rich in foamy macrophages compared to ^{18}F-FDG-PET imaging and it does not

precisely measure the fibrous thin cap due to limited axial resolution and its intrinsic and extrinsic artifacts (Anderson and Kramer, 2007; Priester and Litwin, 2009; Garcia-Garcia, Costa and Serruys, 2010; Ishino *et al.*, 2014).

Optical coherence tomography (OCT): OCT was shown to be capable to provide both morphological and evaluation of the disease activity, where the co-localization of macrophages and microcalcifications in 116 subjects was demonstrated (Burgmaier *et al.*, 2018). However, due to a low penetration of OCT signal (2–4 mm), it is insufficient for detecting lipid core and calcification behind thick fibrous caps and led to inaccurate interpretation of plaque compositions and false positive due to microcalcification and foam cells accumulation (Manfrini *et al.*, 2006; Fujii *et al.*, 2015). The last error might be avoided using OCT in combination with IVUS (Fujii *et al.*, 2015). Finally, there is a limited patient compliance due to the invasive nature and a lack of longitudinal follow-up studies to evaluate the clinical impact of OCT.

Near infrared spectroscopy (NIRS): NIRS could identify lipid-rich atherosclerotic plaque and leads to vulnerable plaque identification (Cassis and Lodder, 1993). The first-in-man study using NIRS was conducted in 2 symptomatic and 8 asymptomatic patients (Madder, Abbas and Safian, 2015) and revealed its feasibility in detecting lipid core of plaques and a reduction in lipid content. However, NIRS imaging is still incapable to identify the depth of the plaque lipid core and thinness of the fibrous cap, that is one of the vulnerable plaque features (Kuku *et al.*, 2020). Multi-modality NIRS-IVUS combined in one single catheter allows the comprehensive assessment of atherosclerotic plaques using wave and light-based technologies. Accuracy for the prediction of necrotic core and large lipid plaques when multi-modality NIRS-IVUS was used, were more accurate than either alone (Kang *et al.*, 2015).

Single photon emission computed tomography (SPECT): SPECT is an imaging modality that uses a gamma-emitting radioisotope attached to a specific ligand which binds to certain tissue of interest in the body. The radioisotopes typically used in SPECT are Technetium-99m (^{99m}TC is the most used), iodine-123, iodine-131, thallium-201, Gallium-67 and Indium-111 (Bouziotis *et al.*, 2013). The 99mTc-IDA-D-[c(RGDfK)]$_2$ tracer binds to vitronectin receptor and opens avenue for targeting activated endothelial cells. A

study using $\alpha_v\beta_3$ integrin-targeted probe ^{99m}Tc-IDA-D-[c(RGDfK)] with SPECT/CT (Yoo *et al.*, 2015) demonstrated a significant targeted tracer uptake in murine atherosclerotic aortas.

The most important adhesion molecules in atherosclerosis is the vascular cell adhesion molecule 1 (VCAM1) that assists in adhesion and recruitment of inflammatory cells to vulnerable plaque. VCAM1 scFv/cAb (conjugated to ^{99m}Tc) showed its feasibility and effectiveness for early diagnosis and evaluation of atherosclerosis in animal model (Broisat *et al.*, 2014; Liu *et al.*, 2016). Interleukin-2 (IL-2) receptors over-expressed on activated T lymphocytes has been targeted using ^{99m}Tc-HYNIC-IL-2 in ex vivo study that confirmed its specificity for imaging activated T lymphocytes in carotid plaques (Glaudemans *et al.*, 2014). Folate receptor-β (FR-β) is expressed on activated macrophages and especially in M2 polarized macrophages, therefore, ^{99m}Tc-folate has been studied in carotid endarterectomy specimens of 20 patients and positive correlation was found between high ^{99m}Tc-folate accumulation and FR-β expression on M2 polarized macrophages (Jager *et al.*, 2014).

There is a strong correlation between the risk of plaque rupture and quantity of macrophage (Schaar *et al.*, 2003). Annexin V radiolabeled with ^{99m}Tc was found to closely correlates with intensity of macrophages and the degree of apoptosis (Cheng *et al.*, 2015), by binding to exposed phosphatidylserine on cell surface of apoptotic macrophages and they are the majority of apoptotic cells at the site of rupture for atherosclerotic plaque (Littlewood and Bennett, 2003). [99m]Tc -Annexin on a study of 5 rabbits was used for non-invasive detection of apoptotic macrophages (Kolodgie *et al.*, 2003) and showed higher uptake (9-fold) in atherosclerotic plaque compared to non-lesion and reported to specifically target the vulnerable plaques in animal model (Li *et al.*, 2016). Annexin V has been shown to be a safe radiopharmaceutical with excellent clearing speed in the blood stream (24 ± 3 min) and offers a favorable biodistribution for imaging apoptosis in the abdominal as well as thoracic area (Kemerink *et al.*, 2003). Its preferential uptake compared to ^{18}F-FDG of the advanced stage has been demonstrated in animal model (Zhao *et al.*, 2007). However, long biological half-life and high liver and kidneys uptake make its limitations (De Saint-Hubert *et al.*, 2009). Others (Vemulapalli *et al.*, 2007) have demonstrated the feasibility of indium 111 ^{111}In-oxine–labeled bone marrow (BM) with high-resolution whole-body SPECT for monitoring and quantifying atherosclerosis in a murine model. Somatostatin Subtype Receptor 2 (SST2)

is upregulated significantly during the differentiation of monocytes into macrophages (Dalm *et al.*, 2003). ^{111}In-DOTA JR11 in mice study (Meester *et al.*, 2020) demonstrated high uptake of this tracer at plaque location.

2. COMPUTED TOMOGRAPHY AND POSITRON-EMISSION TOMOGRAPHY

2.1 Computed tomography (CT)

2.1.1 Assessment of atherosclerosis

Computed tomography (CT) refers to computerized x-ray procedure in which a narrow beam of x-ray radiation rotated around the patient's body and acquired in a breath-hold that typically lasts a few seconds. CT measures x-ray attenuation coefficient (μ) by the detectors transmitted to a computer and expressed according to a density scale called Hounsfield unit (HU). In the HU scale, water is assigned a value of 0 HU and other CT values are computed accordingly as:

$$HU = \frac{\mu_{Tissue} - \mu_{Water}}{\mu_{Water}} \times 1000$$

The attenuation characterizing tissue density allows non-invasive assessment and visualization of stenosis and calcification of atherosclerotic plaque (Saba *et al.*, 2019). Furthermore, visualizing the vessel lumen is achieved using an injection of an iodinated contrast agent. Additionally, the potential of CT in atherosclerosis is considered as an independent predictor of cardiovascular events (Bamberg et al., 2011).

2.1.2 Quantification of calcification

Quantification of calcification using CT images is a robust predictor of cardiovascular events (Bamberg *et al.*, 2011; Dweck *et al.*, 2016) and considered as a biomarker of overall disease and independent of conventional risk scores, like FRS (Malguria, Zimmerman and Fishman, 2018). In this context, there are a variety of approaches for calcification scores which summarized in the following paragraphs.

2.1.2.1 Agatston score (AS)

Agatston score (AS, mm^2) is a common approach introduced in 1990 by Arthur Agatston and colleagues (Agatston *et al.*, 1990) and has still remained a standard method. AS is calculated by selecting pixels above a threshold of 130 HU and excluding structures smaller

than 1 mm^2. The area of calcification is multiplied by a weighting factor according to maximum HU (HU_{max}) number in the plaque area. Weighting factor of 1 for a range of 130–199 HU_{max}, 2 for 200–299 HU_{max}, 3 for 300–399 HU_{max}, and 4 for $\geq$ 400 HU_{max}. The total AS for each individual is calculated by summing up the scores in all slices, where: $AS_{Total} = \sum_i AS_i$.

2.1.2.2 Volume score (VS)

Volume score (VS, mm^3) was first established by (Callister *et al.*, 1998). VS is calculated by segmenting calcified plaque area (>130 HU) and multiplied by the number of slices of those plaques. The total VS therefore is calculated by summing up VSs, where: $VS_{total} = \sum_i VS_i$.

2.1.2.3 Mass score (MS)

In 2002, a method to measure the absolute real mass of calcification was introduced (Hong *et al.*, 2002). The mass score (MS, mg), also called mean CT calcification mass score. It is calculated by multiplying the calcified plaque volume (pixel volume >130 HU), mean HU of calcified plaque and calibration factor (CF). The latter is determined using external standard calibration phantom having a calcified object with a known density of calcium (ρ_{HA}) (usually hydroxy apatite "HA") and measuring its mean intensity, where: $CF = \frac{\rho_{HA}}{HU_{HA} - HU_{Water}}$. By determining the mean CT number (CT_{HA}) of hydroxy apatite and correcting it for the mean CT number of water (HU_{water}). The total MS, therefore, is calculated summing up MSs, where $MS_{total} = \sum MS_i$.

2.1.2.4 Calcium coverage score (CCS)

Brown and his colleagues (Brown *et al.*, 2008) introduced different score called calcium coverage score (CCS, unitless). It is calculated by dividing the number of artery segments in which the calcified plaque was present (>130 HU) by the total number of absolute artery segments in the coronary arteries and then multiplying this quotient by 100 to estimate the percentage of coronary arteries affected by the calcified plaque.

2.1.2.5 Derlin score (DS)

Derlin score (DS, unitless) is calculated by determining the percentage ratio of arterial wall circumference to calcification circumference (>130 HU) and scaling that percentage

into a scoring scale for circumferential extent (Derlin, Wisotzki, *et al.*, 2011), where 0, no calcification; 1, less than 25% of arterial wall circumference; 2, 25%–50% of arterial wall circumference; 3, 50%–75% of arterial wall circumference; and 4, greater than 75% of arterial wall circumference.

2.1.2.6 Agatston coverage "calcification" score (ACS)

We have recently produced another way of quantifying calcification score in the combination of AS and CCS (Al-enezi *et al.*, 2019), where the area of calcification (>130HU) is divided by total arterial area and multiplied by both weighting factor as in AS and by 100 to estimate the percentage as in CCS. In this manner, we take into account both the amount (as in AS) and distribution of calcification build-up (as in CCS).

2.2 Positron-emission tomography (PET)

PET uses positron emission radionuclides produced in a cyclotron such as fluorine-18, carbon-11 and oxygen-15 that labels a variety of compounds either identical or analogous to naturally occurring substances in the body (radiotracers). PET measurement is preceded by an injection of a radiotracer and detecting gamma photon pairs. The collected data are processed to reconstruct a 3D or 4D images. PET is the most sensitive non-invasive imaging modality clinically available, that is proficient in detecting picomolar tracer concentrations. It enables the quantification of small metabolic changes within the plaques (Evans et al., 2016), and it is more quantitatively accurate due to its sensitivity and photon scatter and attenuation corrections (Okuda et al., 2021). It is usually combined with CT or MRI to compensate for its low spatial resolution and anatomical localization. In the next sections, the methods of quantification of PET measurements are presented followed with a discussion on PET radiotracers.

2.2.1 Partial volume effect

PET has some technical impediments which include partial volume effect (PVE). PVE causes a drop-in apparent activity and appears in the image less than what it really should be. There are two major sources of PVE in PET images:

1. The limited spatial resolution of the scanner.

   When an object is small (< 2 times the full width of half maximum "FWHM" of the intrinsic spatial resolution of PET scanner[1]), Figure. 2.1a (Hoffman, Huang and Phelps, 1979), or partially occupies in the field of view (FOV) as a function of space or time (Figure. 2.1b (Erlandsson *et al.*, 2012)), therefore, due to averaging several comprising picture elements within the FOV, this would lead to an underestimate of the detected tracer concentration.
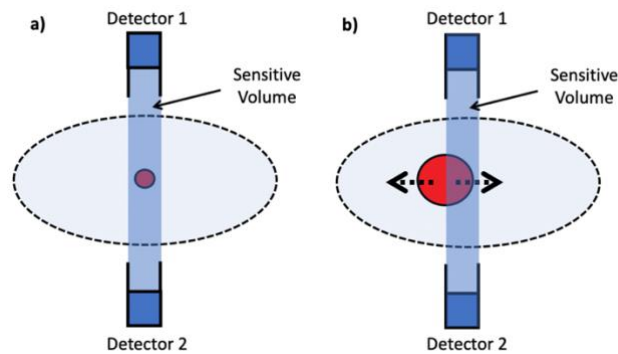
Figure 2.1 PVE due to small object (small circle) in the FOV (a), or partially occupied in the FOV in space or time, the black arrows represent a possible motion of the object during the acquisition (b).

2. The image sampling.

   The activity distribution of a tracer used is sampled on a voxel grid (Figure 2.2 (Soret, Bacharach and Buvat, 2007)). The ideal contour of the activity distribution of an object would not match the contour of voxels but further comprise activity of surrounding object.
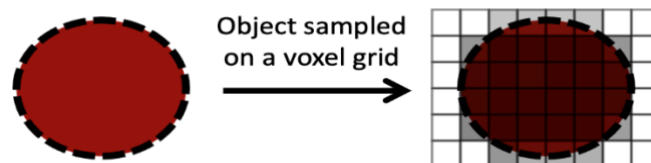
Figure 2.2 Illustration of PVE due to image sampling on a voxel grid (each square represents picture element).

---

[1] FWHM is used to measure the intrinsic spatial resolution quantitatively. This measurement is done by imaging a single point source placed at the center of the scanner field of view, the intensity line profile of this point source would give a bell-shaped curve known as the point-spread function of the scanner. FWHM (in a unit of length) would be measured as the width at 50% of maximum amplitude.

Different approaches have been proposed in overcoming such an issue (Erlandsson *et al.*, 2012). Recovery coefficient (RC) due to its simplicity and practicality (Srinivas *et al.*, 2009) has been broadly applied and provided more accurate measurement of Standard uptake value (SUV) (Croteau *et al.*, 2010).

The RC curve is obtained by using a phantom having cylinders with different diameters which were filled with the same activity (Figure 2.3a) and placed in the center of the FOV of the PET scanner, where RC= $\frac{\text{Measured cylinder activity}}{\text{True activity}}$, thus, RC curve is obtained as a function of the cylinder diameter (Figure 2.3b (Croteau *et al.*, 2010)).
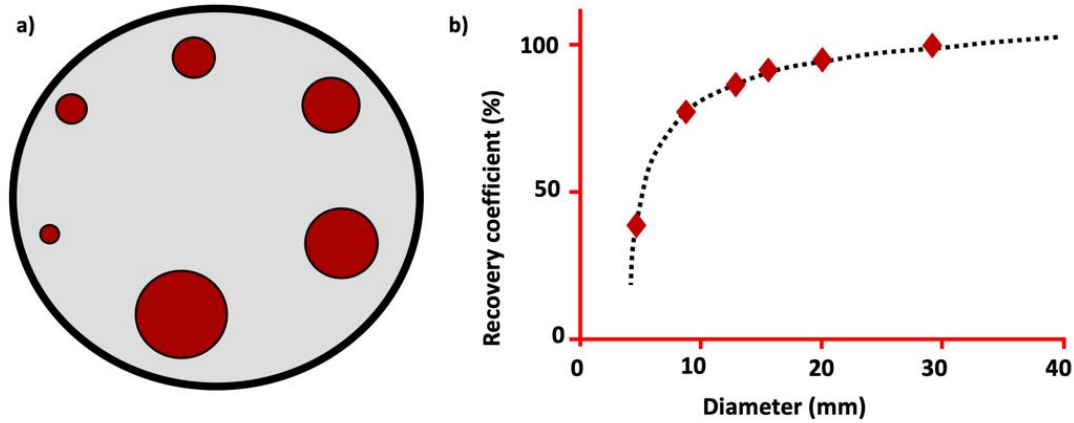
Figure 2.3 Illustration of PVE phantom of 6 cylinders of different sizes (a), RC curve obtained from PVE phantom (dotted line represents the interpolation within the diameters).

2.2.2 Quantification of PET measurement

2.2.2.1 Standard uptake value (SUV)

SUV is mathematically expressed as the ratio of decay-corrected tracer activity concentration in a region of interest (ROI) and injected activity per kilogram of the patient's weight or lean body mass or body surface area (Kotasidis, Tsoumpas and Rahmim, 2014).

$$\text{SUV} = \frac{\text{Activity concentration in ROI } (\frac{\text{Bq}}{\text{kg}})}{\text{Injected activity (Bq)}} \times \text{Body weight (kg)}$$

2.2.2.2 Tissue to background ratio (TBR)

TBR is another way to quantify PET signal and devised to correct for both background activity and false high uptake effects (Rudd *et al.*, 2009). TBR is a ratio of SUV of a ROI to SUV in the lumen of large vein.

$$TBR = \frac{SUV\ (ROI)}{SUV\ (Blood\ pool)}$$

TBR has been reported to be very sensitive to the difference between time of injection to the time of measurement (Evans *et al.*, 2016). SUV may also be evaluated as SUVmax[2] (Derlin, Habermann, *et al.*, 2011) and was shown to be comparable to TBR. But, SUVmax is highly affected by the noise and pixel size (Ronald Boellaard *et al.*, 2004). Other ways such as $SUV_{0.75max}$ may be used instead to eliminate possibility of single pixel measurement (noise) (Lee *et al.*, 2000).

2.2.2.3 Fractional uptake rate (FUR)

FUR represents the uptake value normalized by the arterial input of tracer activity (Ishizu *et al.*, 1994).

$$FUR = \frac{Activity\ concentration\ in\ ROI\ (T)}{\int_0^T Blood\ time\ activity\ curve\ (t)dt}$$

where T is the time at the mid-frame.

FUR is better and non-affected by patient's weight and gender compared to SUV and TBR, however it requires blood sampling (Rutland, Que and Hassan, 2000).

2.2.2.4 Graphical analysis

Graphical analysis (Patlak plot) is a more comprehensive way of PET quantification (Freedman *et al.*, 2003). Patlak plot transforms the multiple time measurements of the activity in plasma and ROI into a linear plot and the slope of it reflects the number of tracer irreversible binding sites at that ROI (Gjedde, 1982).

$$\frac{A_{ROI}(T)}{A_{Blood}(T)} = Slope \times \frac{\int_0^T A_{Blood}(t)dt}{A_{Blood}(T)} + Intercept,\ T\ is\ the\ middle\ frame\ time.$$

---

[2] SUVmax is defined as a hottest pixel/voxel in a ROI normalized to injected activity and body weight.

In case of reversible binding, Logan plot is used instead (Logan *et al.*, 1990).

$$\frac{\int_0^T A_{ROI}(t)dt}{A_{Blood}(T)} = \text{Distribution Volume} \times \frac{\int_0^T A_{Blood}(t)}{A_{Blood}(T)} + \text{Intercept, T is the middle frame time.}$$

2.2.2.5 Pharmacokinetic modeling

Pharmacokinetic modeling and particularly 2-tissue-compartment model of ^{18}F-FDG (Figure 2.4) is a set of differential equations representing the radiotracer compartments (Phelps *et al.*, 1979):

$$C_{PET}(t) = \frac{K_1}{\alpha_2 - \alpha_1}\left[(k_3 + k_4 - \alpha_1)e^{-\alpha_1 t} + (\alpha_2 - k_3 - k_4)e^{-\alpha_2 t}\right] \otimes IF + k_5 IF$$

$$\alpha_1 = \frac{k_2 + k_3 + k_4 - \sqrt{(k_2 + k_3 + k_4)^2 - 4k_2 k_4}}{2}$$

$$\alpha_2 = \frac{k_2 + k_3 + k_4 + \sqrt{(k_2 + k_3 + k_4)^2 - 4k_2 k_4}}{2}$$

where K_1, k_2, k_3 and k_4 are rate constants.
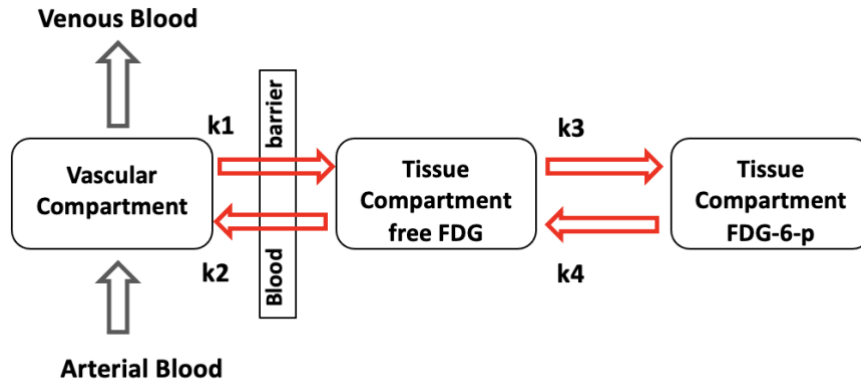
Figure 2.4 Illustration of 2-tissue compartmental model of ^{18}F-FDG.

Such a model is a standard in describing the kinetics of the tracer. However, in the case for atherosclerosis where the blood is a major component, it is a challenging. We have recently demonstrated the feasibility of 2-tissue compartmental modeling in atherosclerosis when the blood image is extracted by factor analysis from the measured images from which

the tissue blood fraction is derived. This approach was tagged without blood sampling method (WOBS) (Al-enezi and Bentourkia, 2020).

$$C_{PET}(t) = \frac{K_1}{\alpha_2 - \alpha_1} \left[\left(k_3 + k_4 - \alpha_1 \right) e^{-\alpha_1 t} + (\alpha_2 - k_3 - k_4) \, e^{-\alpha_2 t} \right] \otimes \nu TBV + TBV,$$

TBV is tissue blood volume, and the constant $\nu > 1$.

2.2.3   PET tracers for atherosclerosis imaging

Radioisotopes used in PET imaging modality are positron emitting radioisotopes, these radioisotopes are labeled with different substances in its chemical composition for targeting specific cells or physiological processes (such as glycolysis). Some radiotracers particularly of interest to atherosclerosis are reported in the next paragraphs.

^{18}F-FDG: in regards of atherosclerosis tracers, ^{18}F-FDG is the most used and studied radiotracer (Shepherd and Kahn, 1999)). ^{18}F-FDG uptake has shown to be strongly correlated with macrophages density in atherosclerotic plaques (Rudd *et al.*, 2002; Tawakol *et al.*, 2006).

[18]F-macroflor: it is a poly-glucose nanoparticle allowing rapid renal excretion (small size), fast clearance from blood pool and was found having high affinity for cardiovascular macrophages with minimal myocyte uptake. It has been studied in mice, rabbits, and a non-human primate (Raffort *et al.*, 2017) and may become a promising tracer for imaging cardiac inflammation.

DOTATATE: DOTATATE ([1,4,7, 10-tetraazacyclododecane-N,N′,N″,N‴-tetraacetic acid]-d- Phe1,Tyr3-octrotate) labeled with [64]Cu (Malmberg *et al.*, 2015) and [68]Ga (Rominger *et al.*, 2010) is another promising tracer that was found to be correlated with calcification burden and cardiovascular risk factors, such as age and hypertension. It was also found to be comparable with ^{18}F-FDG (Li *et al.*, 2012). In addition, ^{68}Ga-DOTATATE was found capable to visualizes the distribution of somatostatin receptor subtype-2 (SSTR-2) (Rominger *et al.*, 2010). [64]Cu compared to ^{68}Ga might be favorable due to shorter maximum positron range but longer half-life. The correlation between ^{68}Ga-DOTATATE and ^{18}F-FDG was also demonstrated for 41 atherosclerotic patients (Tarkin *et al.*, 2017).

^{18}F-fluorodeoxymannose (^{18}F-FDM): it is a tracer targeting mannose receptor (isomer of glucose) that are upregulated particularly in M2 polarized macrophages in high-risk plaque (Dweck *et al.*, 2016) and associated to neovascularization and intraplaque hemorrhage in atherosclerotic plaque.

Choline: it is taken up by activated macrophages and considered a good target for macrophage infiltration, where ^{18}F-fluorocholine (^{18}F-FCH) and ^{18}F-methylcholine (^{18}F-FMCH) are radiolabeled-choline PET radiotracers utilized clinically for diagnosing and for high-risk-prostate cancer staging and might serve as a marker toward identifying inflammatory plaques. In pre-clinical model, a comparison study for murine atherosclerotic lesions between ^{18}F-FCH and ^{18}F-FDG has demonstrated a better correlation of ^{18}F-FCH with macrophage staining than ^{18}F-FDG (Matter *et al.*, 2006). In a study of 10 stroke patients utilizing ^{18}F-Fluorocholine(^{18}F-FCH) (Vöö *et al.*, 2016) has reported a strong correlation of ^{18}F-FCH uptake to macrophage infiltration and recent symptoms.

Fluorine-18-NaF (18F-NaF): the microcalcifications are thought to identify vulnerable atherosclerotic plaques while the disease is still silent through the clear association to macrophage inflammatory activity in the early-stage of atherosclerosis (Aikawa *et al.*, 2007). ^{18}F-NaF has recently been reported to noninvasively visualize the high-risk of microcalcifications in unstable plaques (Derlin *et al.*, 2010; Joshi *et al.*, 2014). It has also been demonstrated to predict an increase in macrocalcification within 18 months follow-up (Høilund-Carlsen *et al.*, 2019), and reported to identify calcification changes in the aortic valve with age (Rojulpote *et al.*, 2020). Another approach of ^{18}F-NaF in combination with CTA (Moss *et al.*, 2019) shows high precision and reproducibility in coronary atherosclerotic plaque and may serve as a biomarker of plaque vulnerability.

Hypoxia radiotracers: hypoxia (low oxygen tension) likely results from an increase in plaque size leading to a reduction of oxygen level within the plaque which induces local hypoxia that is an important stimulus of both pathological and physiological processes associated with rupture-prone-plaque, including angiogenesis and apoptosis (Evans *et al.*, 2016). ^{18}F-HX4 is a promising tracer for hypoxia with good target to background ratio compared to other hypoxic tracers (Sanduleanu *et al.*, 2020) with good correlation of its uptake and plaque size (Van Der Valk *et al.*, 2015).

3. RESEARCH PROBLEM AND HYPOTHESES

The chronic inflammation is one of the main mechanisms associated in atherosclerosis initiation and progression.

The objective of this thesis is to assess the inflammation and micro-calcification of atherosclerotic plaque quantitatively using ^{18}F-FDG and ^{18}F-NaF radiopharmaceuticals in dynamic mode of PET imaging, and to assess the metabolic activity represented by FUR, MRG, TBR and ^{18}F-NaF uptake represented by TBR in the correlation with different calcification phenotypes. Other attempts were to identify non-calcified plaque in CT images and to correlate it with ^{18}F-FDG.

Objective 1: Spotty of calcification and inflammation

The calcification is one of the common plaque features which is evidenced by CT imaging. Different shapes, area and locations may act as a marker of a stable plaque whereas other forms might identify an unstable vascular environment (Shi *et al.*, 2020). Spotty calcification is a remarkable feature of vulnerable plaque associated with 2-fold increase in plaque rupture and related to acute myocardial infarction and unstable angina pectoris (Ehara *et al.*, 2004; Fujii *et al.*, 2005; Van Velzen *et al.*, 2011; Mizukoshi *et al.*, 2013; Maurovich-Horvat *et al.*, 2014; Nerlekar *et al.*, 2018). The presence of spotty calcification was significantly associated with thinner fibrous caps and larger lipid necrotic cores of atherosclerotic plaque (Kataoka *et al.*, 2014). Number of spotty calcifications were shown to be significantly higher in the rupture group than in the non-rupture group (Sakaguchi *et al.*, 2016). We evaluated the effect of spotty calcified plaque on the metabolic activity of glucose using ^{18}F-FDG tracer.

Objective 2: Modified kinetic modeling in atherosclerosis

The two-tissue compartmental model is a standard in describing the kinetics of the tracer (Phelps *et al.*, 1979). However, in the case for atherosclerosis where the blood is a major component in the arteries, the model becomes uncertain. We examined the feasibility of using two-tissue compartmental model with blood input function obtained from factor analysis with a modified model without blood sampling approach and independent of partial volume effect.

Objective 3: Non-calcified plaque in CT image

Non-calcified plaque (NCP) is a lipid rich plaque and was shown to be associated with high disease activity and risk of plaque rupture (Uetani *et al.*, 2010; Skeoch and Bruce, 2015). CT imaging was focused on the calcification quantification of atherosclerotic plaque. Recently, CT has shown to be able to identify NCP (Noguchi *et al.*, 2018). The plaques with attenuation ≤30 HU was identified with a sensitivity of 95% and specificity of 85% in the correlation with IVUS (Marwan *et al.*, 2011), and the same cut-off value was associated with greater risk of plaque rupture or acute syndromes (Motoyama *et al.*, 2007). Other cut-off value of ≤ 50 HU of napkin-ring plaques has been reported in a high specificity and high positive predictive value for the presence of high-risk lesions (Maurovich-Horvat *et al.*, 2012). In this context, we analyzed a cut-off value of ≤ 50 HU from CT images in the correlation with metabolic activity of ^{18}F-FDG. We have reported the positive correlation of ≤ 50 HU to metabolic activity and possibility of CT images to identify non-calcified plaque.

Objective 4: ^{18}F-NaF PET/CT for atherosclerosis

^{18}F-NaF has been demonstrated to predict an increase in macrocalcification within 18 months (Høilund-Carlsen *et al.*, 2019) and with age (Rojulpote *et al.*, 2020). ^{18}F-NaF uptake was also shown to be associated with increased risk (Blomberg *et al.*, 2017) and reported a marker of plaque (Moss *et al.*, 2019). It is also a predictor of early stages of plaque formation (Fiz *et al.*, 2015). Recently, ^{18}F-NaF uptake was shown to be correlated to spotty calcifications (Kitagawa *et al.*, 2017). Yet, ^{18}F-NaF in arteriosclerosis needs firm conclusions and more studies (Høilund-Carlsen *et al.*, 2020). In this section, we report ^{18}F-NaF uptake in volunteers and correlate its uptake with calcification parameters and spotty calcified plaques. Additionally, we correlated arterial wall attenuation with ≤ 50 HU (non-calcified plaque, NCP) with ^{18}F-NaF uptake. We found a reverse correlation of ^{18}F-NaF uptake to calcification area and significant increase of ^{18}F-NaF uptake was associated with spotty calcifications and NCP.

4. MATERIALS AND METHODS

4.1 Experimental measurements

4.1.1 ^{18}F-FDG

4.1.1.1 Population

We recruited 10 subjects with age ranging from 65 to 85 years (69.15 ± 3.7). These subjects were imaged twice at 12 months apart for a total of 19 PET/CT scans (one subject was measured only once). Four recruited subjects were under medication after first scan for 1 year (Rosuvastatin 20 mg/day). Five subjects were having chest angina and they were taking their own prescribed anti-inflammatory drugs. In total, at the PET/CT scans, 10 subjects were non-medicated and 9 were under medication. All the subjects were non-smokers and not having excessive alcohol consumption, not taking antioxidants, vitamin supplements or hormonal replacement for women.

4.1.1.2 Vital signs measurements

The measurement of glucose, total cholesterol, low density lipoprotein, high density lipoprotein, triglyceride and CRP were performed in each subject after overnight fasting.

4.1.1.3 Imaging

Subjects were injected intravenously with an ^{18}F-FDG bolus at an activity of 140 to 400 MBq depending on the subject's weight. PET and CT were performed with a PET/CT system (Philips Gemini TF 16). Imaging started with non-enhanced low-dose CT with tube potential of 120 kV. CT images were reconstructed in sets of transaxial 512×512 matrices with a pixel size of 1 mm × 1 mm × 5 mm. The PET scans were initiated in dynamic mode for 30 min and were divided into 26 consecutive time frames of 12×10 secs; 8×30 secs; 6×240 secs. PET slices were reconstructed into a 144×144 matrix, and the voxel size was 4 mm × 4 mm × 4 mm. The arteries scanned were the aorta and left and right iliacs in one bed position. CT and PET was established based on their location in mm as read from CT and PET image file headers. PET and CT images were reconstructed using three-dimensional row action maximum likelihood algorithm (3D-RAMLA).

4.1.2 ^{18}F-NaF

4.1.2.1 Population

Five volunteers (non-oncologic patients) were recruited for ^{18}F-NaF study.

4.1.2.2 Imaging

^{18}F-NaF PET/CT was performed on Gemini TF 16-slice PET/CT scanner (Philips). A non–contrast-enhanced CT scan was acquired first in a 512×512 data matrix and pixel size of $1 \times 1 \times 4$ mm^3 in headfirst spine position with tube potential of 120 kVp.

After CT examination, PET data were acquired in a dynamic mode for 40 min (12×10 secs, 8×30 secs, 8×180 secs and 2×300 secs) immediately after intravenous injection activity of 251.25 ± 33.26 MBq of ^{18}F-NaF (normalized to body's weight) with a 144×144 data matrix and in-plane spatial resolution of 4 mm covering the same field of view as in CT.

Furthermore, contrast enhanced CT images were acquired afterward, in a 512×512 data matrix after injection of iodinated contrast agent (370 mg/ml with a bolus volume of 100 ml at a flow rate of 3 ml/sec) with a pixel size of $0.8 \times 0.8 \times 0.5$ mm^3, with a tube potential of 120 kVp.

All images were reconstructed using three-dimensional row action maximum likelihood algorithm (3D-RAMLA).

4.2 Ethics

All protocols were approved by the research ethics committee of the Faculty of Medicine and Health Sciences, University of Sherbrooke, Canada, and the subjects gave their written consent.

4.3 Analysis

PET segmentation of arteries was carried out on the first 6 image frames with active contour[3] per artery image slice. Active contour was also used semi-automatically for CT segmentation. We also used CT atlas images for verification of identified ROI (Figure 4.1).

The calcification was visually identified on thresholded CT images (>130 HU). Active contour was then applied to identify calcification region (Figure 4.2 and Figure 4.3). Calcification region was measured as a ratio of calcification region to whole artery region per slice.

PET images were further decomposed into blood and tissue components using factor analysis. Blood time activity curve (TAC) (Figure 4.4 and Figure 4.5) was extracted from blood images in axial view from aorta for SUV, TBR, FUR calculation and 2-tissue compartmental fitting.

For ^{18}F-NaF images, we segmented the contrasted enhanced CT images in the same manner as previously mentioned. The ROI was co-registered on the corresponding non-enhanced CT slice (Figure 4.6).

---
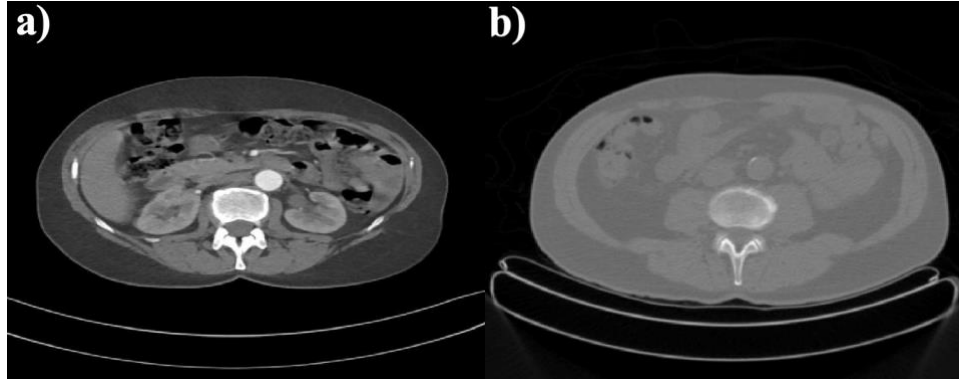
[3] The active contour is an iterative region-growing image segmentation algorithm used for detecting edges of image objects. It places an initial contour on an image and evolving the contour towards the objects boundaries on the image by minimizing the main function of this algorithm that consists of 3 functions, first function represents a set of points making up the contour, the second function represents the image gradients and last function is the integral of these functions.
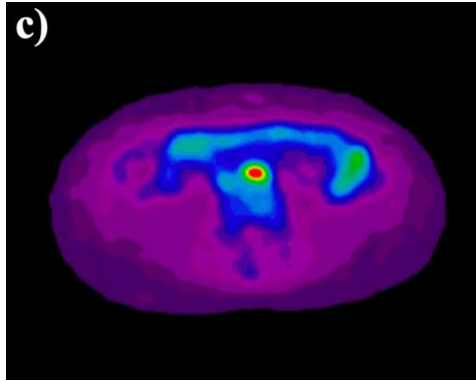
Figure 4.1 a) Transaxial image of CT Atlas. b) CT image of abdominal aorta. c) the corresponding PET image.
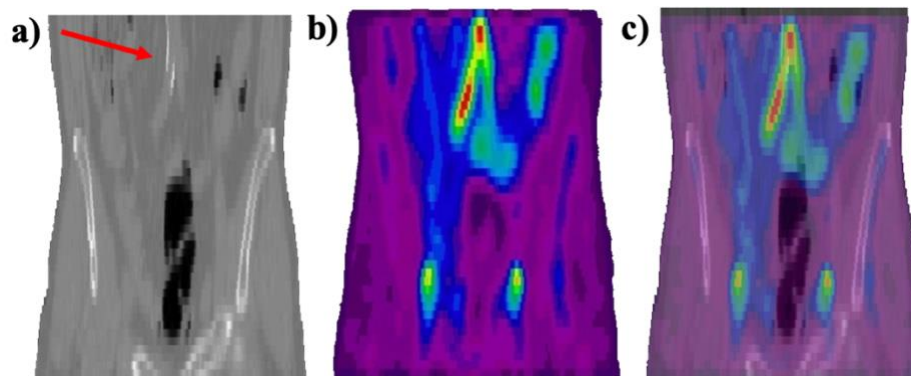
Figure 4.2 PET/CT coronal images of the abdomen, a) CT with calcification (arrow), b) PET image and c) fused PET-CT.
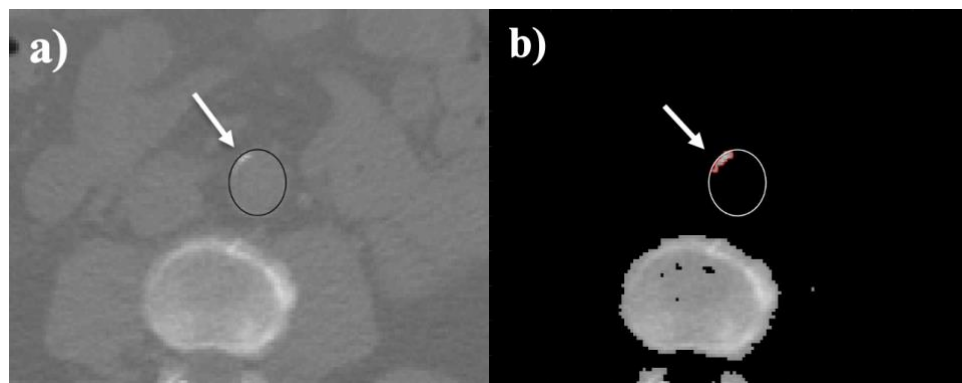
Figure 4.3 Transaxial images of CT showing ROI on aorta(a) and on calcification (b).
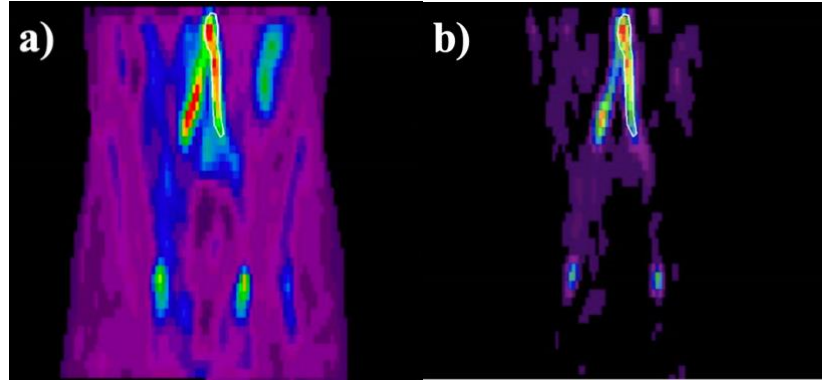
Figure 4.4 Coronal PET images, a) measured image with blood ROI, and b) decomposed blood image with factor analysis with ROI on aorta.
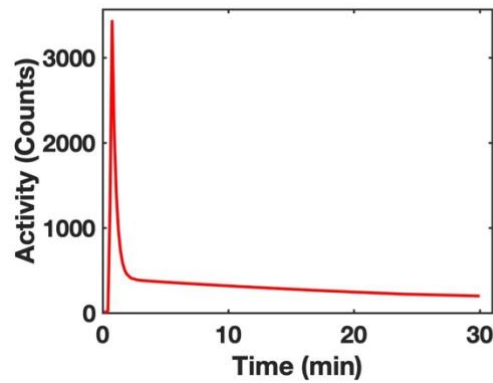
Figure 4.5 TAC of aorta from blood image obtained with factor analysis.
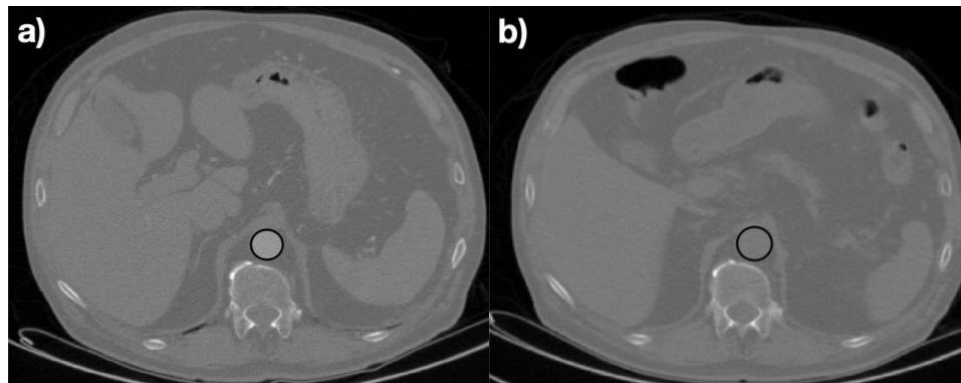
Figure 4.6 Transaxial image of contrast enhanced CT (a), and CT image of abdominal aorta (b).

TBR was calculated from the last 3 data points of the TAC for ^{18}F-FDG images. For ^{18}F-NaF, the last 3 data points of the TAC were normalized to the blood pool from superior vena cava. All data were partial volume corrected using recovery coefficients from the phantom.

SUV was calculated as the mean of activity within 75% from the maximum for last 3 data points of TAC multiplied by SUV scale (suvscl) per patient.

4.4 Statistics

For clustering the data, we used Ward's clustering method and Automatic Hierarchical K-means algorithm (AHK) and we enhanced its performance with the use of silhouette-coefficient, the later was automatic and non-supervised.

The statistical analyses were performed in MATLAB. The continuous data were tested for normality using the D'Agostino-Pearson omnibus test. Normally distributed data were analysed with the aid of analysis of variance ANOVA for unpaired multi-groups and with the student t-test for the comparison of unpaired two groups and expressed as mean ± STD.

Non-parametric data were compared using Wilcoxon-Mann-Whitney U test and expressed as median with interquartile range (IQR). The goodness of fit between the measured TACs and the model fits was assessed by Pearson's correlation coefficient squared (r^2) in each ROI.

For the receiver operating characteristic curve (ROC) analysis, sensitivity and specificity were calculated for different cut-off points and optimal cut-off value was computed as an intersection point between sensitivity and specificity values and according to CLSI/NCCLS guidelines.

Statistical significance was assumed for p-values < 0.05.

5. ARTICLE 1

Assessment of calcification in atherosclerosis with Dynamic ^{18}F-FDG-PET/CT imaging in elderly subjects

Mamdouh S. Al-enezi, Redha-alla Abdo, Mohamed Yazid Mokeddem, Faiçal A. A. Slimani, Abdelouahed Khalil, Tamas Fulop, Eric Turcotte, M'hamed Bentourkia

Contribution of the student: Mamdouh S. Al-Enezi performed the analyses for this manuscript and the preparation of the first draft.

Résumé:

Il a été démontré que le métabolisme du glucose dans les artères avec athérosclérose est un indicateur de l'inflammation qui pourrait être un précurseur de la rupture de la plaque. Dans cette étude prospective, nous avons évalué la corrélation entre la calcification artérielle et le métabolisme du glucose en utilisant l'imagerie TDM/^{18}F-FDG-TEP chez des personnes âgées. Dix sujets âgés de 65 à 85 ans ont été imagés par le TDM/^{18}F-FDG-TEP dynamique deux fois pour un total de 19 mesures, un sujet n'a été scanné qu'une seule fois. La calcification artérielle a été déterminée avec un seuil de 130 unités Hounsfield (HU). L'intensité de la calcification et le rapport de la zone de calcification à la surface totale de l'artère ont été classés en quatre classes séquentielles à partir des images de la TDM. Les images de l'artère ont également été classées. Leur métabolisme du glucose respectif a été évalué avec un taux de captation fractionnelle (FUR). L'analyse factorielle a été utilisée dans cette étude pour séparer les images de l'activité dans le sang de celle dans les tissus afin d'extraire les courbes temps-activité de l'activité dans le sang pour les calculs du FUR. Les images TEP des artères ont été corrigées pour l'effet de volume partiel. Le nombre total des segments artériels analysés s'élève à 1332, parmi eux il y a 1085 sans calcification (81%) et 247 (19%) avec calcification. Il est à noter que 94 segments présentaient des calcifications multiples. Il y a eu une différence statistiquement significative dans les valeurs du FUR entre les segments non calcifiés et les segments calcifiés et aussi entre les sujets sous médicament et les sujets ne prenant pas de médication lorsque nous avons comparu les sujets basés sur

l'aire de calcification. Aucune différence statistiquement significative du FUR n'a été trouvée parmi les groupes ayant une seule aire de calcification en fonction de l'intensité, alors que dans les groupes avec des aires de calcifications multiples, il y avait une différence statistiquement significative pour tous les segments d'artère. L'activité métabolique varie pour les segments non calcifiés à calcifiés ($p < 0.05$). Il a été démontré que les calcifications dans les groupes de calcifications multiples ont des effets différents de ceux dans les groupes avec une seule aire de calcificationen fonction de l'activité métabolique représentée par le FUR ($p < 0.05$).

Mots Clés : L'athérosclérose ; Calcification ; Artères; Plaque; TEP ; TEP/TDM ; ^{18}F-FDG

Assessment of calcification in atherosclerosis with Dynamic ^{18}F-FDG-PET/CT imaging in elderly subjects

Mamdouh S. Al-enezi, Redha-alla Abdo, Mohamed Yazid Mokeddem, Faiçal A. A. Slimani, Abdelouahed Khalil, Tamas Fulop, Eric Turcotte, M'hamed Bentourkia

Abstract:

Glucose metabolism in atherosclerotic arteries has been shown to be an indicator of inflammation, which might be a precursor of plaque rupture. In this prospective study, we assessed the correlation between artery calcification and glucose metabolism by means of ^{18}F-FDG PET/CT imaging in elderly subjects. Nineteen elderly subjects, with age ranging from 65 to 85 years, underwent CT and dynamic ^{18}F-FDG-PET imaging. The artery calcification was determined with a threshold of 130 Hounsfield units (HU). Intensity of calcification and ratio of calcification area to total artery area were classified in four sequential classes from CT images. The CT artery images were also classified as having single or multi-spot calcifications. Their respective glucose metabolism was assessed with fractional uptake rate (FUR). Factor analysis was used in this study to separate blood images from tissue to extract the blood time activity curves for FUR calculations. The artery images in PET data were corrected for partial volume effect. The total arterial segments analyzed were 1332, with 1085 without calcification (81%), 247 (19%) with calcification, and 94 segments were having multi-spot of calcifications. There was a statistically significant difference in FUR values between non-calcified to calcified segments and between subjects under medication to non-medication when comparing the subjects based on calcification area. No statistically significant differences of FUR were found between single spot clusters as a function of intensity, while in the multi-spots, there was a statistically significant difference for all artery segments. Metabolic activity varies for non-calcified to calcified segments ($P<0.05$). Based on the metabolic activity represented by FUR, calcifications in multi-spots have different effects than in single spots ($P<0.05$).

Key Words: Atherosclerosis; Calcification; Arteries, Plaque; PET; PET/CT; ^{18}F-FDG.

Introduction

Atherosclerosis is a vascular inflammatory disorder and is considered a major cause of cardiovascular diseases and severe events including sudden death [1]. It is characterized by the accumulation of inflammatory cells and oxidized lipids within the vessel wall, causing the construction of the plaque [2] [3] [4] .

The plaque development is a long and dynamic slow process, which might complicate the effort for early diagnosis. Therefore, there is neither standardized approach for early diagnosis nor for plaque stability level [5]. Identifying the vulnerable plaque would reduce atherosclerosis-associated disability and mortality, however this is yet remaining a major ongoing challenge.

Pharmacological lipid lowering therapy by means of statins and other preventives are available, however, residual risk remains even in patients treated with preventive drug therapies [6] [7] [8].

Lumenographic techniques, like intravascular ultrasound**,** digital subtraction angiography and magnetic resonance angiography allow for absolute quantification of the plaque and its components, but they are still unable to detect vulnerable plaque [5] [8] [9]

In the hematological point of view, there are several systemic inflammatory biomarkers being established for atherosclerosis inflammation, among them the C-reactive protein (CRP) which is correlated with increased risk of cardiac events [10] [11]. Unfortunately, the biomarkers together with CRP suffer poorness of information in terms of the plaque localization, level of stabilization and specificity to atherosclerotic inflammation.

Framingham is one example of diagnostic criteria available for identifying population at risk, with low reliability for an individual patient and lack of differentiability of acute cardiovascular risk and chronic stable risk [11] [12].

Most of the analytical studies in regard of atherosclerosis disease are for oncology patients, while the impact of anticancer medical therapies in tracer uptake could influence the accuracy and reproducibility of the analysis [13]. Moreover, neglecting the effect of partial volume might causes noticeable influence on the accuracy of quantitative PET analysis, especially for artery size < 2 to 3 times FWHM of PET scanner [14].

In the present work, we report the correlation between ^{18}F-FDG uptake in the arteries as a function of plaque intensity and calcification area with single and multi-spots of calcifications. These parameters were also evaluated as a function of medication with Rosuvastatin and medication for chest angina.

Materials and methods:

Subjects' measurements

We recruited 19 subjects with age ranging from 65 to 85 years (69.15 ± 3.7). Six subjects were considered as healthy, eight subjects were having hypercholesterolemia (H), and five were having chest angina (A). The subjects were classified as non-medication and under-medication groups. Subjects in under-medication group were under Rosuvastatin, 20 mg/day for one year in group H, and other anti-inflammatory drugs in group A.

The measurement of glucose, total cholesterol, low density lipoprotein, high density lipoprotein, triglyceride and CRP were performed for each subject after overnight fasting. Subjects were injected intravenously with an ^{18}F-FDG bolus at a dose of 140 to 400 MBq depending on the subject's weight. PET and CT were performed with a PET/CT system (Philips Gemini TF 16). Imaging started with non-enhanced low-dose CT (120 kV) which was used for PET attenuation correction and artery calcification detection. CT images were reconstructed in sets of transaxial 512×512 matrixes with a pixel size of 1 mm×1 mm. The PET scans were initiated in dynamic mode for 30 min and were divided into 26 consecutive time frames of 12×10 secs; 8×30 secs; 6×240 secs. PET slices were reconstructed into a 144×144 matrixes, and the voxel size was 4×4×4 mm. The arteries scanned were the aorta and iliac (left and right).

Image analysis

CT images were evaluated visually for the presence of vascular calcification defined according to a threshold of 130 Hounsfield units (HU) for the disclosure of calcification [15]. Thereafter, each lesion was classified within intensity intervals in HU based on the Agatston scale [15].

The classes of intensities (CI) in the CT artery image were defined as: CI0, with no calcification, i.e. pixel intensities below 130 HU; CI1, intensities between 130-199 HU; CI2, 200-299 HU; CI3, 300-399 HU; and CI4, intensity > 400 HU.

The area of calcification was measured for each artery segment as a ratio of calcification area (RCA), defined as an area of at least 2 adjacent pixels >130 HU to total arterial area and expressed as a percentage (%) [16] [17]. Subsequently, the RCAs were subdivided in four classes as for CI with the help of the Ward's clustering method [18]: RCA0 = absence of calcification; RCA1: ≤ 10%; RCA2: 11% - 20%; RCA3: 21% - 30%; RCA4: > 30%.

Fractional uptake rate (FUR) was used in this study to quantify ^{18}F-FDG uptake in PET images. It is an approximated value to Patlak slope and is independent of the body size and gender [19]. $FUR = \frac{C(T)}{\int_0^T C_p(t)dt}$ where T is the time at the mid-frame time, C(T) and $C_p(t)$ are the PET artery image counts and input function, respectively [20], the FUR measurements were done in PET images of the last 3 data points of the time activity curve.

Factor analysis (FA) was used to derive the input function from the sagittal view of the aorta (Figure 5.1.) [21].

For partial volume correction purposes, artery diameters were extracted from CT transaxial images of pixel size 1×1 mm^2. For PET images, the artery diameter was assessed from the first 60 sec of the dynamic transaxial PET images where the images are mainly made of blood, and also from the FA blood images. In this case, the images of the arteries were fitted with 2D Gaussians and the full-width at half maximum (FWHM) averaged in the two orthogonal directions and assumed as artery diameter [22]. The artery transaxial images in PET measurements were corrected for partial volume effect based on the study in [23] made in our center using the same PET/CT scanner.

The measurement of the mean in the region of interest (ROI) was made over the pixels in the ROI having intensity above 70% of the maximum to avoid the influence of image noise for single pixel measurement as well as background contribution [24].

We have corresponded the CT and PET slices by matching their slice positions to avoid interpolation uncertainties during image co-registration. The analyses were then performed on the 512×512 CT images and on the 144×144 PET images.

Statistical analysis

The statistical analyses were performed with the aid of analysis of variance ANOVA for unpaired multi-groups and with the Student t-test for the comparison of unpaired two groups. A p value <5% was considered statistically significant.

Results:

The total arterial segments analyzed in this study were 1332[4], with 1085 segments were not calcified (81%) and 247 (19%) were having calcification. 153 (62%) of the calcified segments were occupied with a single-spot (SS) calcification (Table 5.1.), and 94 (38%) with multi-spot calcifications (MS) (Table 5.2.). The 94 artery segments with MS had a total of 231 calcification spots. From Table 5.1 for SS, it appears that most calcifications with smaller area have low intensity, and those with larger area have high intensity. In the case of MS artery calcifications, the calcifications were found made mostly of smaller areas. The largest area (RCA4) was found in only 8 segments with MS calcifications, independently of their intensity.

Table 5.1 Distribution of ratio of artery calcification (RCA) versus classes of intensities (CI) for single-spot (SS) artery calcification.

	RCA1	RCA2	RCA3	RCA4	Total
CI1 or SS1	30	3	2	0	35
CI2 or SS2	22	27	1	0	50
CI3 or SS3	1	13	9	8	31
CI4 or SS4	0	6	18	13	37
Total segments	53	49	30	21	153

---

[4] The arteries were visually identified on CT and verified with both a CT atlas and correspondence PET slices of first 6 frames. Thereupon, the arterial edges were carefully identified using active contour algorithm.

Table 5.2 Distribution of ratio of artery calcification (RCA) versus classes of intensities (CI) for multi-spot (MS) artery calcifications.

	RCA1	RCA2	RCA3	RCA4	Total
CI1 or MS1	75	2	1	0	78
CI2 or MS2	52	13	2	0	67
CI3 or MS3	12	17	12	3	44
CI4 or MS4	10	17	10	5	42
Total segments	149	49	25	8	231

Figure 5.1. depicts an example of the decomposition with FA into blood and tissue of a PET artery image. The blood curve in Figure 5.1b was used as the input function in FUR calculation.

Figure 5.2. shows an example of CT image of the aorta having two spots of calcification and its corresponding PET image. The CT and PET images were matched based on their scanning slice positions. Figure 5.3. shows an artery with 4 calcification spots segmented with active contours and classified from 1 to 4 based on their mean intensities.

The statistical comparison between calcified and non-calcified arteries showed a statistically significant difference in their FUR values (FUR mean of calcified = 0.0829 and 0.0727 of non-calcified, $p < 0.05$) (Figure 5.4.a). In this figure, the calcified data included the single-spot and multi-spot calcifications and the artery segments of subjects under medication and non-medication. Figure 5.4.b was obtained with the same manner as in Figure 5.4.a but without inclusion of arteries of subjects under medication, and still the two sets of data were found statistically significantly different (FUR mean of calcified = 0.0829 and 0.0762 of non-calcified, $p < 5\%$). Figure 5.4.c was obtained in all calcified artery segments but classified as having calcifications with single spots versus those having multi-spots (FUR mean of calcified = 0.0756 and 0.0827 of non-calcified, $p < 5\%$). From these data, it can be concluded that: 1) medication lowers uptake of ^{18}F-FDG in the arteries; 2) in the absence of medication, the calcification lowers ^{18}F-FDG uptake; and 3) artery segments with multi-spot calcifications accumulates more ^{18}F-FDG than those with single spot calcification.

Figure 5.5.a shows FUR values for the four intensity classes of arteries having single-spot calcification in the medicated and non-medicated subjects. Figure 5.5.b depicts the FUR values as a function of the four classes of area ratios (RCA) still in the arteries with a single spot calcification. From these figures, and apart from the values in Figure 5.5.a for SS3, the results show a decline of glucose metabolism in high intensity calcification and in large area calcification for single-spot calcifications. The statistical difference between non-medication to under-medication was not significantly different based on intensity (p=0.2378, Figure 5.5.a), while it was different based on the area ratios (p=0.0089, Figure 5.5.b).

By grouping artery segments for single-spot and multi-spot calcifications, and by plotting FUR as a function of intensity classes CI and area classes RCA, the medications were still shown to lower FUR (Figure 5.6.). FUR values appeared with a slight increase as a function of the extent of the calcification.
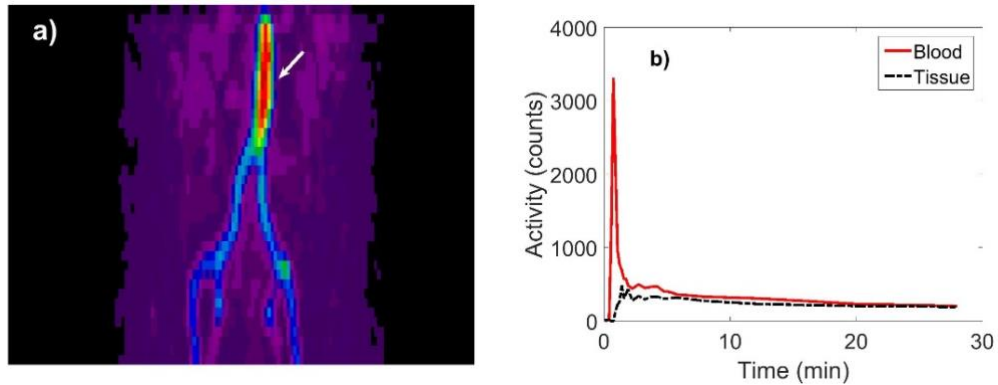
Figure 5.1 a) Sagittal view of the blood FA image with aorta indicated with the white arrow. b) Blood and tissue time activity curves extracted from aorta FA images.
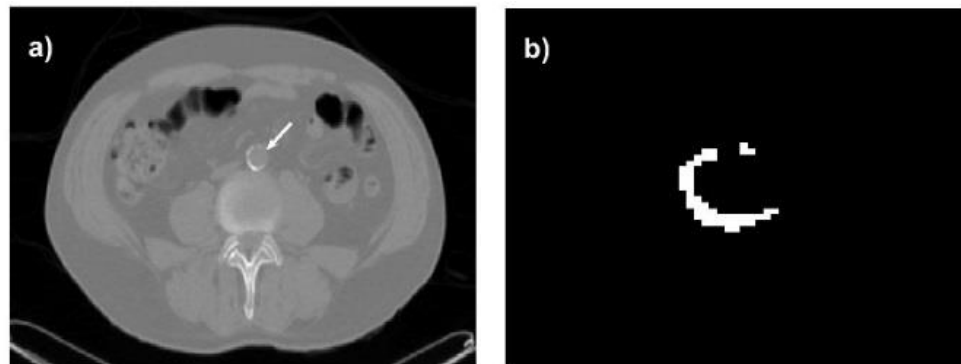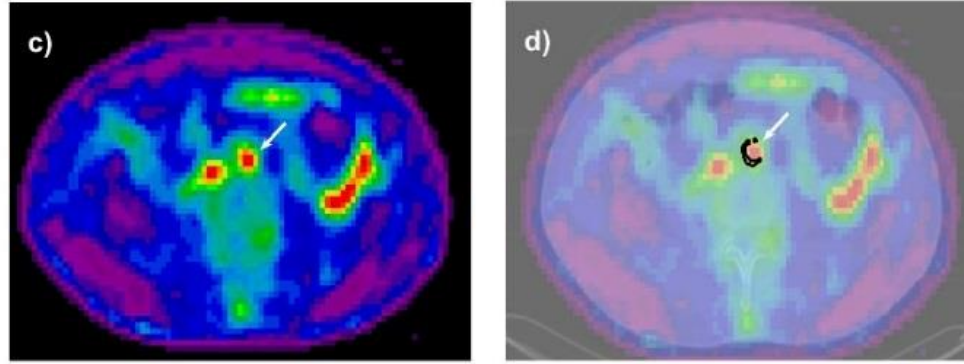
Figure 5.2 a) CT image with calcified aorta (white arrow). b) Segmented calcification spots. c) Corresponding PET image slice with the aorta indicated with the white arrow. d) Fused PET/CT for display only, with overlapping ^{18}F-FDG signal and calcification (black arc) (white arrow). All displayed images were differently zoomed.
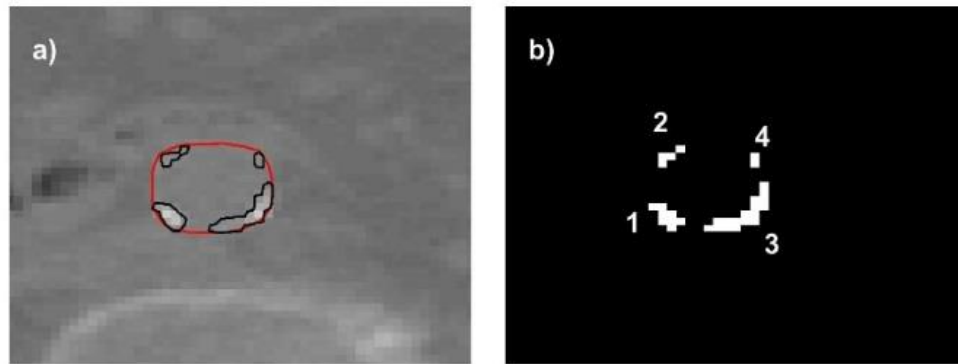
Figure 5.3 a) CT artery image with multi-spot calcifications extracted by utilizing active contour. b) The numbers on each spot represent its class corresponding to their mean CT numbers.
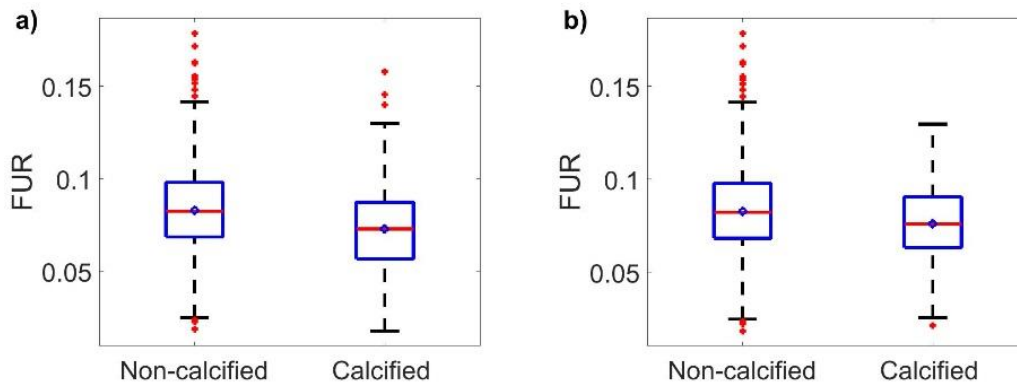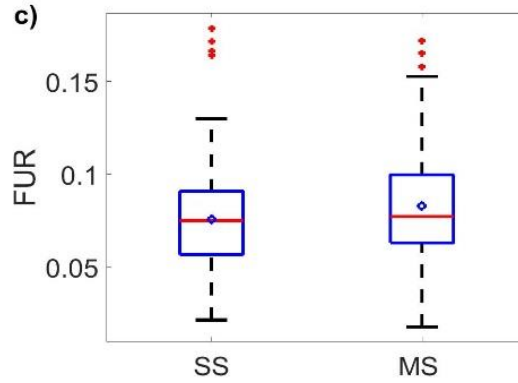
Figure 5.4 a) FUR for non-calcified to calcified segments (p<0.05). All artery segments were included. The circle near the line of the median indicates the mean. The dots above and below the quantiles represent outliers. b) Same as in a) but with excluding artery segments of subjects under medication (p<0.05). c) Comparison of all calcified artery segments as having single calcification spot SS versus those having multi-spot calcifications MS (p<0.05).
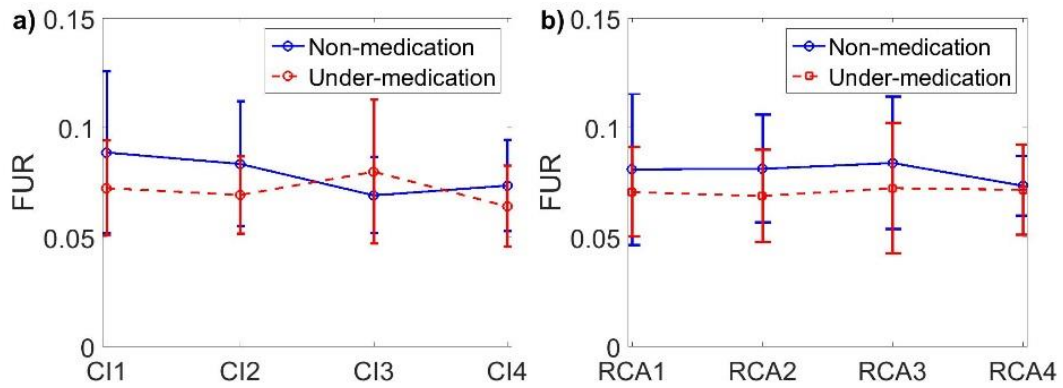
Figure 5.5 a) FUR values in the four intensity classes of arteries identified with single-spot (SS) calcification. b) Same in the four area classes. In both figures, the curves were shown in groups of subjects with and without medication.

The differences of the means between non-medication and under-medication were not statistically significantly different for calcification intensity in a) (p=0.2378), but they were different in b) (p=0.0089).

In overall, medication lowers FUR, and high intensity calcifications show decreased FUR while large area calcifications tend to increase FUR.
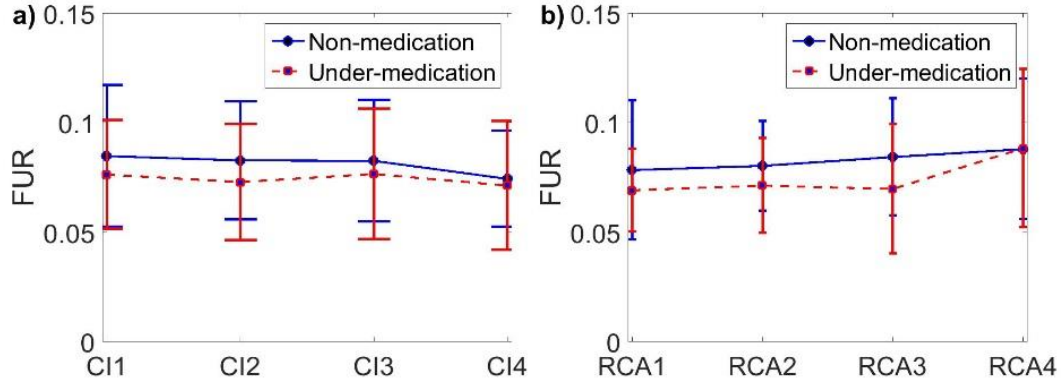
Figure 5.6 a) FUR values for mixed SS and MS versus the four intensity classes (CI). b) Same in the four area classes.

Discussion:

Detection of artery inflammation in atherosclerosis with ^{18}F-FDG-PET remains controversial. The main reasons are thus more technical such as imaging protocol, image reconstruction and filtering, data acquisition mode, image correction for partial volume effect, image co-registration with CT to define the arteries, region of interest drawing, concentration of ^{18}F-FDG in plasma (input function), and the method of analysis which should be more quantitative than standard uptake value (SUV) and tissue-to-blood ratio. For example, the image reconstruction and filtering smooth the images and lacks in image resolution to delimit the arteries. Image co-registration destroys the calcification extent in transaxial and axial slices by interpolating pixels intensity, and vice-versa, it affects PET image intensities if PET images have to be reported to CT images.

The assessment of PET signal for atherosclerosis was mostly carried in a semi-quantitative manner that could minimize the information obtained. Yet, most of published studies for atherosclerosis using PET imaging modality are either oncologic patients, where the influence of anticancer therapies couldn't be neglected, or by using the animal model to resemble human atherosclerosis, where the mouse is the predominant specie in the experimental atherosclerosis studies. Animals are differing from human atherosclerotic plaque and lack some approved vulnerable features of human plaque such as neovascularization and hemorrhage. Additionally, most studies predominantly condone the correction of partial volume that is a predominant factor affecting the accuracy of tracer's

uptake particularly for small lesions (< 2 FWHM). Thus, this could lead to under-estimation of uptake.

Several authors observed a decline of ^{18}F-FDG uptake as a function of calcification severity [13] [25] [26], while others showed its increase [27] [28] [29]. Others reported no correlation between ^{18}F-FDG and volume of calcifications [30] [31]. Some authors, including these cited above, targeted more unstable plaques than calcifications. Lastly, ^{18}F-FDG uptake of other resident cell types, smooth muscle cells and hypoxia would weaken the specificity of ^{18}F-FDG to macrophages [29] [32].

The present study aims were to show how ^{18}F-FDG varies with calcification intensity and volume (area multiplied with slice thickness) in subjects under medication and non-medication. We identified each calcification with its intensity and volume without the recourse to image co-registration. Apart from the clear difference provided with the effect of medication [33] [8], the rest of the results remains debatable.

Indeed, calcification is a disputable feature of being a cause of either stabilization or destabilization of the plaque.

The plaque was thought to healed and stabilized through different mechanisms including calcification (Dweck *et al.*, 2016), therefore, vascular calcifications were postulated more likely to quiesce than causing a clinical event.

However, calcification may also lead to vicious cycle of inflammation and arterial calcification driving disease progression (Nadra *et al.*, 2005). The area of calcification was reported to be correlated with plaque burden (Sangiorgi *et al.*, 1998; Marquering *et al.*, 2011). Increasing area of calcification was seen to be associated with a higher intraplaque hemorrhage (IPH) in 239 studied subjects (van den Bouwhuijsen *et al.*, 2015), where, IPH is associated with a risk of plaque rupture (Saba *et al.*, 2019). The calcification area was also reported to be associated with increased cardiovascular disease risk (Blomberg *et al.*, 2017). Additionally, long-term studies consisted of 25,235 (Budoff *et al.*, 2007) and 125 (Bellasi *et al.*, 2016) patients have shown that the increasing calcification burden worsening long-term survival as a result of the increased complexity of calcification influence in atherosclerosis complication. A study conducted a total of 66,636 asymptomatic adults in a follow-up of 12.3±3.9 years (Peng *et al.*, 2020) noted that patients with extensive calcification scores

represent a very high-risk mortality outcome. For 4180 subjects who were evaluated for stroke events (Hermann *et al.*, 2013), the patients suffering a stroke had significantly higher calcification scores at baseline than the remaining patients, in 9715 asymptomatic patients, the extent of calcification scores were also reported to be accurately predicts 15-year mortality (Shaw *et al.*, 2015).

After all paradoxical findings, we should be skeptical making a firm conclusion regarding the stabilization of plaques caused by calcification and these contradictory outcomes might because all of these calcification areas and score analyses were qualitative in each study. Additionally, calcification of differential shapes, area and locations may act as a marker of a stable plaque, whereas, other forms might identify an unstable vascular environment (Shi *et al.*, 2020).

Concisely, the influence of calcification is may local dependent (Wu, Pei and Li, 2014) rather than global, thus, of each may lead to different clinical consequences (Li *et al.*, 2007), therefore, the findings in respects to calcification emphasised the need of classifying the calcification to their relative prognostic values and they are worthy to be discriminated from one another (Blaha *et al.*, 2017). These different manifestations of calcification would be best incorporated in considering the calcification quantification.

Intriguingly, spotty calcification has identified to be one of the vulnerable plaque features (Ehara *et al.*, 2004). We have demonstrated herein a clear correlation with inflammation seen by ^{18}F-FDG and multi-spots calcifications.

The difference between artery segments having single spot or multi-spot calcifications, and between those having small or large volume, have to be considered at the same level as calcification scores [12] [15]. We demonstrated in this work that calcifications with high intensity and/or with large volume in a single spot calcification behave differently from arteries with multi-spot calcifications. The rise of ^{18}F-FDG uptake in multi-spot calcification arteries, i.e. with larger volume, might be due to its exposure to high level of shear stress which can result in plaque instability [6]. In the same point of view, it has been reported that microcalcifications within the plaque would produce an increase in peak circumferential stress, transforming the plaque into a vulnerable plaque [34] [35]. Finally, the calcification

was suggested to be associated with remodeling and plaque expansion, but without inflammation [36], translating a low uptake of ^{18}F-FDG.

This longitudinal trial has some limitations. Small number of subjects that may not enough statistically, and a larger study population is needed. The arterial diameters were computed either by the CT images or estimated using FWHM of reconstructed PET images for partial volume effect correction and might under or overestimate corrected activity within the selected region, therefore, enhanced CT images would overcome such a source of uncertainty.

Conclusion:

Metabolism activity varies for non-calcified to calcified segments and with medication. FUR for multi-spot calcification correlated with larger calcification area. Under the point of view of metabolic activity represented by FUR, calcifications with multi-spots have different effect than single spot.

Major findings of the research:

The main objective is to investigate either calcification is a marker of inflammatory cascade that is identified by FUR of ^{18}F-FDG, therefore, led to vulnerable plaque identification, or it is a marker of plaque stability. The calcification was clustered as a function of maximum density, area, and shapes of calcification. We demonstrated that spotty of calcification was correlated with inflammation and calcification area but not the density of calcification.

Acknowledgment:

Conflicts of interest:

There are no conflicts of interest.

References:

[1] R. Virmani, "Atherosclerotic Plaque Progression and Vulnerability to Rupture: Angiogenesis as a Source of Intraplaque Hemorrhage," Arteriosclerosis, Thrombosis, and Vascular Biology, vol. 25, no. 10, pp. 2054–2061, Oct. 2005.

[2] P. Libby, P. M. Ridker, and G. K. Hansson, "Inflammation in Atherosclerosis: From Pathophysiology to Practice," J Am Coll Cardiol, vol. 54, no. 23, pp. 2129–2138, Dec. 2009.

[3] E. A. Osborn, C. W. Kessinger, A. Tawakol, and F. A. Jaffer, "Metabolic and Molecular Imaging of Atherosclerosis and Venous Thromboembolism," Journal of Nuclear Medicine, vol. 58, no. 6, pp. 871–877, Jun. 2017.

[4] C. Costopoulos, T. V. Liew, and M. Bennett, "Ageing and atherosclerosis: Mechanisms and therapeutic options," Biochemical Pharmacology, vol. 75, no. 6, pp. 1251–1261, Mar. 2008.

[5] M. Naghavi, M. Madjid, M. R. Khan, R. M. Mohammadi, J. T. Willerson, and S. W. Casscells, "New developments in the detection of vulnerable plaque," Current Atherosclerosis Reports, vol. 3, no. 2, pp. 125–135, Mar. 2001.

[6] N. Nighoghossian, L. Derex, and P. Douek, "The vulnerable carotid artery plaque: current imaging methods and new perspectives," Stroke, vol. 36, no. 12, pp. 2764–2772, 2005.

[7] G. Pugliese, C. Iacobini, C. B. Fantauzzi, and S. Menini, "The dark and bright side of atherosclerotic calcification," Atherosclerosis, vol. 238, no. 2, pp. 220–230, Feb. 2015.

[8] J. H. Revkin, C. L. Shear, H. G. Pouleur, S. W. Ryder, and D. G. Orloff, "Biomarkers in the prevention and treatment of atherosclerosis: need, validation, and future," Pharmacol Rev, vol. 59, no. 1, pp. 40–53, 2007.

[9] D. R. J. Owen, A. C. Lindsay, R. P. Choudhury, and Z. A. Fayad, "Imaging of Atherosclerosis," Annu Rev Med, vol. 62, pp. 25–40, 2011.

[10] R. R. S. Packard and P. Libby, "Inflammation in atherosclerosis: from vascular biology to biomarker discovery and risk prediction," Clin. Chem., vol. 54, no. 1, pp. 24–38, Jan. 2008.

[11] T. M. Brown and V. Bittner, "Biomarkers of atherosclerosis: Clinical applications," Current Cardiovascular Risk Reports, vol. 3, no. 1, pp. 23–30, 2009.

[12] N. Alexopoulos and P. Raggi, "Calcification in atherosclerosis," Nat Rev Cardiol, vol. 6, no. 11, pp. 681–688, 2009.

[13] X. Li et al., "Association Between Osteogenesis and Inflammation During the Progression of Calcified Plaque Evaluated by 18F-Fluoride and 18F-FDG," J. Nucl. Med., vol. 58, no. 6, pp. 968–974, 2017.

[14] D. Izquierdo-Garcia et al., "Comparison of Methods for Magnetic Resonance-Guided [18-F] Fluorodeoxyglucose Positron Emission Tomography in Human Carotid Arteries," Stroke, Jan. 2009.

[15] A. S. Agatston, W. R. Janowitz, F. J. Hildner, N. R. Zusmer, M. Viamonte, and R. Detrano, "Quantification of coronary artery calcium using ultrafast computed tomography," Journal of the American College of Cardiology, vol. 15, no. 4, pp. 827–832, 1990.

[16] M. Ohya et al., "Vascular calcification estimated by aortic calcification area index is a significant predictive parameter of cardiovascular mortality in hemodialysis patients," Clin Exp Nephrol, vol. 15, no. 6, pp. 877–883, Dec. 2011.

[17] N. van der Bijl et al., "Assessment of Agatston Coronary Artery Calcium Score Using Contrast-Enhanced CT Coronary Angiography," American Journal of Roentgenology, vol. 195, no. 6, pp. 1299–1305, Dec. 2010.

[18] J. J. Macnab, L. T. Miller, and H. J. Polatajko, "The search for subtypes of DCD: is cluster analysis the answer?" Hum Mov Sci, vol. 20, no. 1–2, pp. 49–72, Mar. 2001.

[19] M. Rutland, L. Que, and I. M. Hassan, "'FUR' – one size suits all," Eur J Nucl Med, vol. 27, no. 11, pp. 1708–1713, Nov. 2000.

[20] K. Ishizu et al., "Effects of hyperglycemia on FDG uptake in human brain and glioma," J. Nucl. Med., vol. 35, no. 7, pp. 1104–1109, Jul. 1994.

[21] M. Bentourkia, "PET kinetic modeling of 11C-acetate from projections," Comput Med Imaging Graph, vol. 27, no. 5, pp. 373–379, Oct. 2003.

[22] A. N. Christensen et al., "Calibrated image-derived input functions for the determination of the metabolic uptake rate of glucose with [18F]-FDG PET," Nucl Med Commun, vol. 35, no. 4, pp. 353–361, Apr. 2014.

[23] E. Croteau et al., "Image-derived input function in dynamic human PET/CT: methodology and validation with 11C-acetate and 18F-fluorothioheptadecanoic acid in muscle and 18F-fluorodeoxyglucose in brain," Eur J Nucl Med Mol Imaging, vol. 37, no. 8, pp. 1539–1550, Aug. 2010.

[24] M. A. Lodge, M. A. Chaudhry, and R. L. Wahl, "Noise Considerations for PET Quantification Using Maximum and Peak Standardized Uptake Value," J Nucl Med, vol. 53, no. 7, pp. 1041–1047, Jul. 2012.

[25] N. Hiari and J. H. F. Rudd, "FDG PET imaging and cardiovascular inflammation," Curr Cardiol Rep, vol. 13, no. 1, pp. 43–48, Feb. 2011.

[26] J. Wassélius, S. Larsson, and H. Jacobsson, "Time-to-time correlation of high-risk atherosclerotic lesions identified with [18F]-FDG-PET/CT," Ann Nucl Med, vol. 23, no. 1, pp. 59–64, Jan. 2009.

[27] "18F-FDG PET/CT Identifies Patients at Risk for Future Vascular Events in an Otherwise Asymptomatic Cohort with Neoplastic Disease." [Online]. Available: http://jnm.snmjournals.org/content/50/10/1611.full. [Accessed: 06-Sep-2018].

[28] Y.-W. Wu et al., "Characterization of Plaques Using 18F-FDG PET/CT in Patients with Carotid Atherosclerosis and Correlation with Matrix Metalloproteinase-," p. 8.

[29] J. H. F. Rudd et al., "Imaging atherosclerotic plaque inflammation with [18F]-fluorodeoxyglucose positron emission tomography," Circulation, vol. 105, no. 23, pp. 2708–2711, 2002.

[30] R. M. Kwee et al., "Multimodality imaging of carotid artery plaques: 18F-fluoro-2-deoxyglucose positron emission tomography, computed tomography, and magnetic resonance imaging," Stroke, vol. 40, no. 12, pp. 3718–3724, Dec. 2009.

[31] A. Tawakol et al., "In vivo 18F-fluorodeoxyglucose positron emission tomography imaging provides a noninvasive measure of carotid plaque inflammation in patients," J. Am. Coll. Cardiol., vol. 48, no. 9, pp. 1818–1824, Nov. 2006.

[32] E. J. Folco et al., "Hypoxia but not inflammation augments glucose uptake in human macrophages: Implications for imaging atherosclerosis with 18fluorine-labeled 2-deoxy-D-glucose positron emission tomography," J. Am. Coll. Cardiol., vol. 58, no. 6, pp. 603–614, Aug. 2011.

[33] N. Tahara et al., "Simvastatin attenuates plaque inflammation: evaluation by fluorodeoxyglucose positron emission tomography," J. Am. Coll. Cardiol., vol. 48, no. 9, pp. 1825–1831, Nov. 2006.

[34] N. Maldonado, A. Kelly-Arnold, D. Laudier, S. Weinbaum, and L. Cardoso, "Imaging and analysis of microcalcifications and lipid/necrotic core calcification in fibrous cap atheroma," Int J Cardiovasc Imaging, vol. 31, no. 5, pp. 1079–1087, Jun. 2015.

[35] J. F. Wenk, P. Papadopoulos, and T. I. Zohdi, "Numerical modeling of stress in stenotic arteries with microcalcifications: a micromechanical approximation," J Biomech Eng, vol. 132, no. 9, p. 091011, Sep. 2010.

[36] A. P. Burke, F. D. Kolodgie, A. Farb, D. Weber, and R. Virmani, "Morphological predictors of arterial remodeling in coronary atherosclerosis," Circulation, vol. 105, no. 3, pp. 297–303, Jan. 2002.

6. ARTICLE 2

Kinetic modeling of dynamic PET-^{18}F-FDG in elderly with atherosclerosis without blood sampling

Mamdouh S. Al-enezi, M'hamed Bentourkia

Contribution of the student: Mamdouh S. Al-Enezi has performed the analysis for this project and the preparation of the first draft.

Résumé:

L'athérosclérose est une maladie affectant les artères périphériques et qui se caractérise par l'accumulation des dépôts de lipides et des cellules immunitaires pour former la plaque d'athérome. La plaque calcifiée est facilement détectable et mesurable avec l'imagerie TDM et l'inflammation de cette plaque peut être quantifiée avec l'imagerie dynamique TEP en utilisant le radiotraceur ^{18}F-FDG. Étant donné que les parois artérielles sont trop petites et dominées par l'activité dans le sang, le modèle compartimental conventionnel devient inadéquat pour modéliser le métabolisme artériel, surtout lorsque nous utilisons une fonction d'entrée dérivée d'une image à partir d'une artère. L'objectif de cette étude est d'évaluer quantitativement le métabolisme du glucose dans les artères avec une modélisation compartimentale plus appropriée. La modélisation cinétique des artères a été effectuée à l'aide du modèle compartimental classique du ^{18}F-FDG et du modèle modifié sans avoir besoin d'échantillonnage sanguin. Le taux métabolique de glucose (MRG) a été calculé par segment d'artère dans chaque tranche d'image avec les deux modèles. Le rapport des scores de calcification de la zone (RCA) et de calcification d'Agatston (ACS) ont été automatiquement classifiés en utilisant l'algorithme K-means. Les constantes de temps ont montré une variation significative entre les deux modèles ($p < 0,05$), alors que le débit du flux net (K_i) était en bon accord pour les deux modèles ($p > 0,05$). Du point de vue statistique, les deux modèles ont révélé que les valeurs de MRG dans le groupe des sujets ne prenant pas de médicament étaient significativement différentes de celles dans le groupe sous médicaments.

Mots Clés : TEP; TEP/TDM; ^{18}F-FDG; Modélisation cinétique; Athérosclérose; Artère, Inflammation; Calcification.

Kinetic modeling of dynamic PET-^{18}F-FDG in elderly with atherosclerosis without blood sampling

Mamdouh S. Al-enezi, M'hamed Bentourkia

Abstract:

Atherosclerosis is a disease affecting the peripheral arteries characterized by a deposit of lipids and immune cells forming a plaque. The plaque can be calcified and be measured with CT, and it can be inflamed and be measured with PET and ^{18}F-FDG. Since artery walls are too small and are dominated by blood activity, the conventional compartmental model becomes inadequate to provide artery metabolism especially when using an image derived input function from an artery. The purpose of this study was to quantitatively evaluate glucose metabolism in arteries with a more appropriate compartmental modeling. Kinetic modeling of arteries was conducted using the classical ^{18}F-FDG compartmental model and a modification of this model without the need of blood sampling. Metabolic rate of glucose (MRG) was computed per artery segment in each image slice with both models. The ratio of calcification area (RCA) and Agatston calcification scores (ACS) were automatically clustered with the Automatic Hierarchical K-means algorithm. The rate constants showed significant variation between the two models ($p < 0.05$), however, net influx rate (K_i) was with good agreement in both models ($p > 0.05$). Both models found that MRG values in non-medication group were statistically significantly different from those in under-medication group.

Index Terms— PET; PET/CT; ^{18}F-FDG; Kinetic modeling; Atherosclerosis; Artery; Inflammation; Calcification.

Introduction

Atherosclerosis is a lipid-driven inflammatory disease underlying causes of morbidity and mortality worldwide[1]. It affects the peripheral arteries characterized by a deposit of lipids and immune cells forming a plaque. The plaque can harden and be safe all the life of the

individual, or it can be inflamed, rupture and obstruct small blood vessel provoking complications in the brain or the heart.

The most clinical vascular imaging modalities currently used for diagnosing atherosclerosis are conventional X-ray angiography, intravascular ultrasound (IVUS), computed tomography (CT) and magnetic resonance imaging (MRI). They all provide a good anatomical information about the status of vascular lumen and/or vessel wall. Previous findings have shown that due to the positive vascular remodeling, most of ruptured plaques do not significantly obstruct vascular lumen prior to rupture [2][3]. Such plaques, therefore, are hard to be identified using angiography. In addition, IVUS, CT and MRI imaging modalities provide information on vessel wall and plaque components, like fibrous cap thickness, lipid core size and calcification[4],[5]. However, they lack metabolic information and status of plaque vulnerability.

^{18}F-FDG with PET reflects the metabolic activity of macrophages and consequently the degree of plaque inflammation [6]. Yet, metabolic activity by means of aortic ^{18}F-FDG uptake was shown to provide an independent prediction of cardiovascular complication [7].

Kinetic modeling is a mathematical model used to fit the time-activity curve (TAC) of a region of interest (ROI) obtained from dynamic PET images and incorporating an input function (IF) manually sampled or extracted from the images by means of ROIs on heart chambers or arteries, thus allowing the assessment of biological parameters and metabolic activity estimation. The quantitative kinetic features of the ^{18}F-FDG uptake, such as metabolic rate of glucose (MRG) are more reliable and reproducible than semi-quantitative metrics like standard uptake value (SUV) and tissue to blood ratio (TBR) [8], [9]. Although kinetic modeling provides itemized and precise information of the tissue metabolic activity [10], it is not actually predominantly utilized in clinical practice.

The aims of this study were to utilize kinetic modeling of ^{18}F-FDG independently of blood sampling and correction for partial volume effect (PVE). Moreover, the IF was derived from the same ROI to be fitted with the model using factor analysis (other means of image decomposition can be used). This approach allowed to study the arteries themselves and is called hereafter model without blood sampling (WOBS). WOBS model was compared with the classical ^{18}F-FDG 2-tissue compartmental model with conventional method of IF

determination from the images and PVE correction. These analyses were performed in artery images of elderly subjects with atherosclerosis with the aims to correlate MRG with artery calcification. Besides, we have appraised the differences of MRG as a function of ratio of calcification area (RCA) and Agatston calcification scores (ACS) both calculated from CT images. The correspondence of MRG values to RCA and ACS is expected to correlate the artery inflammation to the extent of the calcification (RCA) and to its intensity (ACS). Lastly, we compared data from subject's under-medication for the reduction of artery inflammation and those not taking medication.

Materials and Methods

Subjects' Measurements

The dynamic PET measurements were acquired in ten participants (69.2 ± 3.65 years old) twice a year, making a total of 19 measurements (one participant was scanned a single time). Nine subjects were under medication.

An activity of 140 to 400 MBq of ^{18}F-FDG, normalized to participant's weight, were intravenously injected in subjects and emission data were collected immediately in PET dynamic mode for 30 min (12 × 10 secs, 8 × 30 secs and 6 × 240 secs) and they were attenuation corrected using CT images. PET and CT images were reconstructed using 3D row action maximum likelihood reconstruction algorithm with 144×144 and 512×512 grids, having pixel size of 4 mm × 4 mm × 4 mm and 1 mm × 1 mm × 5 mm for PET and CT, respectively, with a PET/CT system (Philips Gemini TF 16). All participants were following 6-8 hours of over-night fasting. Blood glucose measurement was taken in all recruited participants and was 4.95 ± 0.703 mmol/l (mean ± STD). All participants gave written informed consent for scanning with ^{18}F-FDG-PET and the study protocol was approved by the research ethics committee of the Faculty of Medicine and Health Sciences, University of Sherbrooke, Canada.

Image Analysis

The aorta and iliac artery images were considered on each transaxial slice of CT and PET images. PET image segmentation of the arteries was performed using edge-based

active contours algorithm [11] in the summation of the first 6 early frame images where the arteries were well identified. Arteries on CT images were manually identified and verified with both a CT atlas and correspondence PET slices of first 6 frames. The arterial edges were carefully identified using active contour algorithm as in PET image artery segmentation. The calcification of arteries on CT images was also automatically segmented and its area calculated. The calcification area was used to assess the calcified lesion and calcification scores[12]. Therefore, the calcified lesions were visually identified in the segmented arteries as areas greater than 2 contiguous pixels with intensity greater than 130 Hounsfield units[13]. The quantification of RCA was calculated per arterial segment as the ratio of calcified pixels to total arterial pixels on an image slice. In fact, a pixel in CT image was counted as an area of 1 mm^2. ACS thereafter was computed as the product of calcification area and intensity factors. These factors were assumed to vary from 1 to 4 based on the intensity of the calcification: 130–199 HU assigned as 1, 200–299 HU assigned as 2, 300–399 HU assigned as 3, or $\geq$ 400 HU assigned as 4[14].

MRG was computed by means of the estimated rate constants, glycemia (gl in mg/100ml) and molar mass of glucose [0.18 (g/mmol)] as: MRG=$\frac{gl}{0.18} \times \frac{K_1 k_3}{k_2 + k_3}$ [15]. The lumped constant has been assumed to be unity.

The rate constants were estimated following the classical model as described in [15]. In this case, the IF has been determined from an ROI on the coronal blood image of the aorta extending on several transaxial slices. The blood image was calculated with factor analysis (FA) [16], [17]. IF in each artery image slice was corrected for PVE.

The second approach was based on a model introduced by Bentourkia and it is summarized in [18]. In fact, instead of using IF in a kinetic model, with IF defined by any means, i.e. from blood samples, population or images, in this new model, tissue blood volume (TBV) was used. TBV was defined from FA blood image. Usually, the pharmacokinetic model generates TBV together with the rate constants during the fitting of tissue TACs, in this new model, TBV is evaluated from FA blood images and IF is deduced from TBV during TAC fitting. In the following we write the classical ^{18}F-FDG model (1) [15] followed by the WOBS model (4) [18]:

$$C_{PET}(t) = \frac{K_1}{\alpha_2 - \alpha_1} \left[(k_3 + k_4 - \alpha_1) e^{-\alpha_1 t} + (\alpha_2 - k_3 - k_4) e^{-\alpha_2 t} \right] \otimes IF + k_5 IF \qquad (1)$$

k_5 is a constant <1, and $k_5 IF$ is a fraction of the IF representing TBV of that ROI (TBV $= k_5 IF$). TBV is also the blood component in this same ROI in the image which was defined with FA. By knowing TBV from FA, IF can be obtained as:

$$IF = TBV/k_5 \qquad (2)$$

Substituting this equation in the above we obtain:

$$C_{PET}(t) = \frac{K_1}{\alpha_2 - \alpha_1} \left[(k_3 + k_4 - \alpha_1) e^{-\alpha_1 t} + (\alpha_2 - k_3 - k_4) e^{-\alpha_2 t} \right] \otimes TBV/k_5 + TBV \qquad (3)$$

which becomes, by replacing $1/k_5$ by a constant v:

$$C_{PET}(t) = \frac{K_1}{\alpha_2 - \alpha_1} \left[(k_3 + k_4 - \alpha_1) e^{-\alpha_1 t} + (\alpha_2 - k_3 - k_4) e^{-\alpha_2 t} \right] \otimes vTBV + TBV \qquad (4)$$

In final, equation (4) is independent of IF. In terms of fitting, the classical model (1) fits for 4 rate constants and a constant $k_5 < 1$, while the WOBS model (4) equally fits for the 4 rate constants and a constant $v > 1$.

The advantage of using (4) is that both TBV and C_{PET} are evaluated from the same ROI, thus PVE is cancelled out. Since TBV is extracted from the same ROI to be fitted, the noise in TBV is already contained in the ROI TAC and thus the model more accurately fits the data. As a third advantage, once FA is applied on a 3D image, tissue and TBV can be easily used at the pixel basis or with ROIs in a model, and this provides a gain in time.

The SUV (in arbitrary unit, AU) was calculated as the mean of the artery ROI pixels in the last PET image frame multiplied by the scale *suvscl* extracted from the image header.

Finally, in clustering RCA and ACS, we utilized Automatic Hierarchical K-means algorithm (AHK) [19] and we enhanced its performance with the use of silhouette-coefficient [20].

Statistical Analysis

The goodness of fit between the measured TACs and the model fits was assessed by Pearson's correlation coefficient squared (r^2) in each ROI[21], [22]. Continuous data were

tested for normality using the D'Agostino-Pearson omnibus test[23]. Since the normality was not demonstrated in our data, we opted for the non-parametric data to be compared using Wilcoxon-Mann-Whitney U test and expressed as median with interquartile range (IQR)[23], [24].

The p value < 0.05 considered the threshold for statistical significance. The statistics of the influx constants and MRG values between the applied models and all clustered groups illustrated in this study were analyzed with Wilcoxon-Mann-Whitney U test.

Results

There were 710 artery segments in total from the 19 subjects (mean segments per subject 37 segments, with a minimum of 14 and a maximum of 47 segments per subject). Among these segments, 354 had calcifications with a mean RCA of 0.21 ± 0.14. The number of artery segments from subjects under medication was 315 segments, and under medication with calcification was 203 segments.

Figure 6.1.a shows a CT image slice of the aorta as indicated by the arrow with the ROIs on the whole artery and on the two calcification spots. Figure 6.1.b represents the corresponding PET image slice including the aorta, and Figure.4.1.c was obtained from factor analysis for the blood component of the same slice. Figure 6.1.d depicts the TACs from measured and FA blood image of the ROI drawn around the aorta as shown in Figure 6.1.b and Figure 6.1.c.

Figure 6.2.a shows the diagram of the WOBS model as it is mathematically described in equation (4). The vascular compartment in this figure, when it represents the IF in the classical model, is partially seen by PET (dashed line), while in WOBS model, the whole blood compartment which is reduced to TBV is included in what PET measures (TBV inside dashed line).

In almost the whole TACs, the fit with WOBS model was more accurate than with the classical model (Figure 6.2.b) (p<0.05 with both Student t-test and Mann-Whitney test. WOBS r2: mean $\pm$ STD is 0.995 ± 0.01, median: 0.998, IQR: 0.0046; classical model r2: 0.90 ± 0.05, median: 0.901, IQR: 0.0778). Figure 6.2.c and its zoomed counterpart on the amplitude Figure 6.2.d show the fits to an aorta TAC using WOBS model, and similarly in

Figure 6.2.e and Figure 6.2.f for fits using the classical model with IF extracted from FA images.

With WOBS model (Figure 6.2.d), TBV appears far below the measured and fitted TACs, and the free ^{18}F-FDG (CF curve in green) does not appear having contamination from blood component (peak of green curve not following peak of the bolus injection as in Figure 6.2.f).

Table 6.1. shows the values of K_1 and K_i for WOBS and for the classical model with IF derived from FA. K_1 values with WOBS were statistically significantly different from those of the classical model ($p < 0.05$), while K_i was not different between WOBS and the classical model ($p = 0.41$).
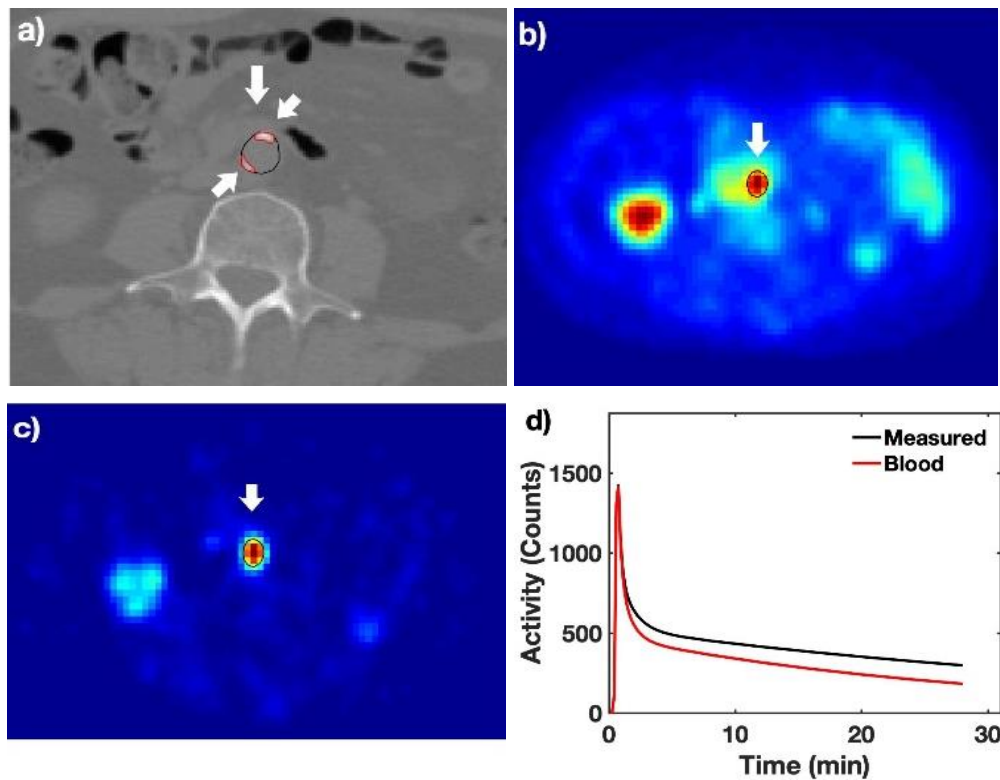
Figure 6.1 a) Trans-axial view of a CT image through the aorta. The arrows indicate the aorta and two calcification spots. b) Corresponding measured PET image. c) Corresponding blood FA image. d) Example of TACs from measured PET image and from blood FA image.
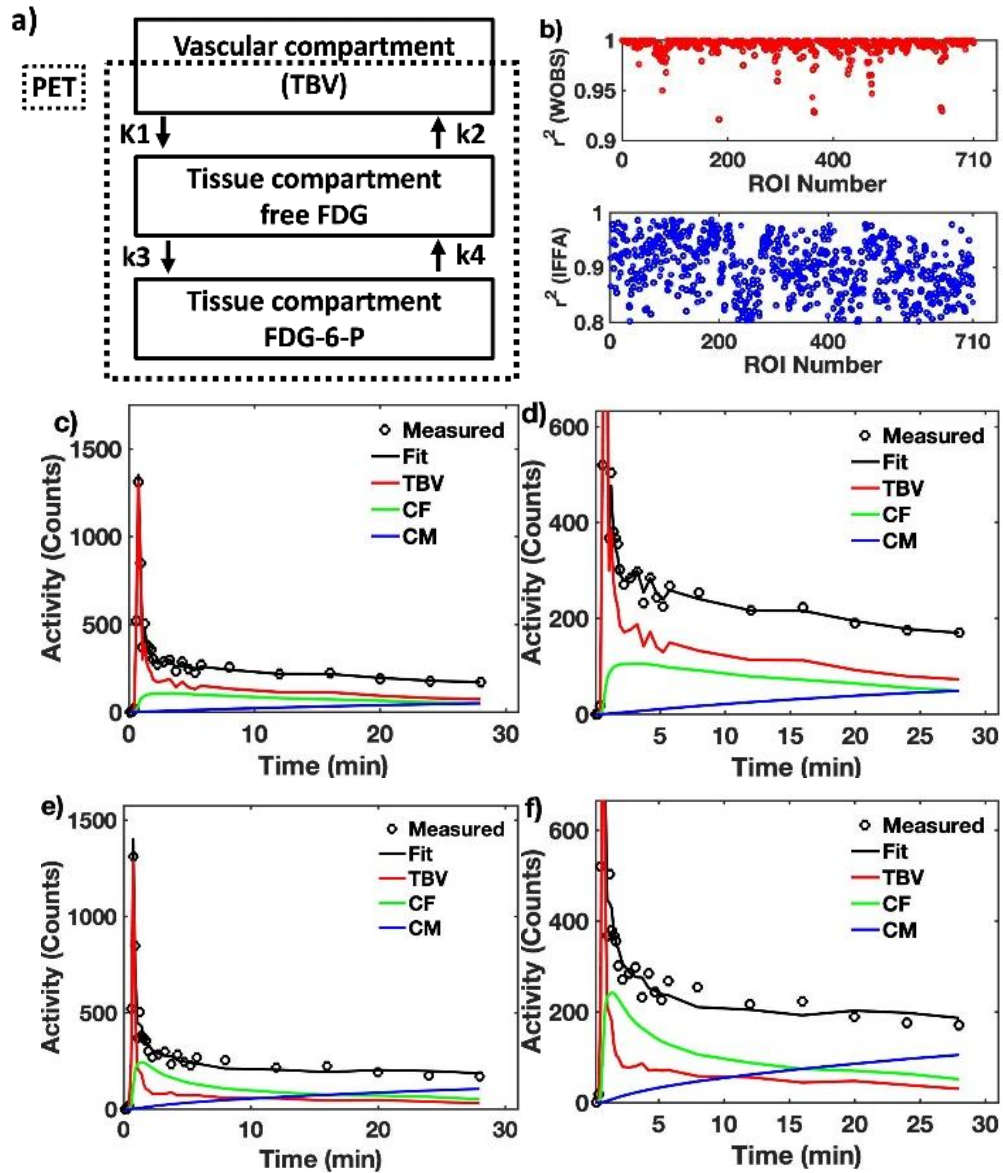
Figure 6.2 a) WOBS model. b) Pearson's correlation coefficient squared (r2) for all TAC fits with WOBS (upper plot) and with the classical model (lower plot). c) TAC fit with WOBS model. d) Same in c) with a zoom on the amplitude. e) and f) Same as in c) and d), respectively, for TAC fit with the classical model.

Table 6.1 Influx constant values estimated using WOBS and classical models. Values were expressed as mean ± STD averaged over all artery segments.

	K_1 (ml/min/g)	K_i (ml/min/g)
WOBS model	0.015 ± 0.013	0.194 ± 0.153
Classical ^{18}F-FDG Model (IF from FA)	0.026 ± 0.011	0.202 ± 0.140

$$K_4 = 0;\ K_i = K_1 k_3/(K_2 + k_3).$$

Figure 6.3 depicts the comparison of MRG values calculated with WOBS (Figure 6.3a) and the classical model (Figure 6.3.b). Within each model as well as with SUV in Figure 6.3.c. There was a significant difference for the effect of medication ($p < 0.05$). However, between the two compartmental models the results did not show differences in either groups of non-medicated or under medication. MRG and SUV values respectively for non-medication and under-medication groups are grouped in Table 6.2.
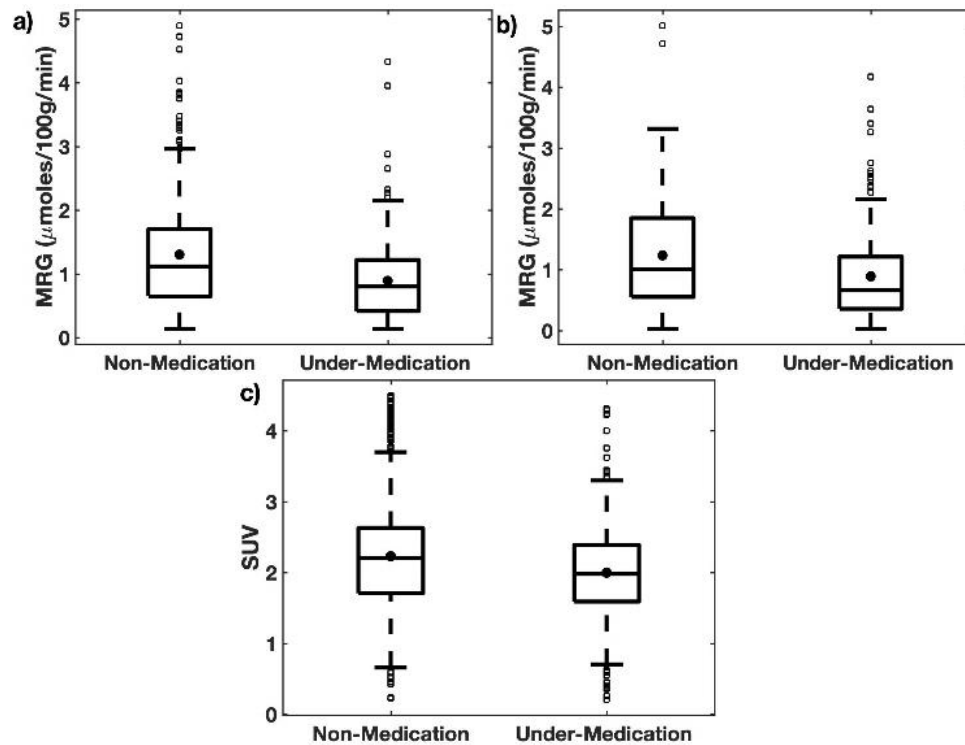
Figure 6.3 Comparison of MRG between non-medicated and under-medication groups assessed with (a) WOBC, (b) classical models and (c) SUV. In both models and SUV, non-medicated and under medication groups were statistically significantly different. ($p < 0.05$).

Table 6.2 Statistics in the groups of non-medicated and under-medication for WOBS and classical models and SUV.

		Non-medication	Under-medication
WOBS	Mean±STD	1.31 ± 0.86	0.89 ± 0.59
	Median	1.12	0.80
	Quartiles	0.65 -1.70	0.42 - 1.22
	IQR	1.05	0.80
Classical	Mean±STD	1.24 ± 0.89	0.90 ± 0.76
	Median	1.01	0.67
	Quartiles	0.55 -1.85	0.36 - 1.21
	IQR	1.30	0.85
SUV	Mean±STD	2.23 ± 0.78	2.00 ± 0.60
	Median	2.21	1.98
	Quartiles	1.71 -2.63	1.60 - 2.40
	IQR	0.92	0.80

- The values of WOBS and classical models are in units of μmoles/100g/min and those of SUV are in arbitrary units.

For the three automatically defined RCA clusters with AHK, the median values of MRG in units of μmoles/100g/min for WOBS model were 0.69 (IQR 0.41 - 1.14), 0.78 (IQR 0.42 – 1.40) and 1.40 (IQR 1.04 – 1.90) in RCA1, RCA2 and RCA3 clusters, respectively. While for classical model, MRG values were 0.60 (IQR 0.20 - 1.12), 0.83 (IQR 0.45 – 1.82) and 1.75 (IQR 0.88 – 2.40) in the same clusters. This indicates that MRG increased with RCA in both models. Higher RCA (RCA3) was significantly different from RCA1 in both models (P<0.05). Figure 6.4 summarizes these results.

In the comparison between the two models with respect to RCA clusters (RCAi in WOBS versus RCAi in classical model), there was no significant difference (p= 0.32, 0.47 and 0.3 for RCA1, RCA2 and RCA3 respectively).

As in RCA, the ACS were clustered with unsupervised AHK and gave 5 clusters. MRG in units of μmoles/100g/min of the 5 clusters for WOBS model expressed as median with IQR were: 0.62 (IQR 0.34 - 1.12), 0.73 (IQR 0.48 – 1.23), 0.81 (IQR 0.42 – 1.35), 1.20 (IQR

0.81 – 1.91) and 1.52 (IQR 1.32 – 1.97). While for the classical model, these values were respectively 0.60 (IQR 0.20 - 1.20), 0.55 (IQR 0.35 – 1.03), 1.12 (IQR 0.46 – 1.83), 1.48 (IQR 0.69 – 2.05) and 2.06 (IQR 0.96 – 2.46).

The higher 2 ACSs were significantly different from the first 2 ACSs groups in both models ($P<0.05$). Figure 6.5 shows a plot of these results.

We compared ACS between the two models (same as in RCA), and there was no significant difference ($p = 0.60, 0.30, 0.36, 0.59$ and 0.38 for ACS1, ACS2, ACS3, ACS4 and ACS5 respectively).
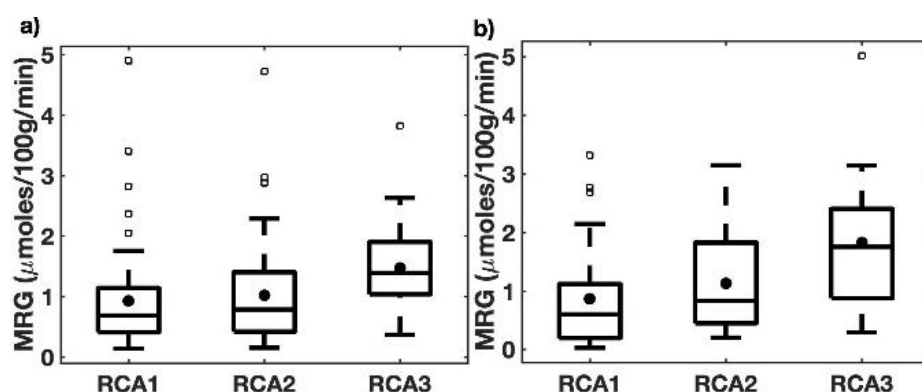
Figure 6.4 MRG as a function of the three clusters of RCA; a) MRG obtained with WOBS model and b) with classical model.
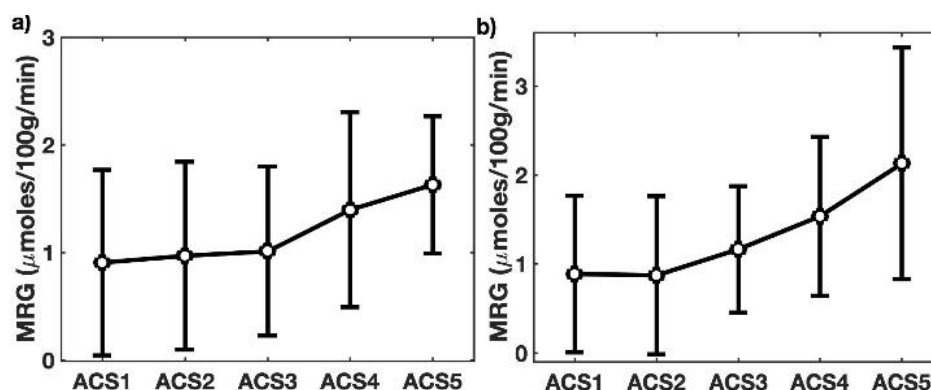
Figure 6.5 MRG as a function of the five clusters of ACS; a) MRG obtained with WOBS model and b) with classical model.

Discussion

Several studies have demonstrated the feasibility of utilizing ^{18}F-FDG pharmacokinetic model and its derived parameters in dynamic PET imaging clinically in oncologic

malignancies. However, no study up to now applied this approach in atherosclerotic disease. The major issue obstructing the use of ^{18}F-FDG model is the time demanding in imaging in addition to blood sampling and its accompanied obstacles[25]. Nonetheless, the reliability of using a short time of PET data acquisition within 30-min compared to the classical 60-min imaging protocol has been demonstrated[26], [27].

In the regards of blood TAC, invasive blood sampling could be appropriately replaced by image derived input function strategies[16], [17]. Partial volume effect due to limited resolution of a clinical PET scanner results in increasing underestimation of activity measured with decreasing volume of interest [28] and to an increased measurement uncertainty of this activity. Having said that, there are plenty of strategies for partial volume correction[29].

Our approach in this study was to exploit the reliability of kinetic modeling independently of blood sampling or common IF derived from images prone to PVE, and concurrently eliminating the impact of partial volume effect (mathematically explained in equation (4)). Several cancer and brain studies used IF defined from arteries such as aorta and carotid. To study the arteries themselves, this approach becomes trivial as an artery IF cannot be used to fit itself in the model. In this study, we also derived an IF from the sagittal measured PET image of the aorta in each subject and applied the classical model and found the values $K_1 = 0.024 \pm 0.011$, $K_i = 0.104 \pm 0.052$ which were statistically significantly different from those obtained with WOBS and with the classical model using IF from FA blood image.

The simple approach for PVE correction is the design of a phantom with cylinders or spheres at the same distance from the phantom center and filled with the same radiotracer concentration. The deficit in intensity in the image of the cylinders is used as recovery factors to correct artery or tumor images depending on their diameters[30], [31]. The other approach is the correction for spill-out by deconvolution which is more demanding. The approach of recovery factors is well suited to imaging of arteries as these appear almost circular on the images. Consequently, since we used the same ROI for TBV and for the artery segment, the recovery factors (RC) cancel out in equation (4):

$$C_{PET}(t) \times RC = \frac{K_1}{\alpha_2 - \alpha_1} \left[\left(k_3 + k_4 - \alpha_1 \right) e^{-\alpha_1 t} + \left(\alpha_2 - k_3 - k_4 \right) e^{-\alpha_2 t} \right] \otimes vTBV \times RC + TBV \times RC.$$

In addition to PVE elimination in WOBS model, and since $C_{PET}(t)$ and TBV are deduced from the same ROI, they are subject to nearly the same noise including subject movement during image acquisition or direct action on the tissue of interest [32]. However, these effects remain to be demonstrated.

We have compared rate constant values estimated using WOBS model with the classical ^{18}F-FDG model and the correlation was obvious over the macro-parameter (K_i, therefore MRG). However, for the rate constants when taken separately, they were having significant variations between the two models. The significant variations in micro-parameters could be explained by the short circulation time (30 min) and different input IFs (per segment blood TACs for WOBS model and single global input IF for classical model). Therefore, if these rate constants were taken as a single block (K_i), they were found with a good agreement in both models. Interestingly, K_i particularly was shown to be excellently independent of such short circulation time influence[27]. Yet, the dependency of K_i on the relations between the rate constants making it (K_i) little affected by the variation between them, which led us having no significant difference in K_i for both models, in the contrary to rate constants, as this has also been demonstrated for ^{18}F-FDG elsewhere [33].

Increasing calcification area was shown to be positively and independently correlated with cardiovascular disease risks but not intensity factors in the study of 3398 participants of multi-center [34]. We have shown that the overall metabolic activity within the arterial segments significantly differed as a function of calcification area but not the intensity.

The Agatston score thereafter (multiplication of intensity factor and calcification area) was clustered with unsupervised AHK and resulted into 5 groups. Higher scores were accompanied with high MRG values.

The metabolic activity in calcified arterial segments were statistically significantly different in non-medication compared to under medication groups in both models.

We finally shall mention that this was a prospective study, and the participants were not oncology patients or taking medication other than those for atherosclerosis.

Conclusions

The modified ^{18}F-FDG model was used without the knowledge of a common IF, and simultaneously eliminated the need to partial volume correction. This model was shown to be comparable to the classical ^{18}F-FDG model.

For atherosclerosis, higher area of artery calcification and calcification score depending on calcification intensity and area were shown to affect glucose metabolism in the arteries. The correlation of glucose metabolism with the combination of calcification area and intensity could be an indicator of plaque vulnerability.

Major findings of the research:

The main objective was to study the feasibility of kinetic modeling application in atherosclerotic settings. We demonstrated the feasibility of using kinetic modeling in atherosclerotic settings with constraints on the input function that should not be extracted directly from the image but rather it should be extracted using factor analysis or other statistical means. We have also found that higher calcification area and higher calcification score were correlated with higher metabolic rate of glucose. Kinetic modeling with WOBS is more appropriate than with the classical model.

Acknowledgment

References

[1]   M. Bäck, A. Yurdagul, I. Tabas, K. Öörni, and P. T. Kovanen, "Inflammation and its resolution in atherosclerosis: mediators and therapeutic opportunities," Nature Reviews Cardiology, vol. 16, no. 7. Nature Publishing Group, pp. 389–406, 01-Jul-2019.

[2]   T. Takumi et al., "Limitation of Angiography to Identify the Culprit Plaque in Acute Myocardial Infarction With Coronary Total Occlusion. Utility of Coronary Plaque Temperature Measurement to Identify the Culprit Plaque," J. Am. Coll. Cardiol., vol. 50, no. 23, pp. 2197–2203, Dec. 2007.

[3] K. K. L. Wong, P. Thavornpattanapong, S. C. P. Cheung, Z. Sun, and J. Tu, "Effect of calcification on the mechanical stability of plaque based on a three-dimensional carotid bifurcation model," BMC Cardiovasc. Disord., vol. 12, no. 1, pp. 1–18, Feb. 2012.

[4] D. R. J. Owen, A. C. Lindsay, R. P. Choudhury, and Z. A. Fayad, "Imaging of Atherosclerosis," Annu. Rev. Med., vol. 62, no. 1, pp. 25–40, Feb. 2011.

[5] J. M. Tarkin et al., "Imaging Atherosclerosis," Circ. Res., vol. 118, no. 4, pp. 750–769, Feb. 2016.

[6] J. M. Tarkin, F. R. Joshi, and J. H. F. Rudd, "PET imaging of inflammation in atherosclerosis," Nat. Rev. Cardiol., vol. 11, no. 8, pp. 443–457, Aug. 2014.

[7] A. L. Figueroa et al., "Measurement of Arterial Activity on Routine FDG PET/CT Images Improves Prediction of Risk of Future CV Events," JACC Cardiovasc. Imaging, vol. 6, no. 12, pp. 1250–1259, Dec. 2013.

[8] T. C. Kwee, G. Cheng, M. G. E. H. Lam, S. Basu, and A. Alavi, "SUVmax of 2.5 should not be embraced as a magic threshold for separating benign from malignant lesions," European Journal of Nuclear Medicine and Molecular Imaging, vol. 40, no. 10. pp. 1475–1477, Oct-2013.

[9] J. H. F. Rudd et al., "18Fluorodeoxyglucose Positron Emission Tomography Imaging of Atherosclerotic Plaque Inflammation Is Highly Reproducible. Implications for Atherosclerosis Therapy Trials," J. Am. Coll. Cardiol., vol. 50, no. 9, pp. 892–896, Aug. 2007.

[10] A. A. Lammertsma, "Forward to the Past: The Case for Quantitative PET Imaging," J. Nucl. Med., vol. 58, no. 7, pp. 1019–1024, Jul. 2017.

[11] V. Caselles, R. Kimmel, and G. Sapiro, "Geodesic Active Contours," Int. J. Comput. Vis., vol. 22, no. 1, pp. 61–79, 1997.

[12] A. J. Einstein et al., "Agreement of visual estimation of coronary artery calcium from low-dose CT attenuation correction scans in hybrid PET/CT and SPECT/CT with standard agatston score," J. Am. Coll. Cardiol., vol. 56, no. 23, pp. 1914–1921, Nov. 2010.

[13] N. van der Bijl et al., "Assessment of Agatston Coronary Artery Calcium Score Using Contrast-Enhanced CT Coronary Angiography," Am. J. Roentgenol., vol. 195, no. 6, pp. 1299–1305, Dec. 2010.

[14] A. S. Agatston, W. R. Janowitz, F. J. Hildner, N. R. Zusmer, M. Viamonte, and R. Detrano, "Quantification of coronary artery calcium using ultrafast computed tomography," J. Am. Coll. Cardiol., vol. 15, no. 4, pp. 827–832, Mar. 1990.

[15] M. E. Phelps, S. C. Huang, E. J. Hoffman, C. Selin, L. Sokoloff, and D. E. Kuhl, "Tomographic measurement of local cerebral glucose metabolic rate in humans with (F-18)2-fluoro-2-deoxy-D-glucose: Validation of method," Ann. Neurol., vol. 6, no. 5, pp. 371–388, 1979.

[16] M. Bentourkia, D. Lapointe, V. Selivanov, I. Buvat, and R. Leconte, "Determination of blood curve and tissue uptake from left ventricle using FADS in rat FDG-PET studies," IEEE Nucl. Sci. Symp. Conf. Rec., vol. 2, pp. 1124–1127, Jan. 1999.

[17] H. M. Wu et al., "Factor analysis for extraction of blood time-activity curves in dynamic FDG-PET studies.," J. Nucl. Med., vol. 36, no. 9, pp. 1714–22, Sep. 1995.

[18] M. Bentourkia, "Kinetic modeling of PET data without blood sampling," IEEE Trans. Nucl. Sci., vol. 52, no. 3 I, 2005.

[19] K. Arai and A. R. Barakbah, "Hierarchical K-means: an algorithm for centroids initialization for K-means." 2007.

[20] P. J. Rousseeuw, "Silhouettes: A graphical aid to the interpretation and validation of cluster analysis," J. Comput. Appl. Math., vol. 20, no. C, pp. 53–65, 1987.

[21] X. Wang, B. Jiang, and J. S. Liu, "Generalized R-squared for detecting dependence," Biometrika, vol. 104, no. 1, pp. 129–139, 2017.

[22] X. Li et al., "Association between osteogenesis and inflammation during the progression of calcified plaque evaluated by 18F-Fluoride and 18F-FDG," J. Nucl. Med., vol. 58, no. 6, pp. 968–974, Jun. 2017.

[23] N. V. Joshi et al., "18F-fluoride positron emission tomography for identification of ruptured and high-risk coronary atherosclerotic plaques: A prospective clinical trial," Lancet, vol. 383, no. 9918, pp. 705–713, Feb. 2014.

[24] T. Derlin et al., "Imaging of chemokine receptor CXCR4 expression in culprit and nonculprit coronary atherosclerotic plaque using motion-corrected [68Ga]pentixafor PET/CT," Eur. J. Nucl. Med. Mol. Imaging, vol. 45, no. 11, pp. 1934–1944, Oct. 2018.

[25] F. A. Kotasidis, C. Tsoumpas, and A. Rahmim, "Advanced kinetic modelling strategies: towards adoption in clinical PET imaging," Clin. Transl. Imaging, vol. 2, no. 3, pp. 219–237, Jun. 2014.

[26] L. G. Strauss, A. Dimitrakopoulou-Strauss, and U. Haberkorn, "Shortened PET data acquisition protocol for the quantification of 18F-FDG kinetics," J. Nucl. Med., vol. 44, no. 12, pp. 1933–1939, Dec. 2003.

[27] T. Torizuka et al., "Short dynamic FDG-PET imaging protocol for patients with lung cancer," Eur. J. Nucl. Med., vol. 27, no. 10, pp. 1538–1542, 2000.

[28] M. Soret, S. L. Bacharach, and I. Buvat, "Partial-volume effect in PET tumor imaging," Journal of Nuclear Medicine, vol. 48, no. 6. pp. 932–945, Jun-2007.

[29] N. J. Hoetjes et al., "Partial volume correction strategies for quantitative FDG PET in oncology," Eur. J. Nucl. Med. Mol. Imaging, vol. 37, no. 9, pp. 1679–1687, Aug. 2010.

[30] L. Arhjoul, O. Sarrhini, and M. Bentourkia, "Partial volume correction using continuous wavelet technique in small animal PET imaging," in IEEE Nuclear Science Symposium Conference Record, 2006, vol. 5, pp. 2717–2721.

[31] E. Croteau et al., "Image-derived input function in dynamic human PET/CT: Methodology and validation with 11C-acetate and 18F- fluorothioheptadecanoic acid in muscle and 18F-fluorodeoxyglucose in brain," Eur. J. Nucl. Med. Mol. Imaging, vol. 37, no. 8, pp. 1539–1550, May 2010.

[32] M. Bentourkia, "Determination of the Input Function at the Entry of the Tissue of Interest and Its Impact on PET Kinetic Modeling Parameters," Molecular Imaging and Biology, vol. 17, no. 6. Springer New York LLC, pp. 748–756, 01-Dec-2015.

[33] G. Galli, L. Indovina, M. L. Calcagni, L. Mansi, and A. Giordano, "The quantification with FDG as seen by a physician," Nucl. Med. Biol., vol. 40, no. 6, pp. 720–730, Aug. 2013.

[34] M. H. Criqui et al., "Calcium density of coronary artery plaque and risk of incident cardiovascular events," JAMA - J. Am. Med. Assoc., vol. 311, no. 3, pp. 271–278, 2014

7. ARTICLE 3

Assessment of inflammation in non-calcified artery plaques with dynamic ¹⁸F-FDG-PET/CT: CT alone, does it detect the vulnerable plaque?

Mamdouh S. Al-enezi, Abdelouahed Khalil, Tamas Fulop, Éric Turcotte, M'hamed Bentourkia

Contribution of the student: Mamdouh S. Al-Enezi has performed the analysis for this project and the preparation of the first draft.

Résumé:

Objectif: l'objectif de cette étude était la localisation de la plaque athéromateuse vulnérable en l'absence de calcification au moyen de sa densité en unités de Hounsfield (HU) sur l'imagerie par tomodensitométrie (CT), et au moyen de son métabolisme sur la tomographie d'émission par positons (TEP). Les plaques artérielles non calcifiées (NCP) et calcifiées (CP) des images TDM étaient corrélées avec le taux métabolique du 2-désoxy-2 [¹⁸F] fluoro-D-glucose (¹⁸F-FDG) (MRG) et la valeur d'absorption standard maximale (SUVmax) dans les images TEP.

Procédures: 19 volontaires âgés de 65 à 85 ans ont subi une imagerie dynamique TDM/¹⁸F-FDG-TEP, parmi lesquels 9 étaient sous médication. Une artère normale (NAR) a été définie comme n'ayant pas de plaque sur une coupe d'image transaxiale TDM (segment), ou bien elle peut contenir du tissu fibreux, le tout avec une densité comprise entre 51 et 130 HU. La CP a été identifiée comme ayant une densité supérieure à 130 HU d'après la littérature. En outre, et toujours sur la base de la littérature, la NCP dans la région de la circonférence d'un segment d'artère a été définie comme une plaque contenant 4 pixels adjacents ou plus ayant une intensité ≤ 50 HU identifiée par la méthode de seuillage d'histogramme. En CP, le rapport de la zone de calcification à la surface de l'artère (RCA) et le score de calcification d'Agatston (ACS) ont été classifiés à l'aide de l'algorithme K-means en 4 groupes du plus petit au plus grand: RCA1, RCA2, RCA3 et RCA4 pour la l'aire, et

ACS1 ACS2, ACS3 et ACS4 pour les scores de densité, et ils ont été corrélés avec MRG et SUVmax.

Résultats: MRG et SUVmax ont été trouvés statistiquement plus élevés pour le NCP comparés aux paramètres NAR et le CP chez les sujets ne prenant pas de médicaments ($p < 0,05$), tandis que ces valeurs du NCP ont profondément chuté chez les sujets sous traitement et NCP est resté statistiquement différent de NAR mais pas de CP. Dans le groupe sans médicament, MRG dans NCP n'était pas statistiquement significativement différent dans les plaques d'aires étendues ($p = 0,40$ et $p = 0,55$ entre NCP et RCA3, et NCP et RCA4, respectivement). Dans le groupe sous-médicament, aucune différence statistique n'a été trouvée entre NCP et les quatre RCA, ils ont tous été abaissés par le médicament.

Conclusions: Étant donné que la plaque calcifiée à haute densité a été rapportée comme stable, et que la plaque de faible densité a été reconnue comme la plaque vulnérable, sur la base de ce travail, cette dernière peut être identifiée sur les images de TDM seule. La plaque ayant une densité inférieure à 50 HU exprimait un métabolisme élevé sur la TEP-^{18}F-FDG indiquant son inflammation, et elle avait une sensibilité significative aux médicaments.

Mots-clés : Athérosclérose, inflammation des artères, plaque non calcifiée, calcification, modélisation cinétique, TDM, TEP.

Assessment of inflammation in non-calcified artery plaques with dynamic ^{18}F-FDG-PET/CT: CT alone, does it detect the vulnerable plaque?

Mamdouh S. Al-enezi, Abdelouahed Khalil, Tamas Fulop, Éric Turcotte, M'hamed Bentourkia

Abstract

Purpose: The goal in this study was the localization of the vulnerable atheromatous artery plaque in the absence of calcification by means of its density in Hounsfield units (HU) on computed tomography (CT) imaging and by means of its metabolism on positron emission tomography (PET) imaging. The non-calcified (NCP) and calcified (CP) artery plaques in CT images were correlated with the metabolic rate of 2-deoxy-2[^{18}F] fluoro-D-glucose (^{18}F-FDG) (MRG) and maximal standard uptake value (SUVmax) in PET images.

Procedures: 19 volunteers aged 65 to 85 years underwent a dynamic ^{18}F-FDG-PET/CT imaging, among them 9 were under medication. A normal artery (NAR) was defined as having no plaque on a CT transaxial image slice (segment), or it might contain fibrous tissue, all with density between 51 and 130 HU. CP was identified as having density above 130 HU as based on the literature. Also, based on the literature, NCP in the circumference region of an artery segment was defined as a plaque containing 4 adjacent pixels or more having ≤ 50 HU identified by histogram thresholding method. In CP, the ratio of calcification area to artery area (RCA) and Agatston calcification score (ACS) were clustered using Hierarchical K-means algorithm into 4 clusters from small to large: RCA1, RCA2, RCA3 and RCA4 for area, and ACS1, ACS2, ACS3 and ACS4 for density scores, and were correlated with MRG and SUVmax.

Results: MRG and SUVmax were found statistically higher for NCP compared to both NAR and CP in non-medication subjects ($p<0.05$), while these values in NCP deeply dropped in subjects with medication and NCP remained statistically different from NAR but not from CP. In non-medication group, MRG in NCP was not statistically significantly different in larger plaque area ($p= 0.40$ and $p= 0.55$ between NCP and RCA3, and NCP and RCA4, respectively). In under-medication group, no statistical differences were found between NCP and the four RCAs, they were all lowered by the medication.

Conclusions: Since the high-density calcified plaque was reported as stable, and the low-density plaque was recognized as the vulnerable plaque, based on the present work, this latter can be uniquely identified on CT images. The plaque having density below 50 HU expressed a high metabolism on PET indicating its inflammation, and it had a significant susceptibility to medication.

Keywords: Atherosclerosis, Artery inflammation, Non-calcified plaque, Calcification, Kinetic modeling, Computed Tomography, Positron emission tomography.

Introduction

Atherosclerosis is the most common type of cardiovascular disease (CVD) causing mortality and morbidity specially in seniors [1]. It begins with the formation of atherosclerotic plaque caused by, but not limited to, the lipid accumulation and oxidation [2]. It has been demonstrated that the degree of stenosis alone is not the best predictor of CVD complication risk, such as stroke and heart attack.

Computed tomography (CT) provides quantification of calcified plaques (CP) and non-calcified plaques (NCP) by means of diverse techniques [3–5]. Besides, NCP was the most prone to rupture plaque as reported in several works [6–8]. This has led to the concept of the "*vulnerable plaque*" describing atherosclerotic plaques with high risk of rupture. Intravascular ultrasound (IVUS) and optical coherence tomography are invasive imaging modalities having been widely used due to a good accuracy and resolution enabling them to identify NCP, in addition to the measurement of fibrous cap thickness [9]. However, the penetration depth, invasive nature and shadowing artifacts added difficulties to assess plaque morphology at the site of the culprit lesion [10]. Magnetic resonance imaging (MRI) is a promising modality for atherosclerosis. Several studies have validated the ability of MRI to differentiate fibrous cap and lipid core components of the atherosclerotic plaque [11–13], nevertheless, a need of longer imaging times to enhance signal to noise ratio and MRI environment not suitable for patients with claustrophobia, pacemakers, defibrillators, and certain aneurysm clips are of major limitations [14].

Recently, several studies in the use of CT images have went deep beyond the stenosis and calcification toward NCP identification. NCP was mostly reported as below 30 HU or below 50 HU cut-off values [15–20]. CT images afford many privileges over other modalities including low cost, less sensitive to motion and non-invasive with very short acquisition time. In the combination with CT, positron emission tomography (PET) imaging is noninvasively able to assess high-risk features of unstable plaque with superior sensitivity up to picomolar tracer concentration detection over other non-invasive imaging modalities[21]. ^{18}F-FDG is the most validated and used tracer for PET imaging and has been extensively demonstrated as a monitor and early atherosclerosis predictor, marker for inflammatory and vulnerable plaques[22–24]. ^{18}F-FDG uptake has been reported to accurately predict the NCP and plaque within the fibrous cap [25]. Although the metabolic rate of glucose (MRG) quantitatively estimated from the standard two-tissue compartment model of ^{18}F-FDG [26] is not often used in clinical practice, it is more reliable than semi-quantitative parameters [27–29] and provides precise and comprehensive description of tissue metabolism [30].

It has been reported that plaque lipid rich tissue and fibrous tissue can be discriminated based on their intensities on CT images [3, 5, 31], and that the lipid rich plaques are the most vulnerable for detachment [3]. Other investigations showed that heterogeneous NCP are associated with high risk detachment [17, 32], while homogeneous NCP are stable [17]. The density of the lipid rich plaque was found between 30 and 60 HU [16, 33], distinctive from plaque fibrous tissue and normal artery tissue which have higher density. Backed by these findings, in this study, we segmented arteries for NCP on CT images with a cut-off value of 50 HU and assessed their metabolism, as a function of MRG and SUVmax in aged volunteers. We also report MRG and SUVmax of CP in comparison to calcification area and density.

Methods

Study design and population

We prospectively recruited nineteen subjects in this study (age range 65 to 85 years). Among these subjects, 9 were taking their prescribed medication against artery

inflammation. All participants underwent overnight fasting prior of glycemia measurements. Low-dose CT images were first acquired for photon attenuation correction, anatomic correlation and for plaque quantification. Dynamic PET data acquisition was performed for 30 min after a bolus intravenous injection of ^{18}F-FDG (3.7 to 10 mCi adjusted by subject's weight) and binned into 26 frames: 12×10 secs, 8×30 secs and 6×240 secs. This acquisition time of 30 min was reported to be greatly correlated to a standard PET acquisition time of 60 min [34]. PET and CT acquisitions were performed with a PET/CT system (Philips Gemini TF 16) in a matrix of a $144 \times 144 \times 45$ for PET and in a matrix $512 \times 512 \times 138$ for CT, and the PET images were reconstructed using the iterative 3D row action maximum likelihood reconstruction algorithm. The ^{18}F-FDG uptake and calcification on PET/CT images were assessed in the aorta and iliac arteries on the transaxial images.

Analysis of CT images

Arteries were segmented from CT transaxial images using edge-based active contour model semi-automatically to find an optimal object boundary [35]. The method of histogram thresholding was used for intensities ≤ 50 HU for NCP determination and > 130 HU for CP in areas of at least 4 adjacent pixels in the circumference region of the arterial segment (artery transaxial image slice) [36, 37], and as a second condition, there cannot be another cluster of 4 adjacent pixels in the same artery segment. An artery with no plaque observed on the artery segment or with intensities between 51 and 130 HU was considered as a normal artery (NAR), (i.e. not prone to rupture). The calcification area was computed and normalized to artery area to give the calcification area ratio (RCA) [36], whereas Agatston calcification scores (ACS) were calculated using a value assigned to the maximum density of calcification in a given artery segment as explained below. We also considered the maximal density in HU in each calcification area and classified these densities in four levels similar to ACS as density levels (DL) from 1 to 4.

The Hierarchical K-means algorithm (AHK) with the precision of hierarchical clustering [38] in the combination with silhouette-coefficient [39] were used for calcification area and scores clustering. With AHK, RCA of artery segments were clustered in 4 clusters: RCA1-4. For ACS calculation, the maximum pixel density in each calcification area was assigned a level from 1 to 4 depending on its density: value of 1 for 131–199 HU, 2 for 200–299 HU,

3 for 300–399 HU, and 4 for 400 HU and above. The ACS were obtained by multiplying these levels with their corresponding RCA [40–42]. The ACSs of all the artery segments were segmented with AHK in 4 clusters: ACS1-4. At the end, the clusters of RCA1 to 4, ACS1 to 4, DL1 to 4, NCP and NAR formed the independent variables for PET MRG and SUVmax comparison.

Analysis of PET images

Artery images were segmented from early frames of PET dynamic images using active contour. The arterial input function (IF) was derived from the blood component decomposed using factor analysis of dynamic sequence (FA) [43–46]. Artery time-activity curves (TAC) defined from transaxial PET dynamic image slices were fitted with the modified two-tissue compartment model [43]. In this model, the tissue blood volume function was taken as the FA blood component (BC) (commonly assumed as a fraction of IF), and IF was taken as a factor of FA blood component, i.e. $IF = \nu BC$ with $\nu > 1$. This model without blood sampling (WOBS) is efficient as it does not require an IF determination neither it needs the correction for partial volume effect (PVE) since the IF and the tissue TAC are deduced from the same region of interest (ROI).

Statistical analysis

Continuous data were tested for normality using the D'Agostino-Pearson omnibus test. Continuous parametric variables were expressed as mean ± STD and compared using Student's *t* tests and expressed as mean ± STD. Non-parametric data were compared using Mann-Whitney *U* test and expressed as median, quartiles and interquartile range (IQR) with the statistical significance level chosen as 5%.

Results

An example of the bifurcation of the iliacs is shown in Figure 7.1A. In other subjects, the aorta was also apparent on the image. Figure 7.1B shows an example of a TAC fit with WOBS. In Figure 7.2A, the NCP was determined in the artery circumference region and identified on the corresponding whole-artery PET image slice (Figure 7.2B). An example of

calcification area reported to artery area for RCA calculation is shown in Figure 7.2C and 2D.

The number of artery calcification segments on CT transaxial images in all 19 subjects were 354 out of 710 in total, with a mean RCA of 0.21 ± 0.14 (Median, 0.18; IQR, 0.20; IQR range, 0.10 - 0.30), and ACS of 0.74 ± 0.59 (mean $\pm$ STD) (Median, 0.61; IQR, 0.92; IQR range, 0.21 - 1.14). Not all these CT artery segments were used in the analysis, but only those corresponding to the artery image slices on PET as reported in the figures below.

Table 7.1 presents the statistics of MRG in units of μmoles/100g/min and SUVmax for the three types of arteries and for non-medication and subjects under medication, and Figure 7.3 depicts the MRG values of their respective medians. From Figure 7.3, all the three types of arteries were statistically significantly different respectively between non-medication and under-medication, and between each other, except NCP and CP which were not different in under-medication. NCP was found to have the highest MRG value, and the medication was observed to act more on this type of artery, suggesting that this type of artery segment encompasses the inflamed plaque which is prone to rupture.
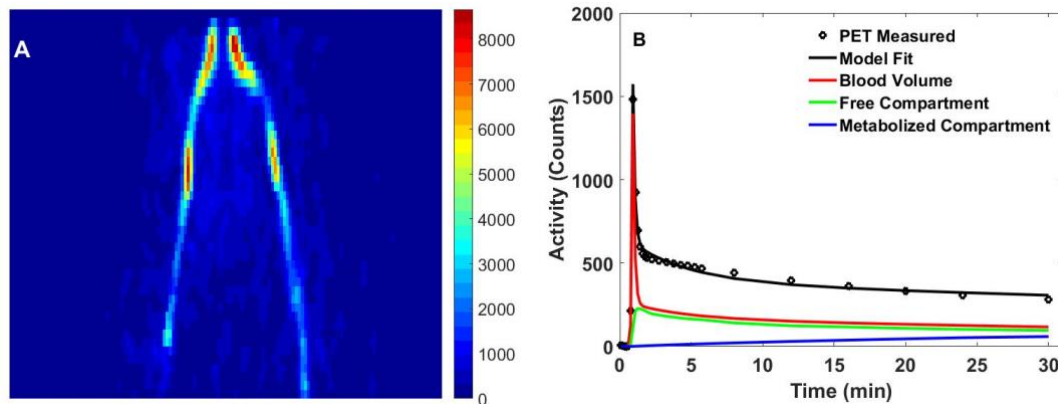
Figure 7.1 A) The coronal view of a PET blood FA image where the right and left iliacs were distinguished. B) Example of an artery TAC fit with WOBS model.
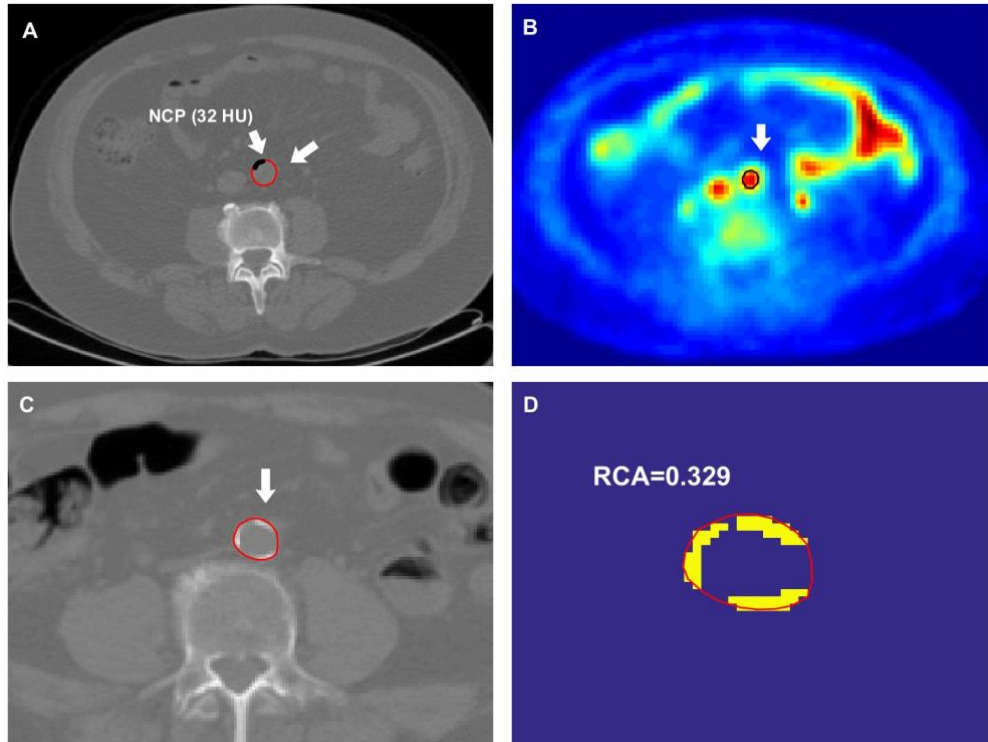
Figure 7.2 A) CT image of aorta showing the NCP region with mean HU of 32 and an area of 89.3 mm³, B) Corresponding aorta PET image. C) CT image of aorta with calcified arterial wall. D) Binary image of the calcified plaque with an RCA of 0.329.

Table 7.1 MRG values in units of μmoles/100g/min and SUVmax for NAR, NCP and CP, from subjects with non-medication and subjects under medication.

Cluster	Measures	Without medication		With medication	
		MRG	SUVmax	MRG	SUVmax
NAR	Mean±STD	1.50±0.91	1.94±0.40	1.22±0.77	1.80±0.36
	Median	1.32	1.97	1.10	1.84
	Quartiles	0.74–2.08	1.74–2.17	0.61–1.70	1.57–2.02
	IQR	1.34	0.43	1.09	0.46
NCP	Mean±STD	170±0.83	2.42±0.50	0.74±0.45	2.26±0.45
	Median	1.52	2.46	0.70	2.30
	Quartiles	1.10–2.32	2.18–2.72	0.35–1.05	1.96–2.53
	IQR	1.22	0.54	0.70	0.57
CP	Mean±STD	1.20±0.88	1.91±0.55	0.82±0.47	1.70±0.53
	Median	0.99	1.90	0.75	1.70
	Quartiles	0.45–1.74	1.59–2.27	0.40–1.16	1.31–2.05
	IQR	1.29	0.68	0.75	0.74
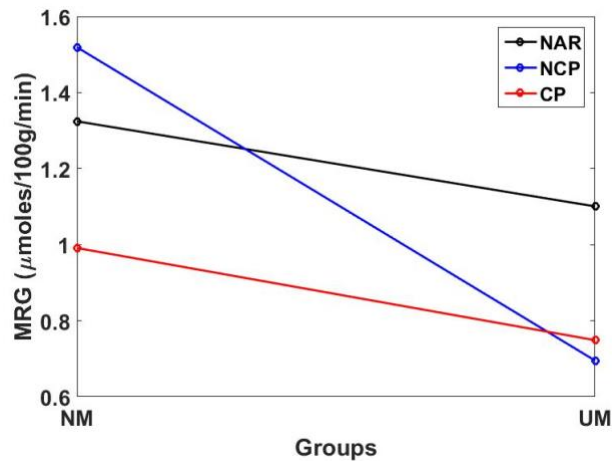
Figure 7.3 Median MRG for NAR, NCP and CP artery types for non-medicated (NM) and under-medication (UM) groups. All the three types of arteries were statistically significantly different between non-medication and under-medication, and between each other, except NCP and CP which were not different in under-medication.

The values of MRG from the four area clusters RCA1-4, from the four density levels DL1-4, and from the four scores ACS1-4 are reported in Figure 7.4 in comparison to NCP and NAR, and for subjects without and with medication. NCP in non-medication data was found statistically significantly different from RCA1 and RCA2 but not from RCA3 and RCA4 (Figure 7.4A). However, the medication lowered all the values including NCP, and then NCP was not statistically different from RCAs (Figure 7.4B). NCP in non-medication was found statistically significantly different from NCP in subjects under medication. When comparing NCP to NAR, they were found statistically significantly different in non-medication ($p = 0.032$) and in under-medication ($p = 3.48.10^{-5}$). From Figure 7.4A, NCP has higher MRG than NAR (Mean: 1.70 versus 1.50, Median 1.52 versus 1.32, see Table 7.1) reflecting the inflammation in the NCP plaque, and this observation is confirmed by the action of the medication in Figure 7.4B where MRG of NCP was highly reduced with respect to that of NAR which is assumed to contain normal artery wall (Mean: 0.74 versus 1.22, Median 0.70 versus 1.10, see Table 7.1). Meanwhile, NCP was found different from DL2 and DL4 in non-medicated subjects (Figure 7.4C). Apparently, these differences were due to the far outliers, and when the outliers were removed, NCP was found statistically different from only DL1. Without removing the outliers in DLs from subjects under medication, no statistical differences were found between NCP and DL1 to 4 (Figure 7.4D). With respect to ACS, in subjects with non-medication, NCP was found statistically significantly different from ACS1 and ACS2 but not from ACS3 and ACS4 (Figure 7.4E), while NCP was not different from all ACSs in subjects under medication (Figure 7.4F).
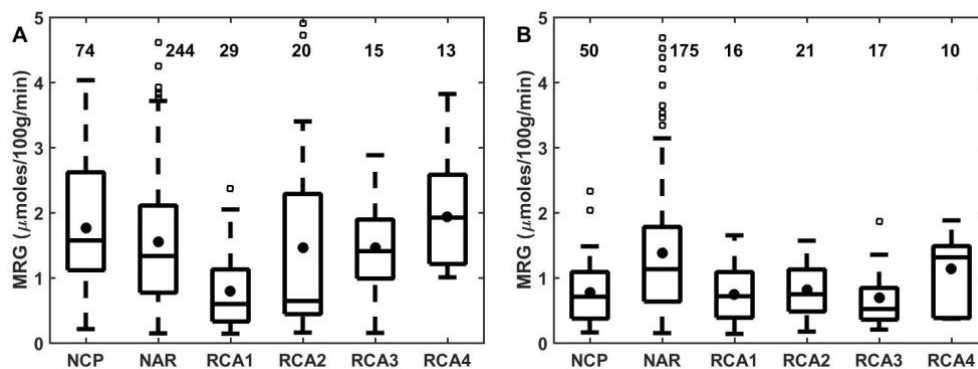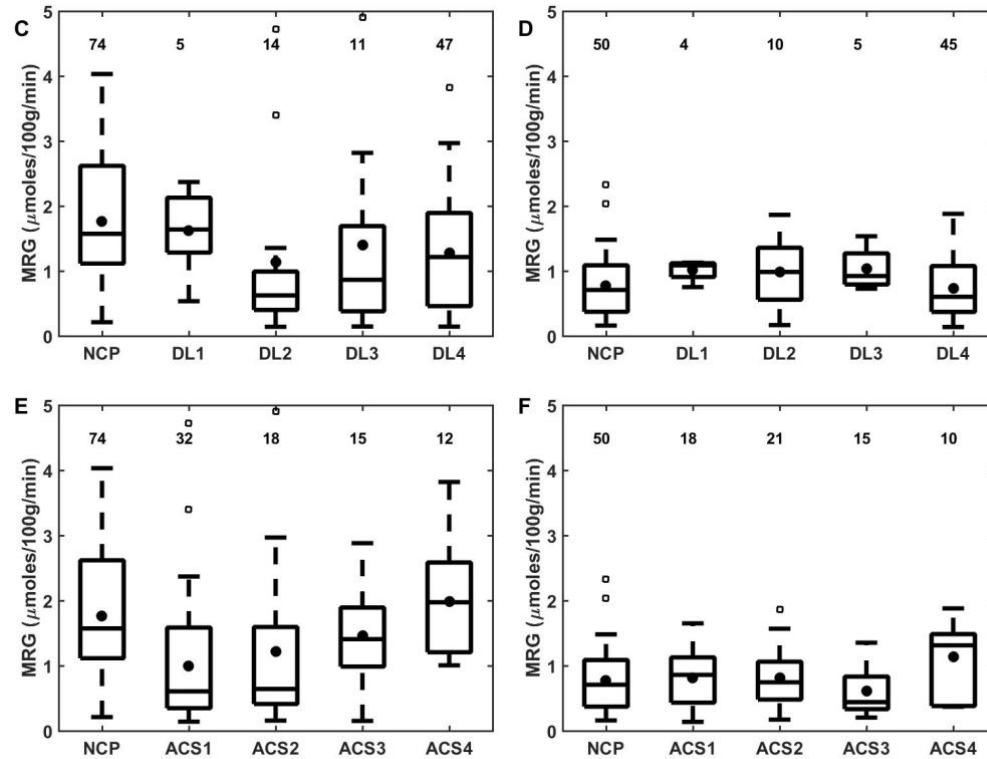
Figure 7.4 Comparison of metabolic activity (MRG) for (A) NCP, NAR and RCA clusters in non-medicated subjects, (B), Same as (A) for subjects under medication. C) and D) Same as (A) and (B), respectively, but for the four density levels (LD) (NAR was omitted since it was the same as in (A) and (B)). E) and F) same as in C) and D) for NCP in comparison to ACSs. The empty squares are for outliers and the filled circles are for the means. The numbers above each box plot indicate the number of artery segments. MRG of NCP was found statistically significantly different from those of NAR, RCA1 and RCA2 in (A), from NAR only in (B), from DL2 and DL4 in (C), and from ACS1 and ACS2 in (E).

Discussion

CT is abundantly used in atherosclerosis imaging for visualizing and quantifying the calcification as a marker for atherosclerotic plaques burden especially when the calcification is linked to its extent. Meanwhile, it was discovered that the high calcification was associated with the plaque stability, and the co-occurrence of calcified and non-calcified plaques were associated with plaque vulnerability. This latter finding was further confirmed by imaging with PET and ^{18}F-NaF [7, 47]. It was reported that plaque rupture is not necessarily dependent on plaque volume or extent of its stenosis, but the microcalcifications and inflammation rather play a more crucial role [47]. Therefore, this study is in agreement with

the literature emphasizing the dynamic imaging with PET-^{18}F-FDG and exploiting the low dose CT imaging.

NCP with a cut-off value of $\leq$ 50 HU was found to be metabolically more sensitive compared to density $\leq$ 30 HU cut-off in the agreement with other findings [3, 5, 7]. The metabolism in NCP was also significantly higher compared to CP group and even when assessed with SUVmax as illustrated in Table 7.1 and Figure 7.3. Compared to the normal artery wall assumed to have CT densities between 51 and 130 HU (NAR), NCP was found having a high MRG value relative to NAR in non-medication (Table 7.1, Figure 7.3 and Figure 7.4A), denoting its inflammation, and this observation was confirmed in subjects under medication were the medication drastically lowered the metabolism, i.e. treated inflammation, in NCP more than in NAR (Table 7.1, Figure 7.3 and Figure 7.4B). The effect of the medication on NAR was also found statistically significantly different between non-medication and under-medication subjects (p = 0.023).

This study demonstrated a significant variation of NCP with respect to the plaque area but not to the density of calcification. Remarkably, the area but not density was cited to be obviously associated with atherosclerosis risk [48]. Unsurprisingly, the calcification scores in Agatston approach were in the same arrangement as the areas where the scores were influenced more by area (same statistical differences between NCP and RCAs versus NCP and ACSs). The effect of medication was clearly demonstrated in NCP and RCA clusters as shown in Figure 7.3 and 7.4 in accordance with the literature [49].

The limited number of subjects, 10 without medication and 9 under medication, generated acceptable number of artery segments based on their area with a minimum of 23 segments per class and a maximum of 39, but based on their density, some segments had a limited number such as 4 in density levels. However, the main conclusions are more drawn from NCP versus NAR and CP globally which have more than 50 samples. As discussed above, the plaque density has a lesser impact on the inflammation, the thresholding of NCP to below 50 HU as reported in the literature depends on the statistics in the CT images which are influenced by several parameters such as beam flux and photon energy spectrum, photon scattering, image reconstruction filtering, artery movement and artery image segmentation. Keeping a gap between 50 HU and 130 HU, where this latter is the start of the calcification,

assures somehow the assumption of the homogeneity of the vulnerable plaque. Another remark concerns the kinetic modeling when using WOBS, which makes the ^{18}F-FDG uptake depending on the same ROI for the input function and for tissue time-activity curve, thus intrinsically reducing the uncertainties, and at the same time, the model avoids the partial volume effect. In other circumstances, the input function has to be determined by other means, e.g. by blood sampling or from artery images, to fit the artery TAC, where this artery TAC itself is mainly made of activity in blood.

Conclusion

This prospective study confirmed the possibility of CT images to identify the non-calcified artery plaque (NCP) with density below 50 HU with an excellent correlation with its metabolic activity. NCP and high calcification area were accompanied with a statistically high metabolic activity. Medication against artery inflammation was clearly shown to reduce NCP metabolism. Based on the literature reporting the potential of ^{18}F-NaF to detect the vulnerable plaque, and since ^{18}F-NaF reports the plaque before being calcified, NCP is expected to play the same role with the more available CT imaging alone than the addition of PET imaging.

Major findings of the research:

The main objective was to study the capability of CT imaging in identifying the vulnerable plaque. We demonstrated that non-calcified plaque with a density below 50 HU has a situ correlation with higher metabolic activity and thus it was assumed as instable plaque.

Conflict of interest

None of the authors have any conflicts of interest to disclose.

References

1. Agnelli G, Belch JJF, Baumgartner I, et al (2020) Morbidity and mortality associated with atherosclerotic peripheral artery disease: A systematic review. Atherosclerosis. https://doi.org/10.1016/j.atherosclerosis.2019.09.012

2. Rafieian-Kopaei M, Setorki M, Doudi M, et al (2014) Atherosclerosis: process, indicators, risk factors and new hopes. Int J Prev Med 5:927–46

3. Saremi F, Achenbach S (2015) Coronary plaque characterization using CT. Am. J. Roentgenol.

4. Owen DRJ, Lindsay AC, Choudhury RP, Fayad ZA (2011) Imaging of Atherosclerosis. Annu Rev Med 62:25–40. https://doi.org/10.1146/annurev-med-041709-133809

5. Achenbach S, Raggi P (2010) Imaging of coronary atherosclerosis by computed tomography. Eur. Heart J.

6. Li X, Heber D, Gonzalez JC, et al (2017) Association between osteogenesis and inflammation during the progression of calcified plaque evaluated by 18F-Fluoride and 18F-FDG. J Nucl Med 58:968–974. https://doi.org/10.2967/jnumed.116.182790

7. Kitagawa T, Yamamoto H, Toshimitsu S, et al (2017) 18F-sodium fluoride positron emission tomography for molecular imaging of coronary atherosclerosis based on computed tomography analysis. Atherosclerosis. https://doi.org/10.1016/j.atherosclerosis.2017.04.024

8. Blomberg BA, de Jong PA, Thomassen A, et al (2017) Thoracic aorta calcification but not inflammation is associated with increased cardiovascular disease risk: results of the CAMONA study. Eur J Nucl Med Mol Imaging. https://doi.org/10.1007/s00259-016-3552-9

9. Miyamoto Y, Okura H, Kume T, et al (2011) Plaque characteristics of thin-cap fibroatheroma evaluated by OCT and IVUS. JACC Cardiovasc Imaging 4:638–646. https://doi.org/10.1016/j.jcmg.2011.03.014

10. Ehara S, Kobayashi Y, Yoshiyama M, et al (2004) Spotty calcification typifies the culprit plaque in patients with acute myocardial infarction: An intravascular ultrasound study. Circulation 110:3424–3429. https://doi.org/10.1161/01.CIR.0000148131.41425.E9

11. Chai JT, Biasiolli L, Li L, et al (2017) Quantification of Lipid-Rich Core in Carotid Atherosclerosis Using Magnetic Resonance T2 Mapping: Relation to Clinical Presentation. JACC Cardiovasc Imaging 10:747–756. https://doi.org/10.1016/j.jcmg.2016.06.013

12. Trivedi RA, U-King-Im JM, Graves MJ, et al (2004) MRI-derived measurements of fibrous-cap and lipid-core thickness: The potential for identifying vulnerable carotid plaques in vivo. Neuroradiology 46:738–743. https://doi.org/10.1007/s00234-004-1247-6

13. Corti R, Fuster V (2011) Imaging of atherosclerosis: Magnetic resonance imaging. Eur Heart J. https://doi.org/10.1093/eurheartj/ehr068

14. Anderson JD, Kramer CM (2007) MRI of atherosclerosis: Diagnosis and monitoring therapy. Expert Rev. Cardiovasc. Ther. 5:69–80

15. Motoyama S, Kondo T, Sarai M, et al (2007) Multislice Computed Tomographic Characteristics of Coronary Lesions in Acute Coronary Syndromes. J Am Coll Cardiol 50:319–326. https://doi.org/10.1016/j.jacc.2007.03.044

16. Marwan M, Taher MA, El Meniawy K, et al (2011) In vivo CT detection of lipid-rich coronary artery atherosclerotic plaques using quantitative histogram analysis: A head to head comparison with IVUS. Atherosclerosis 215:110–115. https://doi.org/10.1016/j.atherosclerosis.2010.12.006

17. Maurovich-Horvat P, Schlett CL, Alkadhi H, et al (2012) The napkin-ring sign indicates advanced atherosclerotic lesions in coronary CT angiography. JACC Cardiovasc Imaging 5:1243–1252. https://doi.org/10.1016/j.jcmg.2012.03.019

18. Achenbach S (2008) Can CT detect the vulnerable coronary plaque? Int. J. Cardiovasc. Imaging 24:311–312

19. Dalager MG, Bøttcher M, Andersen G, et al (2011) Impact of luminal density on plaque classification by CT coronary angiography. Int J Cardiovasc Imaging 27:593–600. https://doi.org/10.1007/s10554-010-9695-z

20. Tzolos E, McElhinney P, Williams MC, et al (2020) Repeatability of quantitative pericoronary adipose tissue attenuation and coronary plaque burden from coronary CT angiography. J Cardiovasc Comput Tomogr. https://doi.org/10.1016/j.jcct.2020.03.007

21. Tarkin JM, Joshi FR, Rudd JHF (2014) PET imaging of inflammation in atherosclerosis. Nat Rev Cardiol 11:443–457. https://doi.org/10.1038/nrcardio.2014.80

22. Tarkin JM, Joshi FR, Evans NR, et al (2017) Detection of Atherosclerotic Inflammation by 68Ga-DOTATATE PET Compared to [18F]FDG PET Imaging. J Am Coll Cardiol. https://doi.org/10.1016/j.jacc.2017.01.060

23. Moghbel M, Al-Zaghal A, Werner TJ, et al (2018) The Role of PET in Evaluating Atherosclerosis: A Critical Review. Semin. Nucl. Med.

24. Leccisotti L, Nicoletti P, Cappiello C, et al (2019) PET imaging of vulnerable coronary artery plaques. Clin. Transl. Imaging

25. Saito H, Kuroda S, Hirata K, et al (2013) Validity of dual MRI and F-FDG PET imaging in predicting vulnerable and inflamed carotid plaque. Cerebrovasc Dis 35:370–377. https://doi.org/10.1159/000348846

26. Phelps MEE, Huang SCC, Hoffman EJJ, et al (1979) Tomographic measurement of local cerebral glucose metabolic rate in humans with (F-18)2-fluoro-2-deoxy-D-glucose: Validation of method. Ann Neurol 6:371–388. https://doi.org/10.1002/ana.410060502

27. Chen W, Dilsizian V (2015) PET assessment of vascular inflammation and atherosclerotic plaques: SUV or TBR? J. Nucl. Med.

28. Keyes JW (1995) SUV: standard uptake or silly useless value? J Nucl Med 36:1836–9

29. Rudd JHF, Myers KS, Bansilal S, et al (2008) Atherosclerosis inflammation imaging with 18F-FDG PET: Carotid, iliac, and femoral uptake reproducibility, quantification methods, and recommendations. J Nucl Med. https://doi.org/10.2967/jnumed.107.050294

30. Lammertsma AA (2017) Forward to the past: The case for quantitative PET imaging. J. Nucl. Med. 58:1019–1024

31. Kitagawa T, Yamamoto H, Horiguchi J, et al (2009) Characterization of Noncalcified Coronary Plaques and Identification of Culprit Lesions in Patients With Acute Coronary Syndrome by 64-Slice Computed Tomography. JACC Cardiovasc Imaging. https://doi.org/10.1016/j.jcmg.2008.09.015

32. Schroeder S, Kuettner A, Leitritz M, et al (2004) Reliability of differentiating human coronary plaque morphology using contrast-enhanced multislice spiral computed tomography: A comparison with histology. J Comput Assist Tomogr. https://doi.org/10.1097/00004728-200407000-00003

33. Schlett CL, Maurovich-Horvat P, Ferencik M, et al (2013) Histogram analysis of lipid-core plaques in coronary computed tomographic angiography: Ex vivo validation against histology. Invest Radiol. https://doi.org/10.1097/RLI.0b013e31828fdf9f

34. Torizuka T, Nobezawa S, Momiki S, et al (2000) Short dynamic FDG-PET imaging protocol for patients with lung cancer. Eur J Nucl Med 27:1538–1542. https://doi.org/10.1007/s002590000312

35. Caselles V, Kimmel R, Sapiro G (1997) Geodesic Active Contours. Int J Comput Vis 22:61–79. https://doi.org/10.1023/A:1007979827043

36. Derlin T, Wisotzki C, Richter U, et al (2011) In vivo imaging of mineral deposition in carotid plaque using 18F-sodium fluoride PET/CT: Correlation with atherogenic risk factors. J Nucl Med 52:362–368. https://doi.org/10.2967/jnumed.110.081208

37. Ohya M, Otani H, Kimura K, et al (2011) Vascular calcification estimated by aortic calcification area index is a significant predictive parameter of cardiovascular mortality in hemodialysis patients. Clin Exp Nephrol. https://doi.org/10.1007/s10157-011-0517-y

38. Kohei Arai and Ali Ridho Barakbah (2007) Hierarchical K-means: An algorithm for centroids initialization for K-means | Request PDF

39. Rousseeuw PJ (1987) Silhouettes: A graphical aid to the interpretation and validation of cluster analysis. J Comput Appl Math 20:53–65. https://doi.org/10.1016/0377-0427(87)90125-7

40. Agatston AS, Janowitz WR, Hildner FJ, et al (1990) Quantification of coronary artery calcium using ultrafast computed tomography. J Am Coll Cardiol 15:827–832. https://doi.org/10.1016/0735-1097(90)90282-T

41. Van Der Bijl N, Joemai RMS, Geleijns J, et al (2010) Assessment of Agatston coronary artery calcium score using contrast-enhanced CT coronary angiography. Am J Roentgenol 195:1299–1305. https://doi.org/10.2214/AJR.09.3734

42. McEvoy JW, Blaha MJ, DeFilippis AP, et al (2010) Coronary artery calcium progression: An important clinical measurement? J. Am. Coll. Cardiol.

43. Bentourkia M (2005) Kinetic modeling of PET data without blood sampling. IEEE Trans Nucl Sci 52:697–702. https://doi.org/10.1109/TNS.2005.851442

44. Wu HM, Hoh CK, Choi Y, et al (1995) Factor analysis for extraction of blood time-activity curves in dynamic FDG-PET studies. J Nucl Med 36:1714–1722

45. Christensen AN, Reichkendler MH, Larsen R, et al (2014) Calibrated image-derived input functions for the determination of the metabolic uptake rate of glucose with

[18F]-FDG   PET.   Nucl   Med   Commun. https://doi.org/10.1097/MNM.0000000000000063

46. De Geus-Oei LF, Visser EP, Krabbe PFM, et al (2006) Comparison of image-derived and arterial input functions for estimating the rate of glucose metabolism in therapy-monitoring 18F-FDG PET studies. J Nucl Med

47. Chen W, Dilsizian V (2013) Targeted PET/CT imaging of vulnerable atherosclerotic plaques: Microcalcification with sodium fluoride and inflammation with fluorodeoxyglucose. Curr Cardiol Rep. https://doi.org/10.1007/s11886-013-0364-4

48. Blaha MJ, Mortensen MB, Kianoush S, et al (2017) Coronary Artery Calcium Scoring: Is It Time for a Change in Methodology? JACC Cardiovasc. Imaging 10:923–937

49. Li Z, Hou Z, Yin W, et al (2016) Effects of statin therapy on progression of mild noncalcified coronary plaque assessed by serial coronary computed tomography angiography: A multicenter prospective study. Am Heart J 180:29–38. https://doi.org/10.1016/j.ahj.2016.06.023

8. PRELIMINARY ANALYSIS OF ^{18}F-NAF PET/CT AND CT WITH CONTRAST AGENT

Evaluation of ^{18}F-NaF uptake and wall attenuation in the arteries using PET/CT and CTA for vulnerable plaque detection.

Mamdouh S. Al-enezi, M'hamed Bentourkia

Résumé:

Le but de cette étude est de corréler l'absorption de fluorure de ^{18}F-sodium (^{18}F-NaF) dans l'aorte et l'iliaque avec une valeur seuil $\leq$ 50 HU sur la paroi artérielle (plaque non calcifiée, NCP) en tenant compte de la densité de calcification, des aires de calcification, et des scores.

Méthodes : 107 segments d'artère de cinq volontaires avec athérosclérose (non oncologiques) ont été inclus dans cette étude. La captation du ^{18}F-NaF a été corrigée pour l'activité du pool sanguin (TBR) et l'effet de volume partiel. L'angiographie par la tomodensitométrie (ATDM) a été utilisée pour la segmentation des images TDM des artères, et la tomodensitométrie à faible dose couplée avec la TEP a été utilisée pour la mesure de la densité de calcification, de l'aire de la plaque et de leurs scores. La NCP sur les images avec la TDM a été mesurée sur la paroi de l'artère dans une valeur seuil $\leq$ 50 HU pour une plaque d'aire supérieure à 5 pixels contigus.

Résultats : La relation inverse entre le TBR et la densité des plaques, l'aire calcifiée et les scores a été observée. Parmi ces paramètres, seule l'aire s'est révélée statistiquement significative entre la petite étendue et la plus grande étendue de la plaque (p = 0,04). La NCP est statistiquement plus élevée par rapport aux segments normaux (p = 0,002) et aux segments calcifiés à une seule aire de calcification (p= 0,003) mais pas aux segments avec multiple aires de calcification (p = 0,14). Une valeur seuil sur le TBR utilisant la fonction d'efficacité du récepteur a été déterminée à 2.5 avec une sensibilité de 97% et une spécificité de 81%.

Conclusion : Il existe une corrélation inverse de la région de calcification avec la captation de ^{18}F-NaF. Il a été constaté une augmentation de la captation de ^{18}F-NaF avec des régions de calcifications avec segments multiples. NCP ($\leq$ 50 HU) avec une valeur seuil de TBR comprise entre 2.5 et 2.6 peuvent refléter le NCP avec une ostéogenèse active.

Mots clés : Fluorure de sodium; athérosclérose; calcification; ostéogenèse; TEP/TDM.

Evaluation of ^{18}F-NaF uptake and wall attenuation in the arteries using PET/CT and CTA for vulnerable plaque detection.

Mamdouh S. Al-enezi, M'hamed Bentourkia

Abstract

The purpose of this study was to correlate ^{18}F-sodium fluoride (^{18}F-NaF) uptake in artery PET images with non-calcified plaque (NCP), calcification density, area, scores and single or spotty calcified segments in CT images.

Methods: 107 artery segments from 5 atherosclerotic (non-oncologic) volunteers were included in this study. Tissue to blood ratio (TBR) values from PET images were corrected for partial volume effect. Computed tomography angiography was used for CT segmentation and low attenuation CT was used for calcification density, area and score measurements. NCP was measured on the arterial wall within a cut-off values of ≤ 50 HU for calcification segments made of more than 5 contiguous pixels.

Results: The reverse relationships between TBR obtained with PET and density, area and scores obtained with CT were observed although only area was found statistically significantly different between small area and the largest area (p = 0.04). NCP was higher compared to normal segments (p = 0.002) and single calcified segments (p = 0.003), but not against spotty calcified segments (p = 0.14). A cut-off TBR values of NCP was determined as 2.5 with a sensitivity of 97% by utilizing receiver operating characteristic curve.

Conclusions: There is a reverse correlation of calcification area with TBR. TBR increases with spotty calcifications. ^{18}F-NaF uptake could be a marker for ongoing calcification activity and NCP. NCP (≤ 50 HU of the arterial wall) identified on CT was correlated with significant ^{18}F-NaF uptake. A cut-off value of TBR of 2.5 may reflect active osteogenesis.

Introduction

Atherosclerosis is a vascular disease in which a plaque builds up inside the arterial wall leading to narrowing and hardening the artery. The plaque could be prone to rupture resulting in severe complication including sudden death [1], [2]. Thus, identifying the vulnerable plaque could limit atherosclerosis complications [3].

Noninvasive detection of arterial calcification depicted on computed tomography (CT) is an important feature of atherosclerotic disease, where the abdominal aortic calcification is associated with increased severe atherosclerosis complication [4]–[6]. The cellular microcalcifications was correlated with inflammation and the early stage of atherosclerotic plaque, this microcalcification is considered a marker of vulnerable plaque throughout thinning or weakening the fibrous cap due to the induction of local stress [7]–[9].

Arterial calcification is now recognized to be an active process analogous to osteogenesis [10], [11]. Therefore, ^{18}F-sodium fluoride (^{18}F-NaF) is a radiotracer that follows the calcium metabolism which was first utilized to detect osseous metastasis [12] and it has been reported to identify the microcalcification activity in unstable plaques noninvasively [13], [14]. Recently, ^{18}F-NaF in combination with computed tomography angiography (CTA) was reported to be a biomarker of vulnerable plaque with high precision and reproducibility [15], in addition to its clear coupling with atherosclerosis risk profile [16]. The low attenuation plaque (≤ 50 HU) in arterial wall was identified as non-calcified plaque with high positive predictivity of the presence of advanced plaque [17], [18].

We aimed in this study to determine ^{18}F-NaF uptake with low wall attenuation ≤ 50 HU in attempt to investigate the possibility of identifying the presence of micro-calcification in non-calcified plaque. ^{18}F-NaF uptake was assessed in the aorta and iliac and associated with calcification parameters (intensity, area, scores and phenotypes of calcification "attached and spotty").

Material and methods

PET/CT Imaging

^{18}F-NaF PET/CT was performed on Gemini TF 16-slice PET/CT scanner (Philips) for five volunteers (non-oncologic patients). A non–contrast-enhanced CT scan was acquired

first in a 512 × 512 data matrix and pixel size of 1 × 1 × 4 mm^3 in headfirst spine position with tube potential of 120 kVp.

After the CT scan, PET data were acquired in a dynamic mode for 40 min (12 × 10 secs, 8 × 30 secs, 8 × 180 secs and 2 × 300 secs) immediately after intravenous activity injection of 251 MBq of ^{18}F-NaF (normalized to body's weight) with a 144 × 144 data matrix and in-plane spatial resolution of 4 mm covering the same field of view as in CT. PET and CT images were reconstructed using three-dimensional row action maximum likelihood algorithm (3D-RAMLA).

CTA imaging

CTA scan was acquired afterward in a 512 × 512 data matrix with a pixel size of 0.8 × 0.8 × 0.5 mm^3, and a tube potential of 120 kVp after an injection of an iodinated contrast agent (370 mg/ml with a bolus volume of 100 ml at a flow rate of 3 ml/sec).

Image analysis

Artery PET images were segmented by utilizing edge-based active contours algorithm [20] on the mean of the first 6 image time frames on each transaxial slice. With the same algorithm, the arterial regions on CTA were segmented, and the resulted regions of interest ROIs were co-registered on corresponding non-enhanced CT slices. The segmented CTA ROIs were also used for diameter and area measurements in the purpose of partial volume effect correction (PVC) and the ratio of calcification area (RCA).

Tissue to blood ratio (TBR) was computed on artery PET images per segment as a ratio of the measured activity (maximum 75% of ROI) to the mean blood pool activity. The blood pool activity measurement was performed by drawing a single ROI in the center of the superior vena cava (SVC) from decay-corrected PET images. SVC is a better region for blood-pool correction due to easiness of its isolated location and width in the images. It is also considered least subject to spillover contamination from adjacent ^{18}F-NaF-avid structures and accurately estimated using single ROI [21].

Calcification was visually identified in non-enhanced CT images and a peak CT density ≥ 130 HU with more than 2 contiguous pixels is deemed a start of calcification [22]. RCA

was determined cross-sectionally per slice as a calcification area normalized to whole arterial area. The calcification intensity (CI) was weighted to 4 levels as in Table 8.1.

Agatston calcification score (ACS) was calculated by multiplying the weighted levels and RCA per segment. Both RCA and ACS were automatically clustered throughout the use of Automatic Hierarchical K-means algorithm (AHK) [23] and AHK was enhanced with the use of silhouette-coefficient [24]. The corresponding TBR values were paired to the clustered RCA and ACS to associate ^{18}F-NaF uptake with RCA and ACS clusters in addition to CI levels (Table 8.1).

The identified ROI of arterial wall with the help of CTA image was used to segment the wall on CT images having a density less than 50 HU and having segments of more than 5 contiguous pixels as identified by histogram thresholding. Such segments were assumed to reflect the non-calcified plaque (NCP). A receiver operating characteristic (ROC) curve analysis was used for identifying the optimal cut-off value of TBR in comparison to NCP segments.

Table 8.1 Calcification intensity ranges and corresponding Agatston weighted factors ([22]).

	INTENSITY RANGE (HU)	WEIGHTED FACTOR
IC1	130 – 199	1
IC2	200 – 299	2
IC3	300 – 399	3
IC4	> 399	4

Statistical analysis:

Wilcoxon/Mann-Whitney U tests were applied for intra- and inter-group comparisons of the quantitative parameters. Continuous variables were expressed as mean ± STD for normally distributed data and median (interquartile range [IQR]) for skewed distributions. For the ROC analysis, sensitivity and specificity were calculated for different cut-off points of TBR, for NCP segments, and the optimal cut-off TBR value was computed as an

intersection point between sensitivity and specificity values and according to CLSI/NCCLS guidelines [25]. Statistical significance was assumed for p-values < 0.05.

Results

A total of 107 artery segments have been analyzed for aorta and iliac, of which, 78 segments were not calcified (having intensity below 130 HU) and 29 were with calcification.

TBR values were calculated per artery segment by considering the blood pool activity from SVC that was identified on PET images (Figure 8.1C and D) at the last 4 data points of the time activity curve (TAC) (mean of last 4 frames of dynamic PET images, 16 min).
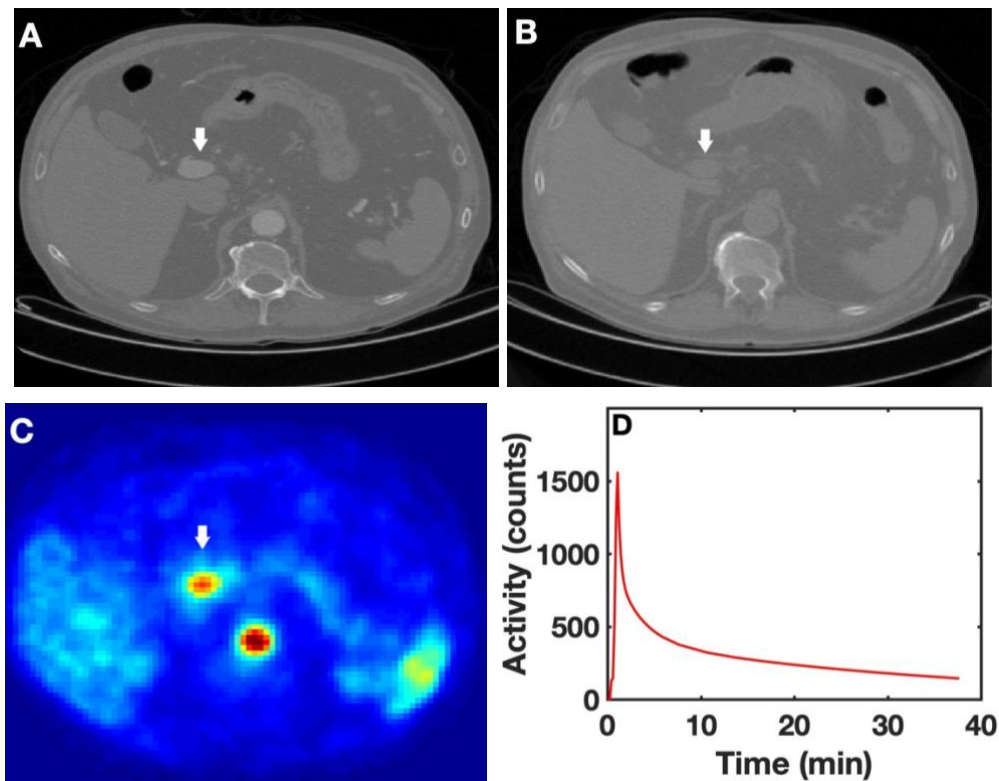
Figure 8.1 A) CTA image showing superior vena cava (SVC, arrow). B) the corresponding low attenuation CT image. C) The corresponding PET image showing the aorta and SVC (arrow). D) The time activity curve of SVC.
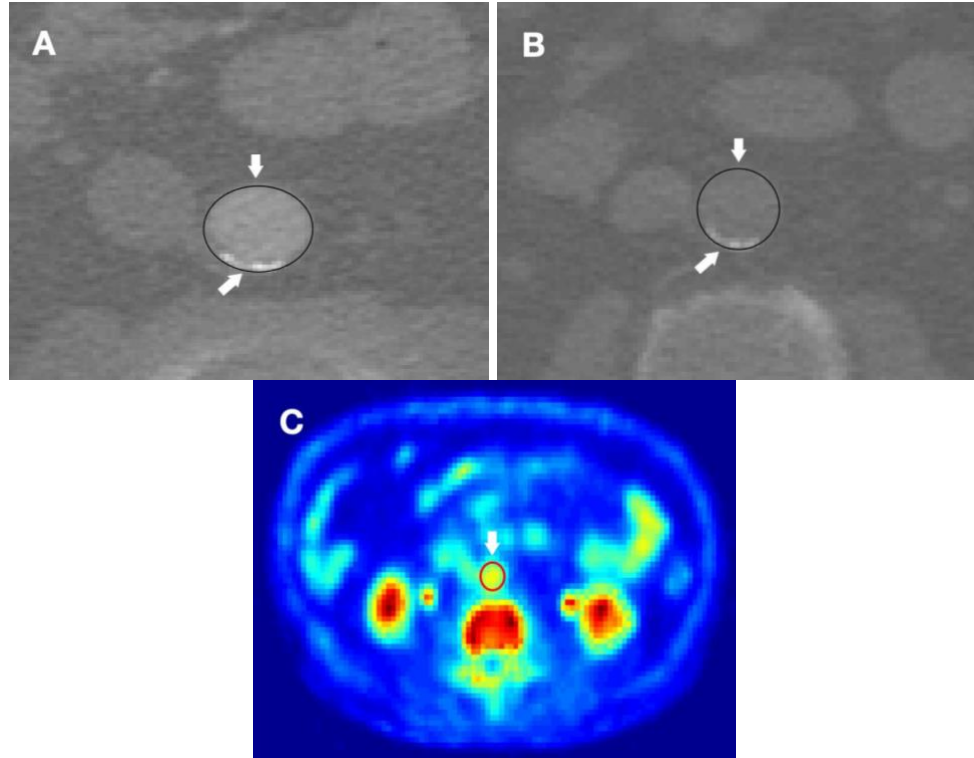
Figure 8.2 A) CTA image showing aorta (top arrow) and the calcification spots in the arterial wall (bottom arrows). B) the low dose CT with the same ROI drawn on CTA. C) The corresponding PET image of the mean of the last 4 image frames.

Figure 8.2 shows the calcification on the aorta wall with its corresponding PET slice.

The mean TBR value of all analyzed segments was 2.03 ± 0.70, and the TBR values as a function of each classified group of segments were summarized in Table 8.2.

The obtained wall thickness was used to produce a ring like binary image of a thicknesses with respect to the diameter D_i and ROI_i center of gravity. Average RCA was 0.1 ± 0.05 and average score was 0.30 ± 0.24.

Table 8.2 TBR values for the classified groups from all recruited subjects.

classified group	Mean±STD	Median	Quartiles	IQR
NCST	1.98 ± 0.72	1.84	1.41 – 2.40	0.99
CST	2.17 ± 0.61	2.37	1.79 – 2.62	0.83
NCSN	1.90 ± 0.68	1.71	1.41 – 2.32	0.91
NCP	2.9 ± 0.33	2.84	2.68 – 3.00	0.31
SS	2.03 ± 0.63	2.26	1.48 – 2.47	0.99
MS	2.60 ± 0.30	2.70	2.38 – 2.74	0.36
CI1	2.23 ± 0.88	2.52	1.70 – 2.76	1.06
CI2	2.23 ± 0.61	2.40	1.93 – 2.68	0.75
CI3	2.11 ± 0.22	2.11	1.95 – 2.27	0.32
CI4	1.84 ± 0.58	1.86	1.36 – 2.33	0.98
ACS1	2.33 ± 0.69	2.53	1.64 – 2.69	1.05
ACS2	2.18 ± 0.59	2.31	2.13 – 2.55	0.42
ACS3	2.00 ± 0.48	2.25	1.60 – 2.38	0.78
RCA1	2.36 ± 0.64	2.68	2.14 – 2.73	0.59
RCA2	2.00 ± 0.73	2.20	1.52 – 2.46	0.94
RCA3	2.02 ± 0.53	2.26	1.40 – 2.43	1.03

NCST: non-calcified segments–total. CST: calcified segments–total. NCSN: non-calcified segments–normal only. NCP: non-calcified plaque. SS: single-spot calcified segments. MS: Multi-spots calcified segments. CI: calcification intensity level. ACS: Agatston calcification score-cluster. RCA: Ratio of calcification area-cluster.
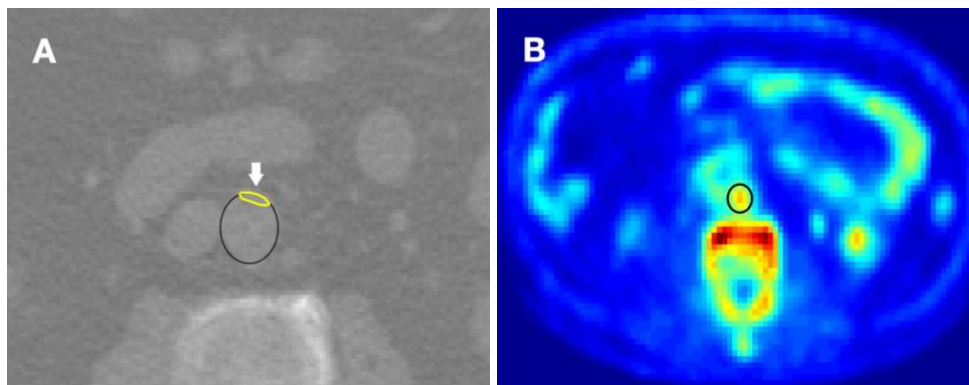
Figure 8.3 A) CT image showing aorta and active osteogenesis region of the wall (arrow). B), the corresponding PET image.

Figure 8.3A shows the resulted identified region of a window at 60-90 HU that met the conditions aforementioned for active osteogenesis region determination. The region was shown with its corresponding PET image and it was with TBR = 3.00. Overall, there were 8 segments having osteogenesis.
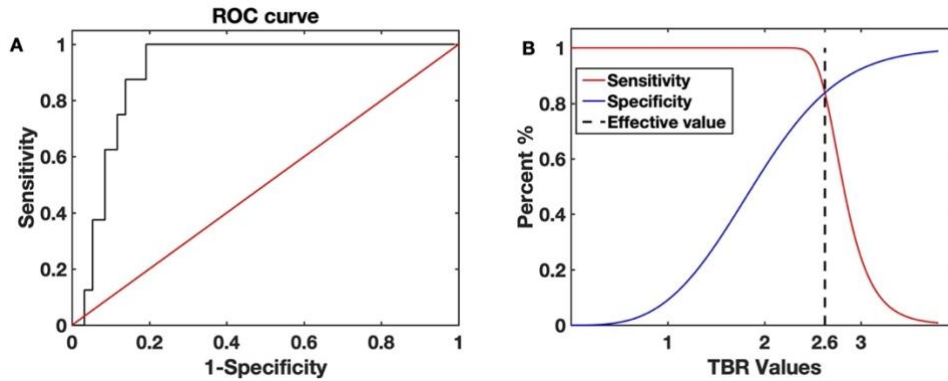
Figure 8.4 A) The receiver operating characteristic (ROC) curve for 60-90 HU CT window. B), the cut-off TBR value optimization.

The area under the receiver operating characteristic (ROC) curve was 0.95. The two cut-off values of 2.6 (intersection point) as in Figure 8.4B and 8.5 identified as a peak value from a plot of the average of sensitivity and specificity versus the cut-off TBR values according to CLSI/NCCLS guidelines [25]. The cut-off value of 2.6 for TBR is with a sensitivity of 88% and specificity of 84% and 2.5 cut-off value is with sensitivity of 97% and specificity of 81%.

There were a reverse association of ^{18}F-NaF uptake as a function of intensity and scores, however, the difference was not significant ($p > 0.05$).

For the RCA clusters, a reverse association of ^{18}F-NaF uptake as a function of area was observed, while RCA3 was statistically significantly different compared to RCA1 ($p = 0.04$) but not with RCA2 ($p > 0.05$) (Figure 8.5).

We compared all non-calcified segments versus all calcification segments, the difference was not statistically significant ($p = 0.1$), however, when the NCP were excluded (Figure 8.6), the comparison was significantly different, where the calcification has higher TBR value ($p = 0.03$).

Multi-spots calcified segments (MS) was statistically significantly different from both non-calcified segments (NCSN) and single-spot calcified segments (SS) (p = 0.004 and 0.018 respectively). While NCSN and SS were not statistically different (p = 0.25).

NCP was also statistically higher compared to NCSN (p = 0.002) and SS (p = 0.003) but not MS (p = 0.14).
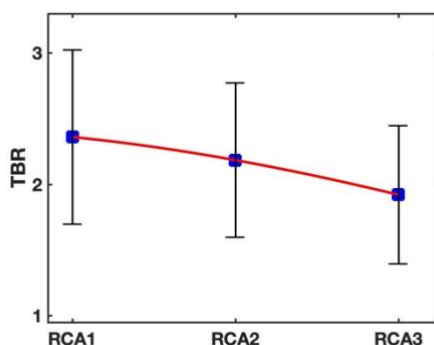
Figure 8.5 The relation between equivalent TBR values to calcification area clusters (RCAs).
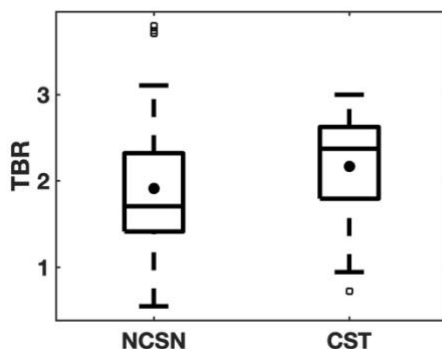
Figure 8.6 Box plot comparing TBR values for normal non-calcified segments (NCSN) and all calcified segments (CST).
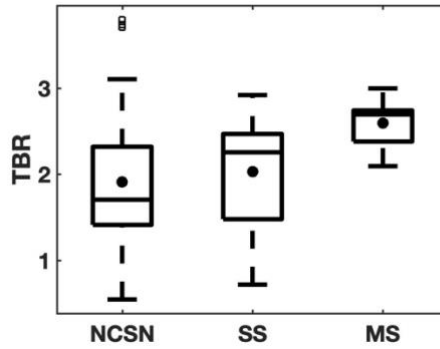
Figure 8.7 Box-and-whisker plot comparing TBR values for normal non-calcified segments (NCSN) with single (SS) and multi-spots (MS) calcified segments.

Discussion

Calcium phosphate deposition in the vessel wall is thermodynamically unfavorable reaction [29] and increases local mechanical stress in the fibrous cap, that may facilitate plaque vulnerability [16], therefore, plaques prone to rupture may demonstrate regions of micro-calcification [30], [31]. ^{18}F-NaF however, can distinguish between areas of macro- and microcalcification and therefore, it may identify the vulnerable plaque.

This study provides a methodological way of ^{18}F-NaF quantification in the combination with CT and CTA and establishes a quantitative framework for detecting the active osteogenesis regions within the arterial wall on CT images.

The difference between non-calcified segments that are assigned normal (NCSN, having no plaque and therefore no calcification) and the calcification segments were found in this work statistically significant. This difference was mainly due to the contribution of ^{18}F-NaF uptake of spotty calcification group, where this group was significantly different (p= 0.004) from NCSN. Additionally, NCSN shows no statistical difference in comparison to single spot (p = 0.25). This finding is in the agreement of other findings reporting a clear correlation between ^{18}F-NaF uptake with spotty calcification [32]. The area was reported herein to be inversely related to TBR values where the largest area was significantly lower compared to the smaller area (p = 0.04). The same pattern was observed for density and scores and may be due to the data sets that are small, they did not show statistical significance. Others have demonstrated such a relation with increased calcification area and scores [33], [34].

Besides, we approximated the arterial wall region in an attempt to correlate the attenuation values of the wall in CT image with ^{18}F-NaF TBR values. The cut-off values of $\leq$ 50 HU on the arterial wall (NCP) was shown to be in agreement with higher TBR values of the corresponding PET slices. NCP regions were with median TBR of 2.84 [IQR: 2.68 – 3.00], Table 8.2 shows values very close to those recently published for the microcalcification at TBR of 2.61 [IQR: 2.50 to 2.77] for ^{18}F-NaF [35]. Although the cut-off values were different in our study, our maximum cut-off value was identified using ROC curve at 2.5 to 2.6 and those from the literature was 2.11, this may be due to the way used to predict the cut-off value.

In a histopathologic analysis of human coronary arteries [36], a clear association of ^{18}F-NaF uptake to a confirmed microcalcification has been demonstrated and the uptake was not significant between plaques with both microcalcification and macrocalcification and plaques with only microcalcification (p = 0.9). In our study, we observed the same, as there was no significant difference between NCP with and without calcification and NCP without calcification (p = 0.7), the median was 2.84 [IQR, 2.690 – 3.00] and 2.87 [IQR, 2.79 - 3.16] respectively.

The current study is accompanied by limitations, including the number of recruited subjects that were small, although they are non-oncologic patients. Moreover, the wall thickness was under assumption of symmetry which might cause the thickness to be overestimated.

Conclusion

^{18}F-NaF uptake is a marker for calcification activity. There is a reverse correlation of calcification area with ^{18}F-NaF uptake. ^{18}F-NaF uptake increased with area of spotty calcifications. NCP ($\leq$ 50 HU of the arterial wall) identified on CT image was correlated with significant ^{18}F-NaF uptake. A cut-off value of TBR at 2.5 may reflect active osteogenesis region. Further studies need to be carried out in order to validate the findings in the current work.

Major findings of the research:

The main objective was to analyze the ^{18}F-NaF uptake that is corrected for blood pool activity and partial volume effect as a function of maximum density, area, and extent of calcification. Additionally, we have correlated the uptake of ^{18}F-NaF with non-calcified plaque of arterial wall on CT and CTA. We found a reverse correlation of calcification area with ^{18}F-NaF uptake and a situ correlation of ^{18}F-NaF uptake with non-calcified plaque using a threshold of 50 HU on the arterial wall.

References

[1]   R. Virmani *et al.*, "Atherosclerotic Plaque Progression and Vulnerability to Rupture," *Arterioscler. Thromb. Vasc. Biol.*, vol. 25, no. 10, pp. 2054–2061, Oct. 2005.

[2]   P. Libby, P. M. Ridker, and G. K. Hansson, "Inflammation in Atherosclerosis. From Pathophysiology to Practice," *Journal of the American College of Cardiology*, vol. 54, no. 23. NIH Public Access, pp. 2129–2138, 01-Dec-2009.

[3]   M. S. Al-enezi *et al.*, "Assessment of artery calcification in atherosclerosis with dynamic 18F-FDG-PET/CT imaging in elderly subjects," *Int. J. Cardiovasc. Imaging*, vol. 35, no. 5, pp. 947–954, May 2019.

[4]   P. W. F. Wilson *et al.*, "Abdominal aortic calcific deposits are an important predictor of vascular morbidity and mortality," *Circulation*, vol. 103, no. 11, pp. 1529–1534, Mar. 2001.

[5]   C. R. Walsh *et al.*, "Abdominal aortic calcific deposits are associated with increased risk for congestive heart failure: The Framingham Heart Study," *Am. Heart J.*, vol. 144, no. 4, pp. 733–739, Oct. 2002.

[6]   J. Takasu, S. Mao, and M. J. Budoff, "Aortic atherosclerosis detected with electronbeam CT as a predictor of obstructive coronary artery disease," *Acad. Radiol.*, vol. 10, no. 6, pp. 631–637, Jun. 2003.

[7]   E. Aikawa *et al.*, "Osteogenesis associates with inflammation in early-stage atherosclerosis evaluated by molecular imaging in vivo," *Circulation*, vol. 116, no. 24, pp. 2841–2850, Dec. 2007.

[8]   O. Tzang, K. Kfir, E. Flaxer, O. Cheshnovsky, and S. Einav, "Detection of Microcalcification in Tissue by Raman Spectroscopy," *Cardiovasc. Eng. Technol.*, vol. 2, no. 3, pp. 228–233, Sep. 2011.

[9]   Y. Vengrenyuk *et al.*, "A hypothesis for vulnerable plaque rupture due to stress-induced debonding around cellular microcalcifications in thin fibrous caps," *Proc. Natl. Acad. Sci. U. S. A.*, vol. 103, no. 40, pp. 14678–14683, Oct. 2006.

[10] J. L. Hunt *et al.*, "Bone formation in carotid plaques: A Clinicopathological study," *Stroke*, vol. 33, no. 5, pp. 1214–1219, 2002.

[11] L. L. Demer, "Vascular calcification and osteoporosis: Inflammatory responses to oxidized lipids," *International Journal of Epidemiology*, vol. 31, no. 4. Oxford University Press, pp. 737–741, 2002.

[12] M BLAU, W NAGLER, and M A BENDER, "Fluorine-18: a new isotope for bone scanning," *J Nucl. Med.*, vol. 3, pp. 332–334, 1962.

[13] T. Derlin *et al.*, "Feasibility of 18F-sodium fluoride PET/CT for imaging of atherosclerotic plaque," *J. Nucl. Med.*, vol. 51, no. 6, pp. 862–865, Jun. 2010.

[14] N. V. Joshi *et al.*, "18F-fluoride positron emission tomography for identification of ruptured and high-risk coronary atherosclerotic plaques: A prospective clinical trial," *Lancet*, vol. 383, no. 9918, pp. 705–713, Feb. 2014.

[15] A. J. Moss *et al.*, "Molecular coronary plaque imaging using 18f-fluoride," *Circ. Cardiovasc. Imaging*, vol. 12, no. 8, Aug. 2019.

[16] B. A. Blomberg *et al.*, "Thoracic aorta calcification but not inflammation is associated with increased cardiovascular disease risk: results of the CAMONA study," *Eur. J. Nucl. Med. Mol. Imaging*, vol. 44, no. 2, pp. 249–258, Feb. 2017.

[17] P. Maurovich-Horvat *et al.*, "The napkin-ring sign indicates advanced atherosclerotic lesions in coronary CT angiography," *JACC Cardiovasc. Imaging*, vol. 5, no. 12, pp. 1243–1252, Dec. 2012.

[18] M. Das *et al.*, "Carotid Plaque Analysis: Comparison of Dual-Source Computed Tomography (CT) Findings and Histopathological Correlation," *Eur. J. Vasc. Endovasc. Surg.*, vol. 38, no. 1, pp. 14–19, Jul. 2009.

[19] K. B. Baron, A. D. Choi, and M. Y. Chen, "Low Radiation Dose Calcium Scoring: Evidence and Techniques," *Current Cardiovascular Imaging Reports*, vol. 9, no. 4. Current Medicine Group LLC 1, 01-Apr-2016.

[20] V. Caselles, R. Kimmel, and G. Sapiro, "Geodesic Active Contours," *Int. J. Comput. Vis.*, vol. 22, no. 1, pp. 61–79, 1997.

[21] B. A. Blomberg *et al.*, "Impact of Personal Characteristics and Technical Factors on Quantification of Sodium 18F-Fluoride Uptake in Human Arteries: Prospective Evaluation of Healthy Subjects," *J. Nucl. Med.*, vol. 56, no. 10, pp. 1534–1540, Oct. 2015.

[22] N. Van Der Bijl *et al.*, "Assessment of Agatston coronary artery calcium score using contrast-enhanced CT coronary angiography," *Am. J. Roentgenol.*, vol. 195, no. 6, pp. 1299–1305, Dec. 2010.

[23] P. Filzmoser, R. Baumgartner, and E. Moser, "A hierarchical clustering method for analyzing functional MR images," *Magn. Reson. Imaging*, vol. 17, no. 6, pp. 817–826, Jul. 1999.

[24] P. J. Rousseeuw, "Silhouettes: A graphical aid to the interpretation and validation of cluster analysis," *J. Comput. Appl. Math.*, vol. 20, pp. 53–65, Nov. 1987.

[25] H. Hautzel, O. Sander, A. Heinzel, M. Schneider, and H. W. Müller, "Assessment of large-vessel involvement in giant cell arteritis with 18F-FDG PET: Introducing an ROC-analysis-based cutoff ratio," *J. Nucl. Med.*, vol. 49, no. 7, pp. 1107–1113, Jul. 2008.

[26] T. L. Assimes *et al.*, "Susceptibility locus for clinical and subclinical coronary artery disease at chromosome 9p21 in the multi-ethnic ADVANCE study," *Hum. Mol. Genet.*, vol. 17, no. 15, pp. 2320–2328, Aug. 2008.

[27] Z. Al Aly and J. C. Edwards, "Vascular biology in uremia: Insights into novel mechanisms of vascular injury," *Adv. Chronic Kidney Dis.*, vol. 11, no. 3, pp. 310–318, 2004.

[28] S. Kathiresan *et al.*, "Genome-wide association of early-onset myocardial infarction with single nucleotide polymorphisms and copy number variants," *Nat. Genet.*, vol. 41, no. 3, pp. 334–341, 2009.

[29] M. A. Hofmann Bowman and E. M. McNally, "Genetic Pathways of Vascular Calcification," *Trends in Cardiovascular Medicine*, vol. 22, no. 4. NIH Public Access, pp. 93–98, May-2012.

[30] A. J. Moss, P. D. Adamson, D. E. Newby, and M. R. Dweck, "Positron emission tomography imaging of coronary atherosclerosis," *Future Cardiology*, vol. 12, no. 4. Future Medicine Ltd., pp. 483–496, 01-Jul-2016.

[31] J. W. Lee, S. H. Bae, J. W. Jeong, S. H. Kim, and K. W. Kim, "Hypoxia-inducible factor (HIF-1)α: Its protein stability and biological functions," *Experimental and Molecular Medicine*, vol. 36, no. 1. Korean Society of Med. Biochemistry and Mol. Biology, pp. 1–12, 29-Feb-2004.

[32] T. Kitagawa *et al.*, "Data on analysis of coronary atherosclerosis on computed tomography and 18F-sodium fluoride positron emission tomography," *Data Br.*, vol. 13, pp. 341–345, Aug. 2017.

[33] F. Fiz *et al.*, "18F-NaF uptake by atherosclerotic plaque on PET/CT imaging: Inverse correlation between calcification density and mineral metabolic activity," *J. Nucl. Med.*, vol. 56, no. 7, pp. 1019–1023, Jul. 2015.

[34] D. Dai, H. H. Chuang, H. A. Macapinlac, T. Li, and T. Pan, "Correlation of fluorine 18-labeled sodium fluoride uptake and arterial calcification on whole-body PET/CT in cancer patients," *Nucl. Med. Commun.*, vol. 40, no. 6, pp. 604–610, Jun. 2019.

[35] M. M. Chowdhury *et al.*, "Vascular Positron Emission Tomography and Restenosis in Symptomatic Peripheral Arterial Disease: A Prospective Clinical Study," *JACC Cardiovasc. Imaging*, vol. 13, no. 4, pp. 1008–1017, Apr. 2020.

[36] T. Youn *et al.*, "18F-sodium fluoride positron emission tomography/computed tomography in ex vivo human coronary arteries with histological

9. DISCUSSION

Atherosclerosis is an intimal plaque in the arterial wall responsible for mortality and morbidity worldwide. In 2016, it caused about 18 million deaths (> 30% of all deaths) (Mathers *et al.*, 2018) and counted third of all deaths in United States (Benjamin *et al.*, 2019).

PET is the most sensitive imaging modality, however, the assessment of PET signal for atherosclerosis was mostly carried in a semi-quantitative manner that could minimize the information obtained. Yet, most of published studies for atherosclerosis using PET imaging modality are either oncologic patients, where the influence of anticancer therapies could not be neglected, or by using the animal model to resemble human atherosclerosis, where the mouse is the predominant specie in the experimental atherosclerosis studies. Animals are differing from human atherosclerotic plaque and lack some approved vulnerable features of human plaque such as neovascularization and hemorrhage. Additionally, most studies predominantly condone the correction of partial volume effect that is a predominant factor affecting the accuracy of tracer's uptake particularly for small lesions (< 2 FWHM). Thus, this could lead to under-estimation of uptake.

One of the major imaging signs of atherosclerosis is the calcification that is usually visualized using CT images (standard imaging technique for calcification). In this regard, there are abundant of calcification score methods. Agatston score is a standard score and the similarity between Agatston score (AS) and volume score (VS) has been demonstrated (Rumberger and Kaufman, 2003). Albeit multi-spot (MS) may quantify the calcification more accurately and reproducibly in comparison to other scores and suggested to replace other scores (Ulzheimer and Kalender, 2003), its complexity might hinder its use. Yet, a study analyzing AS, VS and MS stated that no method of the three is preferable (Nasir *et al.*, 2004). Calcium coverage score (CCS) in the other side, does not account for intensity neither area of calcification but only the presence of calcification.

Agatston calcification scores (ACS) (Al-enezi *et al.*, 2019) were taken under consideration in both spatial distribution (area normalized to total area as in MS) and amount of calcified atherosclerotic plaque (density as in AS). Such an approach may overcome the limited vital information within each calcified plaque by scoring the total area as in the case of AS approach. We have reported both density and area in the comparison head-to-head

with ^{18}F-FDG uptake that allows the determination of the most predictive of those factors used for score measurements (area and density). As it is reported that area is a stronger predictive value for incident cardiovascular disease compared to density (Criqui *et al.*, 2014).

The spotty calcification (small and solid plaque calcification >130 HU) may be fraught with uncertainty when it is considered in the setting of calcification score measurements and could be the source of divergent conclusions. Spotty calcification is a dominant feature of vulnerable plaque and associated with 2-fold increase in plaque rupture, it has also been shown to be related to acute myocardial infarction and unstable angina pectoris (Ehara *et al.*, 2004; Fujii *et al.*, 2005; Van Velzen *et al.*, 2011; Mizukoshi *et al.*, 2013; Maurovich-Horvat *et al.*, 2014; Nerlekar *et al.*, 2018). A study of 300 patients with stable coronary artery disease (Kataoka *et al.*, 2014) demonstrated that the presence of spotty calcification imaged by frequency-domain OCT was significantly associated with thinner fibrous caps and larger lipid necrotic cores of atherosclerotic plaque (features of greater plaque vulnerability). Another study of 98 patients who received serial OCT imaging divided into the plaque rupture group (n = 38) and non-rupture group (n = 60), the number of spotty calcifications was shown to be significantly higher in the rupture group than in the non-rupture group (Sakaguchi *et al.*, 2016). We have shown in our study that spotty calcification is acting differently as a function of metabolic activity (^{18}F-FDG uptake) compared to coalesced calcification (Al-enezi *et al.*, 2019).

A common metrics for PET signal quantification are SUV and TBR of which non-phosphorylated ^{18}F-FDG is still a major contaminated factor. Kinetic modeling is by far a more reliable and reproducible approach. Such an approach is not predominantly utilized in clinical practice and particularly for atherosclerosis.

We are the first who used this approach in atherosclerotic patients. The challenge with this approach is the need of a prior knowledge of the blood time activity curve (TAC) usually obtained by blood sampling resulting in additional risk to both the patient and the operator. Another safe approach is by extracting it directly from the images as for oncologic patients. However, in the case of atherosclerosis where the blood always exist, is not appropriate to fit the blood TAC with itself, leading to restricting its use for atherosclerosis. We have demonstrated the feasibility of kinetic modeling for atherosclerosis quantification when the

blood TAC is extracted from factor analysis and it was comparable with kinetic modeling without a need of prior knowledge of blood TAC (WOBS) and independent of PVE (Al-enezi and Bentourkia, 2020).

CT imaging was focused on the calcification quantification of calcified atherosclerotic plaque. Recently, non-calcified plaque (NCP) identification using CT images has been attracting research interests, attempting to identify NCP using CT images, where low attenuation plaque (15-50 HU) morphologically introduced as lipid rich core while attenuation of 100 HU of the plaque tend to reflect fibrous plaque, in comparison with IVUS. Yet, plaques with attenuation ≤30 HU was associated with greater risk for plaque rupture or acute syndromes (Motoyama *et al.*, 2007). In another study considering a density ≤30 HU was measured for NCP with a sensitivity of 95% and specificity of 85% in the correlation with IVUS (Marwan *et al.*, 2011). The density ≤50 HU of napkin-ring plaques (Maurovich-Horvat *et al.*, 2012) has reported a high specificity and high positive predictive value for the presence of high-risk lesions. Others have shown that the mean HU of NCP was in the range of about 9-11 HU in comparison with catheter angiography (Thilo *et al.*, 2011). We have found that density ≤50 HU (NCP) was metabolically more sensitive compared to density ≤30 HU with respect to ^{18}F-FDG uptake. Additionally, Statin therapy was shown to highly reduce the inflammation seen by ^{18}F-FDG uptake in NCP as it was also reported elsewhere (Lo *et al.*, 2015). Yet, there are concerns in the reliability of such approach, one of the concerns is the effect of overlapped attenuation values (HU) of lipid-rich and fibrous plaques (Dalager, Bøttcher, Andersen, *et al.*, 2011) that might hinder HU to be able to differentiate plaque components (Achenbach, 2008). Additionally, variability in acquisition parameters, including slice thickness, tube voltage (Dalager, Bøttcher, Dalager, *et al.*, 2011; Horiguchi *et al.*, 2011)), reconstruction algorithms (Achenbach *et al.*, 2010) and image noise and filtering (Cademartiri *et al.*, 2007) could cause alteration in HU, all of which might explain the differences in the cut-off values for NCP in the previous studies.

The last study in this thesis provides a methodological way of ^{18}F-NaF quantification in the combination with CT and CTA and establishes a quantitative framework for detecting the active osteogenesis regions within the arterial wall on CT images. We proposed a method to approximate the arterial wall region in attempt to correlate the attenuation values of the

wall in CT image with TBR values in ^{18}F-NaF-PET images. The density ≤50 HU on the arterial wall was shown to be in coupling with higher TBR values of the corresponding PET slices that may reflect osteogenesis activity. Yet, when these segments were excluded from non-calcified segments, the difference to the calcification segments were statistically significant. Additionally, we found that the spotty calcification segments were having higher TBR compared to single spot calcification segments but not for NCP group. This may indicate both spotty calcification and NCP segments were having active osteogenesis. We also found that 2.5 TBR values of ^{18}F-NaF on PET image alone may reflect osteogenesis activity.

In our study, all recruited volunteers were not oncological patients, and they have not undergone medications except medications specified for atherosclerosis. Furthermore, we assessed the inflammation of atherosclerotic plaque quantitatively using fractional uptake rate instead of SUV, where SUV is under assumption that the integral of the time activity curve of a tracer in blood is proportional to injected activity divided by body weight. Thus, for patients who are undergoing chemotherapy or hormone-therapy, the dynamics of blood ^{18}F-FDG could be remarkably affected and diverge from what is anticipated from the injected activity and body weight. Therefore, the computed SUV in this situation would not reliably dovetail to the kinetic influx rate.

These studies have some limitations. The small number of subjects that may affect the statistics, and a larger study population is needed. The arterial diameters were computed from CT images for partial volume effect correction and might underestimate or overestimate the corrected activity within the selected region, therefore, enhanced CT images would overcome such source of uncertainty. For NCP assessment, the wall thickness of the artery was determined assuming it is symmetric for simplification which might cause the thickness to be overestimated and NCP identification may be prone to errors caused by interscan variability.

10.   CONCLUSIONS AND PERSPECTIVES

This dissertation is consisting of four objectives.

The first objective was to study the correlation between calcification parameters and artery inflammation assessed using the fractional uptake rate (FUR) after partial volume correction. FUR values were correlated to the calcifications identified in CT images and quantified based on the spotty of calcifications, attached calcification and calcification score in the arterial wall of aorta and iliac. We also compared the inflammation represented by FUR in the hypercholesteremia subjects before and after Statin therapy within 12-months. We concluded that ^{18}F-FDG uptake represented by FUR varied for non-calcified and calcified segments and with medication. Arterial segments having multi-spots of calcification had different metabolic activity as estimated with FUR compared to those with single spot of calcification. This article was published in The International Journal of Cardiovascular Imaging.

The second objective was to apply the pharmacokinetic modeling in atherosclerosis settings. We computed the metabolic rate of glucose (MRG) as a function of calcification area of arterial wall, calcification intensity and calcification score. The 2-tissue compartmental model was used with blood time activity curve extracted directly from the images and from decomposed blood images using factor analysis. Additionally, we used modified FDG model without a need of blood sampling and unaffected by partial volume effect. We concluded that the modified ^{18}F-FDG model was used without the knowledge of a common input function and simultaneously eliminated the need of partial volume correction. This model was shown to be comparable to the classical ^{18}F-FDG model. For atherosclerosis, higher area of artery calcification and calcification score depending on calcification intensity and area were shown to affect glucose metabolism in the arteries. The correlation of glucose metabolism with the combination of calcification area and intensity could be an indicator of plaque vulnerability.

The third objective was to investigate the sensitivity of CT imaging in identifying the non-calcified plaque (NCP) in the combination with ^{18}F-FDG PET images. In this work, we still used the arterial wall for aorta and iliac arteries, and we have analysed the mostly repeated cut-off value in the literature for NCP and correlated it with the metabolic activity of glucose

(MRG). We concluded that NCP could be identified with CT images with density below 50 HU with an excellent correlation with its metabolic activity seen with ^{18}F-FDG PET. NCP and high calcification area were accompanied with a statistically high metabolic activity. Medication against artery inflammation was clearly shown to reduce NCP metabolism.

The fourth objective was concerning the use of ^{18}F-NaF tracer for tracking NCP in the combination with CT and contrast enhanced CT images for five volunteers. We also carried-out the analysis of ^{18}F-NaF uptake as a function of calcification density, area and scores. The measured ^{18}F-NaF images were corrected for blood pool activity and partial volume effect. We concluded that ^{18}F-NaF uptake is a marker able to measure the calcification activity. There was a reverse correlation of calcification area observed on CT images versus ^{18}F-NaF uptake. There was an increase in ^{18}F-NaF uptake with areas of spotty calcifications. NCP ($\leq$ 50 HU of the arterial wall) identified on CT images was correlated with significant ^{18}F-NaF uptake. A cut-off value of TBR from 2.5 to 2.6 may reflect active osteogenesis region. Further studies need to be carried out in order to validate the findings in the current work.

Other findings in this work suggests that in order to detect an active artery plaque (vulnerable plaque), it is recommended to consider the plaques individually in the same artery segment concurrently using CT and PET images.

Continuous efforts are required to validate the methods and cut-off values we provided in this thesis. Other promising radiotracer apart from the popular ^{18}F-FDG is ^{18}F-FCH which shows strong correlation to macrophage infiltration (Vöö *et al.*, 2016) and may be more specific to macrophages infiltration than ^{18}F-FDG along with ^{68}Ga-DOTATATE (Tarkin *et al.*, 2017). These tracers require more investigations and may provide new insight for quantifying plaque inflammation more precisely with high specificity. ^{18}F-fluciclatide is another promising tracer for targeting integrin $\alpha_v\beta_3$ with a need of validation in a large collaborative study as a next translational step to bring it closer to its clinical application in atherosclerosis.

Recently, anti-inflammatory therapy targeting the IL-1β innate immunity pathway with canakinumab was shown to significantly reduce the rate of recurrent cardiovascular events independently of lipid-lowering therapy (Ridker *et al.*, 2017). Targeting IL-1β by developing a probe may be a tool towards vulnerable plaque identification.

Other targeting enzyme is MMPs such as MMP1 and MMP9, where their elevation is significantly related to vulnerable plaques (Müller *et al.*, 2014).

PET/MRI scanners have been developed and clinically utilized simultaneous or dual-modality imaging which could improve the sensitivity and specificity for diagnosing plaque stability and other plaque components with MRI contrast agents such as MPIO.

ACKNOWLEDGEMENT

11.   LIST OF REFERENCES

van 't Klooster, R. *et al.* (2012) "Automatic lumen and outer wall segmentation of the carotid artery using deformable three-dimensional models in MR angiography and vessel wall images," *Journal of Magnetic Resonance Imaging*. John Wiley & Sons, Ltd, 35(1), pp. 156–165. doi: 10.1002/jmri.22809.

Achenbach, S. (2008) "Can CT detect the vulnerable coronary plaque?," *International Journal of Cardiovascular Imaging*. Int J Cardiovasc Imaging, pp. 311–312. doi: 10.1007/s10554-007-9281-1.

Achenbach, S. *et al.* (2010) "Influence of slice thickness and reconstruction kernel on the computed tomographic attenuation of coronary atherosclerotic plaque," *Journal of Cardiovascular Computed Tomography*. J Cardiovasc Comput Tomogr, 4(2), pp. 110–115. doi: 10.1016/j.jcct.2010.01.013.

Agatston, A. S. *et al.* (1990) "Quantification of coronary artery calcium using ultrafast computed tomography," *Journal of the American College of Cardiology*. Journal of the American College of Cardiology, 15(4), pp. 827–832. doi: 10.1016/0735-1097(90)90282-T.

Aikawa, E. *et al.* (2007) "Osteogenesis associates with inflammation in early-stage atherosclerosis evaluated by molecular imaging in vivo," *Circulation*. Circulation, 116(24), pp. 2841–2850. doi: 10.1161/CIRCULATIONAHA.107.732867.

Al-enezi, M. and Bentourkia, M. (2020) "Kinetic modeling of dynamic PET-18F-FDG atherosclerosis without blood sampling," *IEEE Transactions on Radiation and Plasma Medical Sciences*, pp. 1–1. doi: 10.1109/TRPMS.2020.3005364.

Al-enezi, M. S. *et al.* (2019) "Assessment of artery calcification in atherosclerosis with dynamic 18F-FDG-PET/CT imaging in elderly subjects," *International Journal of Cardiovascular Imaging*. Springer Netherlands, 35(5), pp. 947–954. doi: 10.1007/s10554-019-01527-7.

Anderson, J. D. and Kramer, C. M. (2007) "MRI of atherosclerosis: Diagnosis and monitoring therapy," *Expert Review of Cardiovascular Therapy*. Expert Rev Cardiovasc Ther, pp. 69–80. doi: 10.1586/14779072.5.1.69.

Bamberg, F. *et al.* (2011) "Meta-analysis and systematic review of the long-term predictive value of assessment of coronary atherosclerosis by contrast-enhanced coronary computed tomography angiography," *Journal of the American College of Cardiology*. Elsevier USA, 57(24), pp. 2426–2436. doi: 10.1016/j.jacc.2010.12.043.

Beltowski, J. (2006) "Leptin and atherosclerosis," *Atherosclerosis*. Elsevier Ireland Ltd, pp. 47–60. doi: 10.1016/j.atherosclerosis.2006.03.003.

Benjamin, E. J. *et al.* (2018) "Heart disease and stroke statistics - 2018 update: A report from the American Heart Association," *Circulation*. Lippincott Williams and Wilkins, 137(12), pp. E67–E492. doi: 10.1161/CIR.0000000000000558.

Benjamin, E. J. *et al.* (2019) "Heart Disease and Stroke Statistics-2019 Update: A Report From the American Heart Association," *Circulation*. NLM (Medline), 139(10), pp. e56–

e528. doi: 10.1161/CIR.0000000000000659.

Birukov, K. G. (2006) "Oxidized lipids: The two faces of vascular inflammation," *Current Atherosclerosis Reports*. Springer, pp. 223–231. doi: 10.1007/s11883-006-0077-x.

Blomberg, B. A. *et al.* (2017) "Thoracic aorta calcification but not inflammation is associated with increased cardiovascular disease risk: results of the CAMONA study," *European Journal of Nuclear Medicine and Molecular Imaging*. Springer Berlin, 44(2), pp. 249–258. doi: 10.1007/s00259-016-3552-9.

van den Bouwhuijsen, Q. J. A. *et al.* (2015) "Coexistence of Calcification, Intraplaque Hemorrhage and Lipid Core within the Asymptomatic Atherosclerotic Carotid Plaque: The Rotterdam Study," *Cerebrovascular Diseases*. S. Karger AG, 39(5–6), pp. 319–324. doi: 10.1159/000381138.

Bouziotis, P. *et al.* (2013) "Radiolabeled Iron Oxide Nanoparticles As Dual-Modality SPECT/MRI and PET/MRI Agents," *Current Topics in Medicinal Chemistry*. Bentham Science Publishers Ltd., 12(23), pp. 2694–2702. doi: 10.2174/1568026611212230007.

Brinjikji, W. *et al.* (2018) "Diagnostic accuracy of a clinical carotid plaque MR protocol using a neurovascular coil compared to a surface coil protocol," *Journal of Magnetic Resonance Imaging*. John Wiley and Sons Inc., 48(5), pp. 1264–1272. doi: 10.1002/jmri.25984.

Broisat, A. *et al.* (2014) "99mTc-cAbVCAM1-5 imaging is a sensitive and reproducible tool for the detection of inflamed atherosclerotic lesions in mice," *Journal of Nuclear Medicine*. Society of Nuclear Medicine Inc., 55(10), pp. 1678–1684. doi: 10.2967/jnumed.114.143792.

Brown, E. R. *et al.* (2008) "Coronary calcium coverage score: Determination, correlates, and predictive accuracy in the multi-ethnic study of atherosclerosis," *Radiology*. Radiology, 247(3), pp. 669–678. doi: 10.1148/radiol.2473071469.

Burgmaier, M. *et al.* (2018) "Co-localization of plaque macrophages with calcification is associated with a more vulnerable plaque phenotype and a greater calcification burden in coronary target segments as determined by OCT," *PLOS ONE*. Edited by E. Aikawa. Public Library of Science, 13(10), p. e0205984. doi: 10.1371/journal.pone.0205984.

Cademartiri, F. *et al.* (2007) "Influence of convolution filtering on coronary plaque attenuation values: Observations in an ex vivo model of multislice computed tomography coronary angiography," *European Radiology*. Springer, 17(7), pp. 1842–1849. doi: 10.1007/s00330-006-0548-z.

Callister, T. Q. *et al.* (1998) "Coronary artery disease: Improved reproducibility of calcium scoring with an electron-beam CT volumetric method," *Radiology*. Radiological Society of North America Inc., 208(3), pp. 807–814. doi: 10.1148/radiology.208.3.9722864.

Cassis, L. A. and Lodder, R. A. (1993) "Near-IR Imaging of Atheromas in Living Arterial Tissue," *Analytical Chemistry*. Anal Chem, 65(9), pp. 1247–1256. doi: 10.1021/ac00057a023.

Cheng, D. *et al.* (2015) "Detection of vulnerable atherosclerosis plaques with a dual-modal single-photon-emission computed tomography/magnetic resonance imaging probe targeting apoptotic macrophages," *ACS Applied Materials and Interfaces*. American Chemical Society, 7(4), pp. 2847–2855. doi: 10.1021/am508118x.

Choudhury, R. P. and Fisher, E. A. (2009) "Molecular imaging in atherosclerosis, thrombosis, and vascular inflammation," *Arteriosclerosis, Thrombosis, and Vascular Biology*. Lippincott Williams & Wilkins, pp. 983–991. doi: 10.1161/ATVBAHA.108.165498.

Corti, R. and Fuster, V. (2011) "Imaging of atherosclerosis: Magnetic resonance imaging," *European Heart Journal*. Oxford Academic, 32(14), pp. 1709–1719. doi: 10.1093/eurheartj/ehr068.

Criqui, M. H. *et al.* (2014) "Calcium Density of Coronary Artery Plaque and Risk of Incident Cardiovascular Events," *JAMA*, 311(3), p. 271. doi: 10.1001/jama.2013.282535.

Croteau, E. *et al.* (2010) "Image-derived input function in dynamic human PET/CT: Methodology and validation with 11C-acetate and 18F- fluorothioheptadecanoic acid in muscle and 18F-fluorodeoxyglucose in brain," *European Journal of Nuclear Medicine and Molecular Imaging*. Springer Verlag, 37(8), pp. 1539–1550. doi: 10.1007/s00259-010-1443-z.

Dalager, M. G., Bøttcher, M., Dalager, S., *et al.* (2011) "Imaging atherosclerotic plaques by cardiac computed tomography in vitro: Impact of contrast type and acquisition protocol," *Investigative Radiology*. Invest Radiol, 46(12), pp. 790–795. doi: 10.1097/RLI.0b013e31822b122e.

Dalager, M. G., Bøttcher, M., Andersen, G., *et al.* (2011) "Impact of luminal density on plaque classification by CT coronary angiography," *International Journal of Cardiovascular Imaging*, 27(4), pp. 593–600. doi: 10.1007/s10554-010-9695-z.

Dalm, V. A. S. H. *et al.* (2003) "Expression of somatostatin, cortistatin, and somatostatin receptors in human monocytes, macrophages, and dendritic cells," *American Journal of Physiology - Endocrinology and Metabolism*. American Physiological Society, 285(2 48-2). doi: 10.1152/ajpendo.00048.2003.

Davies, M. K. and Eollman, A. (1996) "Leonardo da Vinci (1452-1519).," *Heart (British Cardiac Society)*. BMJ Publishing Group, 76(6), p. 464. doi: 10.1136/hrt.76.6.464.

Derlin, T. *et al.* (2010) "Feasibility of 18F-sodium fluoride PET/CT for imaging of atherosclerotic plaque," *Journal of Nuclear Medicine*. J Nucl Med, 51(6), pp. 862–865. doi: 10.2967/jnumed.110.076471.

Derlin, T., Habermann, C. R., *et al.* (2011) "Feasibility of 11C-acetate PET/CT for imaging of fatty acid synthesis in the atherosclerotic vessel wall," *Journal of Nuclear Medicine*. J Nucl Med, 52(12), pp. 1848–1854. doi: 10.2967/jnumed.111.095869.

Derlin, T., Wisotzki, C., *et al.* (2011) "In vivo imaging of mineral deposition in carotid plaque using 18F-sodium fluoride PET/CT: Correlation with atherogenic risk factors," *Journal of Nuclear Medicine*. Society of Nuclear Medicine, 52(3), pp. 362–368. doi: 10.2967/jnumed.110.081208.

Dong, Z. M. *et al.* (1998) "The combined role of P- and E-selectins in atherosclerosis," *Journal of Clinical Investigation*. American Society for Clinical Investigation, 102(1), pp. 145–152. doi: 10.1172/JCI3001.

Dubey, L. *et al.* (2008) "Association of plasma leptin levels and complexity of the culprit lesion in patients with unstable angina," *International Journal of Cardiology*. Elsevier, 126(2), pp. 183–189. doi: 10.1016/j.ijcard.2007.03.126.

DuRose, J. B. *et al.* (2012) "Infection of Vascular Endothelial Cells with Human Cytomegalovirus under Fluid Shear Stress Reveals Preferential Entry and Spread of Virus in Flow Conditions Simulating Atheroprone Regions of the Artery," *Journal of Virology*. American Society for Microbiology, 86(24), pp. 13745–13755. doi: 10.1128/jvi.02244-12.

Dweck, M. R. *et al.* (2016) "Noninvasive Molecular Imaging of Disease Activity in Atherosclerosis," *Circulation Research*. Wolters Kluwer Health, 119(2), p. 330. doi: 10.1161/CIRCRESAHA.116.307971.

Ehara, S. *et al.* (2004) "Spotty calcification typifies the culprit plaque in patients with acute myocardial infarction: An intravascular ultrasound study," *Circulation*. Lippincott Williams & Wilkins, 110(22), pp. 3424–3429. doi: 10.1161/01.CIR.0000148131.41425.E9.

Ekmekci, H. and Ekmekci, O. B. (2006) "The Role of Adiponectin in Atherosclerosis and Thrombosis," *Clinical and Applied Thrombosis/Hemostasis*. Sage PublicationsSage CA: Thousand Oaks, CA, 12(2), pp. 163–168. doi: 10.1177/107602960601200203.

Eltoft, A. *et al.* (2018) "Interleukin-6 is an independent predictor of progressive atherosclerosis in the carotid artery: The Tromsø Study," *Atherosclerosis*. Elsevier Ireland Ltd, 271, pp. 1–8. doi: 10.1016/j.atherosclerosis.2018.02.005.

Erlandsson, K. *et al.* (2012) "A review of partial volume correction techniques for emission tomography and their applications in neurology, cardiology and oncology," *Physics in Medicine and Biology*. Phys Med Biol. doi: 10.1088/0031-9155/57/21/R119.

Evans, N. R. *et al.* (2016) "PET Imaging of Atherosclerotic Disease: Advancing Plaque Assessment from Anatomy to Pathophysiology," *Current Atherosclerosis Reports*. Current Medicine Group LLC 1. doi: 10.1007/s11883-016-0584-3.

Falk, E., Shah, P. K. and Fuster, V. (1995) "Coronary Plaque Disruption," *Circulation*. Lippincott Williams and Wilkins, 92(3), pp. 657–671. doi: 10.1161/01.CIR.92.3.657.

Fiz, F. *et al.* (2015) "18F-NaF uptake by atherosclerotic plaque on PET/CT imaging: Inverse correlation between calcification density and mineral metabolic activity," *Journal of Nuclear Medicine*. Society of Nuclear Medicine Inc., 56(7), pp. 1019–1023. doi: 10.2967/jnumed.115.154229.

Fowkes, F. G. R. *et al.* (1992) "Fibrinogen genotype and risk of peripheral atherosclerosis," *The Lancet*. Elsevier, 339(8795), pp. 693–696. doi: 10.1016/0140-6736(92)90596-U.

Freedman, N. M. T. *et al.* (2003) "Comparison of SUV and Patlak slope for monitoring of cancer therapy using serial PET scans," *European Journal of Nuclear Medicine and*

Molecular Imaging. Eur J Nucl Med Mol Imaging, 30(1), pp. 46–53. doi: 10.1007/s00259-002-0981-4.

Fujii, K. *et al.* (2005) "Intravascular ultrasound study of patterns of calcium in ruptured coronary plaques," *American Journal of Cardiology*. Excerpta Medica, 96(3), pp. 352–357. doi: 10.1016/j.amjcard.2005.03.074.

Fujii, K. *et al.* (2015) "Accuracy of OCT, grayscale IVUS, and their combination for the diagnosis of coronary TCFA: An ex vivo validation study," *JACC: Cardiovascular Imaging*. Elsevier Inc., 8(4), pp. 451–460. doi: 10.1016/j.jcmg.2014.10.015.

Garcia-Garcia, H. M., Costa, M. A. and Serruys, P. W. (2010) "Imaging of coronary atherosclerosis: Intravascular ultrasound," *European Heart Journal*. Eur Heart J. doi: 10.1093/eurheartj/ehq280.

Gjedde, A. (1982) "Calculation of cerebral glucose phosphorylation from brain uptake of glucose analogs in vivo: A re-examination," *Brain Research Reviews*. Brain Res, pp. 237–274. doi: 10.1016/0165-0173(82)90018-2.

Glagov, S. *et al.* (1987) "Compensatory Enlargement of Human Atherosclerotic Coronary Arteries," *New England Journal of Medicine*, 316(22), pp. 1371–1375. doi: 10.1056/NEJM198705283162204.

Glaudemans, A. W. J. M. *et al.* (2014) "In vivo and in vitro evidence that 99mTc-HYNIC-interleukin-2 is able to detect T lymphocytes in vulnerable atherosclerotic plaques of the carotid artery," *European Journal of Nuclear Medicine and Molecular Imaging*. Springer Verlag, 41(9), pp. 1710–1719. doi: 10.1007/s00259-014-2764-0.

Goldstein, J. L. and Brown, M. S. (2015) "A century of cholesterol and coronaries: From plaques to genes to statins," *Cell*. Cell Press, pp. 161–172. doi: 10.1016/j.cell.2015.01.036.

Hamdan, A. *et al.* (2011) "A prospective study for comparison of MR and CT imaging for detection of coronary artery stenosis," *JACC: Cardiovascular Imaging*. JACC: Cardiovascular Imaging, 4(1), pp. 50–61. doi: 10.1016/j.jcmg.2010.10.007.

Hill, M. D., Demchuk, A. M. and Frayne, R. (2007) "Noninvasive imaging is improving but digital subtraction angiography remains the gold standard," *Neurology*. Wolters Kluwer Health, Inc. on behalf of the American Academy of Neurology, pp. 2057–2058. doi: 10.1212/01.wnl.0000268580.86336.af.

Hoffman, E. J., Huang, S. C. and Phelps, M. E. (1979) "Quantitation in positron emission computed tomography: 1. effect of object size," *Journal of Computer Assisted Tomography*. J Comput Assist Tomogr, 3(3), pp. 299–308. doi: 10.1097/00004728-197906000-00001.

Høilund-Carlsen, P. F. *et al.* (2019) "Evolving Role of PET in Detecting and Characterizing Atherosclerosis," *PET Clinics*. W.B. Saunders, pp. 197–209. doi: 10.1016/j.cpet.2018.12.001.

Høilund-Carlsen, P. F. *et al.* (2020) "Atherosclerosis imaging with 18F-sodium fluoride PET: state-of-the-art review," *European Journal of Nuclear Medicine and Molecular Imaging*. Springer, pp. 1538–1551. doi: 10.1007/s00259-019-04603-1.

Hong, C. *et al.* (2002) "Coronary artery calcium: Absolute quantification in nonenhanced and contrast-enhanced multi-detector row CT studies," *Radiology*. Radiological Society of North America Inc., 223(2), pp. 474–480. doi: 10.1148/radiol.2232010919.

Hori, S. *et al.* (2019) "Correlation Between Cerebral Microbleeds and Vulnerable Plaque in Patients with Severe Carotid Artery Stenosis; Comparative Magnetic Resonance Imaging Study," *Journal of Stroke and Cerebrovascular Diseases*. W.B. Saunders, 28(10). doi: 10.1016/j.jstrokecerebrovasdis.2019.07.016.

Horiguchi, J. *et al.* (2011) "In vitro measurement of CT density and estimation of stenosis related to coronary soft plaque at 100 kV and 120 kV on ECG-triggered scan," *European Journal of Radiology*. Elsevier, 77(2), pp. 294–298. doi: 10.1016/j.ejrad.2009.08.002.

Howarth, S. P. S. *et al.* (2009) "Utility of USPIO-enhanced MR imaging to identify inflammation and the fibrous cap: A comparison of symptomatic and asymptomatic individuals," *European Journal of Radiology*. Eur J Radiol, 70(3), pp. 555–560. doi: 10.1016/j.ejrad.2008.01.047.

Hwang, J. J. *et al.* (2009) "Association of circulating matrix metalloproteinase-1, but not adiponectin, with advanced coronary artery disease," *Atherosclerosis*. Elsevier, 204(1), pp. 293–297. doi: 10.1016/j.atherosclerosis.2008.08.019.

Ishino, S. *et al.* (2014) "18F-FDG PET and intravascular ultrasonography (IVUS) images compared with histology of atherosclerotic plaques: 18F-FDG accumulates in foamy macrophages," *European Journal of Nuclear Medicine and Molecular Imaging*. Springer Verlag, 41(4), pp. 624–633. doi: 10.1007/s00259-013-2635-0.

Ishizu, K. *et al.* (1994) "Effects of hyperglycemia on FDG uptake in human brain and glioma," *Journal of Nuclear Medicine*, 35(7), pp. 1104–1109. Available at: https://europepmc.org/article/med/8014665 (Accessed: September 26, 2020).

Jager, N. A. *et al.* (2014) "Folate receptor-β imaging using 99mTc-folate to explore distribution of polarized macrophage populations in human atherosclerotic plaque," *Journal of Nuclear Medicine*. Society of Nuclear Medicine Inc., 55(12), pp. 1945–1951. doi: 10.2967/jnumed.114.143180.

Joshi, N. V. *et al.* (2014) "18F-fluoride positron emission tomography for identification of ruptured and high-risk coronary atherosclerotic plaques: A prospective clinical trial," *The Lancet*. Lancet Publishing Group, 383(9918), pp. 705–713. doi: 10.1016/S0140-6736(13)61754-7.

Kang, S. J. *et al.* (2015) "Combined IVUS and NIRS detection of fibroatheromas: Histopathological validation in human coronary arteries," *JACC: Cardiovascular Imaging*. Elsevier Inc., 8(2), pp. 184–194. doi: 10.1016/j.jcmg.2014.09.021.

Kannel, W. B., McGee, D. and Gordon, T. (1976) "A general cardiovascular risk profile: The Framingham study," *The American Journal of Cardiology*. Am J Cardiol, 38(1), pp. 46–51. doi: 10.1016/0002-9149(76)90061-8.

Kataoka, Y. *et al.* (2014) "Spotty calcification and plaque vulnerability in vivo: frequency-domain optical coherence tomography analysis.," *Cardiovascular diagnosis and therapy*. AME Publications, 4(6), pp. 460–469. doi: 10.3978/j.issn.2223-

3652.2014.11.06.

Kelly P and Bhatt DL (2007) "Identification of vulnerable plaque--the quest continues.," *J Invasive Cardiol.*, 19(2), pp. 55–7. Available at: https://pubmed.ncbi.nlm.nih.gov/17268037/ (Accessed: September 24, 2020).

Kemerink, G. J. *et al.* (2003) "Safety, biodistribution, and dosimetry of 99mTc-HYNIC-Annexin V, a novel human recombinant annexin V for human application," *Journal of Nuclear Medicine*, 44(6), pp. 947–952. Available at: http://jnm.snmjournals.org/cgi/content/full/44/6/947 (Accessed: September 25, 2020).

Kim, J. H. *et al.* (2017) "Total and differential WBC counts are related with coronary artery atherosclerosis and increase the risk for cardiovascular disease in Koreans," *PLoS ONE*. Public Library of Science, 12(7). doi: 10.1371/journal.pone.0180332.

Kitagawa, T. *et al.* (2017) "Data on analysis of coronary atherosclerosis on computed tomography and 18F-sodium fluoride positron emission tomography," *Data in Brief*. Elsevier Inc., 13, pp. 341–345. doi: 10.1016/j.dib.2017.06.011.

Kohichi, K. *et al.* (1985) "Significance of adventitial inflammation of the coronary artery in patients with unstable angina: results at autopsy," *Circulation*. Circulation, 71(4), pp. 709–716. doi: 10.1161/01.cir.71.4.709.

Kolodgie, F. D. *et al.* (2003) "Targeting of Apoptotic Macrophages and Experimental Atheroma with Radiolabeled Annexin V: A Technique with Potential for Noninvasive Imaging of Vulnerable Plaque," *Circulation*. Lippincott Williams & Wilkins, 108(25), pp. 3134–3139. doi: 10.1161/01.CIR.0000105761.00573.50.

Konstantinov, I. E., Mejevoi, N. and Anichkov, N. M. (2006) "Nikolai N. Anichkov and his theory of atherosclerosis," *Texas Heart Institute Journal*. Texas Heart Institute, pp. 417–423. Available at: /pmc/articles/PMC1764970/?report=abstract (Accessed: September 25, 2020).

Kotasidis, F. A., Tsoumpas, C. and Rahmim, A. (2014) "Advanced kinetic modelling strategies: Towards adoption in clinical PET imaging," *Clinical and Translational Imaging*. Springer-Verlag Italia s.r.l., pp. 219–237. doi: 10.1007/s40336-014-0069-8.

Kuku, K. O. *et al.* (2020) "Near-Infrared Spectroscopy Intravascular Ultrasound Imaging: State of the Art," *Frontiers in Cardiovascular Medicine*. Frontiers, 7, p. 107. doi: 10.3389/fcvm.2020.00107.

Lee, J. R. *et al.* (2000) "A threshold method to improve standardized uptake value reproducibility," *Nuclear Medicine Communications*. Nucl Med Commun, pp. 685–690. doi: 10.1097/00006231-200007000-00013.

Lewis, A. J. M., Burrage, M. K. and Ferreira, V. M. (2020) "Cardiovascular magnetic resonance imaging for inflammatory heart diseases," *Cardiovascular Diagnosis and Therapy*. AME Publishing Company, pp. 598–609. doi: 10.21037/cdt.2019.12.09.

Li, Q. *et al.* (2015) "The association between serum uric acid levels and the prevalence of vulnerable atherosclerotic carotid plaque: A cross-sectional study," *Scientific Reports*. Nature Publishing Group, 5. doi: 10.1038/srep10003.

Li, S. *et al.* (1996) "Three-dimensional mapping of the static magnetic field inside the

human head," *Magnetic Resonance in Medicine*, 36(5), pp. 705–714. doi: 10.1002/mrm.1910360509.

Li, X. *et al.* (2012) "68Ga-DOTATATE PET/CT for the detection of inflammation of large arteries: Correlation with 18F-FDG, calcium burden and risk factors," *EJNMMI Research*. Springer Verlag, 2(1), pp. 1–10. doi: 10.1186/2191-219X-2-52.

Li, X. *et al.* (2016) "Gold nanoparticles-based SPECT/CT imaging probe targeting for vulnerable atherosclerosis plaques," *Biomaterials*. Elsevier Ltd, 108, pp. 71–80. doi: 10.1016/j.biomaterials.2016.08.048.

Liew, S. M., Doust, J. and Glasziou, P. (2011) "Cardiovascular risk scores do not account for the effect of treatment: A review," *Heart*. BMJ Publishing Group Ltd, pp. 689–697. doi: 10.1136/hrt.2010.220442.

Lind, L. (2003) "Circulating markers of inflammation and atherosclerosis," *Atherosclerosis*. Elsevier Ireland Ltd, 169(2), pp. 203–214. doi: 10.1016/S0021-9150(03)00012-1.

Linton, M. F. *et al.* (1950) "The Role of Lipids and Lipoproteins in Atherosclerosis," *Science*. MDText.com, Inc. Available at: http://www.ncbi.nlm.nih.gov/pubmed/26844337 (Accessed: September 24, 2020).

Littlewood, T. D. and Bennett, M. R. (2003) "Apoptotic cell death in atherosclerosis," *Current Opinion in Lipidology*. Curr Opin Lipidol, pp. 469–475. doi: 10.1097/00041433-200310000-00007.

Liu, C. *et al.* (2016) "SPECT and fluorescence imaging of vulnerable atherosclerotic plaque with a vascular cell adhesion molecule 1 single-chain antibody fragment," *Atherosclerosis*. Elsevier Ireland Ltd, 254, pp. 263–270. doi: 10.1016/j.atherosclerosis.2016.09.005.

Lo, J. *et al.* (2015) "Effects of statin therapy on coronary artery plaque volume and high-risk plaque morphology in HIV-infected patients with subclinical atherosclerosis: A randomised, double-blind, placebo-controlled trial," *The Lancet HIV*. Elsevier Ltd, 2(2), pp. e52–e63. doi: 10.1016/S2352-3018(14)00032-0.

Logan, J. *et al.* (1990) "Graphical analysis of reversible radioligand binding from time-activity measurements applied to [N-11C-methyl]-(-)-cocaine PET studies in human subjects," *Journal of Cerebral Blood Flow and Metabolism*. Lippincott Williams and Wilkins, 10(5), pp. 740–747. doi: 10.1038/jcbfm.1990.127.

Madder, R. D., Abbas, A. E. and Safian, R. D. (2015) "First-in-man use of intravascular near-infrared spectroscopy in the carotid arteries to characterize atherosclerotic plaque prior to carotid stenting," *JACC: Cardiovascular Interventions*. Elsevier Inc., 8(2), pp. e29–e31. doi: 10.1016/j.jcin.2013.11.029.

Makowski, M. R. *et al.* (2013) "Characterization of coronary atherosclerosis by magnetic resonance imaging," *Circulation*. Lippincott Williams & WilkinsHagerstown, MD, pp. 1244–1255. doi: 10.1161/CIRCULATIONAHA.113.002681.

Malguria, N., Zimmerman, S. and Fishman, E. K. (2018) "Coronary Artery Calcium Scoring: Current Status and Review of Literature," *Journal of Computer Assisted*

Tomography. Lippincott Williams and Wilkins, 42(6), pp. 887–897. doi: 10.1097/RCT.0000000000000825.

Malmberg, C. *et al.* (2015) "64Cu-DOTATATE for noninvasive assessment of atherosclerosis in large arteries and its correlation with risk factors: Head-to-head comparison with 68Ga-DOTATOC in 60 patients," *Journal of Nuclear Medicine*. Society of Nuclear Medicine Inc., 56(12), pp. 1895–1900. doi: 10.2967/jnumed.115.161216.

Manfrini, O. *et al.* (2006) "Sources of Error and Interpretation of Plaque Morphology by Optical Coherence Tomography," *American Journal of Cardiology*. Elsevier Inc., 98(2), pp. 156–159. doi: 10.1016/j.amjcard.2006.01.097.

Marwan, M. *et al.* (2011) "In vivo CT detection of lipid-rich coronary artery atherosclerotic plaques using quantitative histogram analysis: A head to head comparison with IVUS," *Atherosclerosis*. Atherosclerosis, 215(1), pp. 110–115. doi: 10.1016/j.atherosclerosis.2010.12.006.

Mathers, C. *et al.* (2018) *Global Health Estimates 2016: Deaths by Cause, Age, Sex, by Country and by Region*. Geneva. Available at: https://terrance.who.int/mediacentre/data/ghe/GlobalCOD_method_2000_2016.pdf (Accessed: January 1, 2021).

Matter, C. M. *et al.* (2006) "18F-choline images murine atherosclerotic plaques ex vivo," *Arteriosclerosis, Thrombosis, and Vascular Biology*. Lippincott Williams & Wilkins, 26(3), pp. 584–589. doi: 10.1161/01.ATV.0000200106.34016.18.

Maurovich-Horvat, P. *et al.* (2012) "The napkin-ring sign indicates advanced atherosclerotic lesions in coronary CT angiography," *JACC: Cardiovascular Imaging*. JACC Cardiovasc Imaging, 5(12), pp. 1243–1252. doi: 10.1016/j.jcmg.2012.03.019.

Maurovich-Horvat, P. *et al.* (2014) "Comprehensive plaque assessment by coronary CT angiography," *Nature Reviews Cardiology*. Nature Publishing Group, pp. 390–402. doi: 10.1038/nrcardio.2014.60.

Mayerl, C. *et al.* (2006) "Atherosclerosis research from past to present - On the track of two pathologists with opposing views, Carl von Rokitansky and Rudolf Virchow," *Virchows Archiv*. Springer, 449(1), pp. 96–103. doi: 10.1007/s00428-006-0176-7.

Meester, E. J. *et al.* (2020) "Imaging inflammation in atherosclerotic plaques, targeting SST2 with [111In]In-DOTA-JR11," *Journal of Nuclear Cardiology*. Springer, pp. 1–8. doi: 10.1007/s12350-020-02046-y.

Meyer, O. (2001) "Atherosclerosis and connective tissue diseases," *Joint Bone Spine*. Elsevier Masson SAS, 68(6), pp. 564–575. doi: 10.1016/S1297-319X(01)00330-X.

Michel, J. B. *et al.* (2014) "Pathology of human plaque vulnerability: Mechanisms and consequences of intraplaque haemorrhages," *Atherosclerosis*. Elsevier Ireland Ltd, pp. 311–319. doi: 10.1016/j.atherosclerosis.2014.03.020.

Mistretta, C. A. and Crummy, A. B. (1986) "Basic concepts of digital angiography," *Progress in Cardiovascular Diseases*. Prog Cardiovasc Dis, 28(4), pp. 245–255. doi: 10.1016/0033-0620(86)90001-0.

Mizukoshi, M. *et al.* (2013) "Coronary superficial and spotty calcium deposits in culprit coronary lesions of acute coronary syndrome as determined by optical coherence tomography," in *American Journal of Cardiology*. Am J Cardiol, pp. 34–40. doi: 10.1016/j.amjcard.2013.02.048.

Mori, Y. *et al.* (2016) "Magnetic resonance imaging (MRI) and magnetic resonance spectroscopy (MRS)," in *Cognitive Neuroscience Robotics B: Analytic Approaches to Human Understanding*. Springer Japan, pp. 147–170. doi: 10.1007/978-4-431-54598-9_7.

Morishige, K. *et al.* (2010) "High-resolution magnetic resonance imaging enhanced with superparamagnetic nanoparticles measures macrophage burden in atherosclerosis," *Circulation*. Lippincott Williams & WilkinsHagerstown, MD, 122(17), pp. 1707–1715. doi: 10.1161/CIRCULATIONAHA.109.891804.

Moss, A. J. *et al.* (2019) "Molecular coronary plaque imaging using 18f-fluoride," *Circulation: Cardiovascular Imaging*. Lippincott Williams and Wilkins, 12(8). doi: 10.1161/CIRCIMAGING.118.008574.

Motoyama, S. *et al.* (2007) "Multislice Computed Tomographic Characteristics of Coronary Lesions in Acute Coronary Syndromes," *Journal of the American College of Cardiology*. Journal of the American College of Cardiology, 50(4), pp. 319–326. doi: 10.1016/j.jacc.2007.03.044.

Müller, A. *et al.* (2014) "Gene expression levels of matrix metalloproteinases in human atherosclerotic plaques and evaluation of radiolabeled inhibitors as imaging agents for plaque vulnerability," *Nuclear Medicine and Biology*. Elsevier Inc., 41(7), pp. 562–569. doi: 10.1016/j.nucmedbio.2014.04.085.

Muller, J. E., Tofler, G. H. and Stone, P. H. (1989) "Circadian variation and triggers of onset of acute cardiovascular disease," *Circulation*. Circulation, pp. 733–743. doi: 10.1161/01.CIR.79.4.733.

Naghavi, M. *et al.* (2003) "From Vulnerable Plaque to Vulnerable Patient: A Call for New Definitions and Risk Assessment Strategies: Part II," *Circulation*. Lippincott Williams & Wilkins, pp. 1772–1778. doi: 10.1161/01.CIR.0000087481.55887.C9.

Narula, J. *et al.* (2013) "Histopathologic characteristics of atherosclerotic coronary disease and implications of the findings for the invasive and noninvasive detection of vulnerable plaques," *Journal of the American College of Cardiology*. J Am Coll Cardiol, 61(10), pp. 1041–1051. doi: 10.1016/j.jacc.2012.10.054.

Nasir, K. *et al.* (2004) "Coronary artery calcium volume scores on electron beam tomography in 12,936 asymptomatic adults," *American Journal of Cardiology*. Elsevier Inc., 93(9), pp. 1146–1149. doi: 10.1016/j.amjcard.2004.01.043.

Nerlekar, N. *et al.* (2018) "Computed Tomographic Coronary Angiography-Derived Plaque Characteristics Predict Major Adverse Cardiovascular Events: A Systematic Review and Meta-Analysis," *Circulation. Cardiovascular imaging*. NLM (Medline), 11(1), p. e006973. doi: 10.1161/CIRCIMAGING.117.006973.

Newby, A. C. (2005) "Dual role of matrix metalloproteinases (matrixins) in intimal

thickening and atherosclerotic plaque rupture," *Physiological Reviews*. Physiol Rev, pp. 1–31. doi: 10.1152/physrev.00048.2003.

Noguchi, T. *et al.* (2018) "Noninvasive coronary plaque imaging," *Journal of Atherosclerosis and Thrombosis*. Japan Atherosclerosis Society, pp. 281–293. doi: 10.5551/jat.RV17019.

Okuda, K. *et al.* (2021) "Multicenter study of quantitative SPECT imaging: reproducibility of 99mTc quantitation using a conjugated gradient minimization reconstruction algorithm.," *Journal of nuclear medicine technology*. Society of Nuclear Medicine. doi: 10.2967/jnmt.120.256131.

Pasterkamp, G. *et al.* (1998) "Relation of arterial geometry to luminal narrowing and histologic markers for plaque vulnerability: The remodeling paradox," *Journal of the American College of Cardiology*. J Am Coll Cardiol, 32(3), pp. 655–662. doi: 10.1016/S0735-1097(98)00304-0.

Patel, S. G. *et al.* (2002) "Outcome, observer reliability, and patient preferences if CTA, MRA, or Doppler ultrasound were used, individually or together, instead of digital subtraction angiography before carotid endarterectomy," *Journal of Neurology Neurosurgery and Psychiatry*. J Neurol Neurosurg Psychiatry, 73(1), pp. 21–28. doi: 10.1136/jnnp.73.1.21.

Phelps, M. E. *et al.* (1979) "Tomographic measurement of local cerebral glucose metabolic rate in humans with (F-18)2-fluoro-2-deoxy-D-glucose: Validation of method," *Annals of Neurology*. John Wiley & Sons, Ltd, 6(5), pp. 371–388. doi: 10.1002/ana.410060502.

Priester, T. C. and Litwin, S. E. (2009) "Measuring Progression of Coronary Atherosclerosis with Computed Tomography: Searching for Clarity Among Shades of Gray," *Journal of Cardiovascular Computed Tomography*. J Cardiovasc Comput Tomogr. doi: 10.1016/j.jcct.2009.10.011.

Raffort, J. *et al.* (2017) "Monocytes and macrophages in abdominal aortic aneurysm," *Nature Reviews Cardiology*. Nature Publishing Group, pp. 457–471. doi: 10.1038/nrcardio.2017.52.

Ramachandra, C. J. A. *et al.* (2020) "Myeloperoxidase As a Multifaceted Target for Cardiovascular Protection," *Antioxidants and Redox Signaling*. Mary Ann Liebert Inc., pp. 1135–1149. doi: 10.1089/ars.2019.7971.

Richards, J. M. J. *et al.* (2011) "Abdominal aortic aneurysm growth predicted by uptake of ultrasmall superparamagnetic particles of Iron oxide : A pilot study," *Circulation: Cardiovascular Imaging*. Lippincott Williams & WilkinsHagerstown, MD, 4(3), pp. 274–281. doi: 10.1161/CIRCIMAGING.110.959866.

Ridker, P. M. *et al.* (2017) "Antiinflammatory Therapy with Canakinumab for Atherosclerotic Disease," *New England Journal of Medicine*. Massachussetts Medical Society, 377(12), pp. 1119–1131. doi: 10.1056/NEJMoa1707914.

Rojulpote, C. *et al.* (2020) "Role of 18F-NaF-PET in assessing aortic valve calcification with age.," *American journal of nuclear medicine and molecular imaging*. e-Century

Publishing Corporation, 10(1), pp. 47–56. Available at: http://www.ncbi.nlm.nih.gov/pubmed/32211218 (Accessed: September 25, 2020).

Rominger, A. *et al.* (2010) "In vivo imaging of macrophage activity in the coronary arteries using 68Ga-DOTATATE PET/CT: Correlation with coronary calcium burden and risk factors," *Journal of Nuclear Medicine*. Society of Nuclear Medicine, 51(2), pp. 193–197. doi: 10.2967/jnumed.109.070672.

Ronald Boellaard, P. *et al.* (2004) "Effects of Noise, Image Resolution, and ROI Definition on the Accuracy of Standard Uptake Values: A Simulation Study," *J Nucl Med.*, 45(9), pp. 1519–1527. Available at: http://jnm.snmjournals.org/content/45/9/1519.long (Accessed: September 25, 2020).

Ross, R. (1999) "Atherosclerosis - An inflammatory disease," *New England Journal of Medicine*. Edited by F. H. Epstein. Massachusetts Medical Society , pp. 115–126. doi: 10.1056/NEJM199901143400207.

Rudd, J. H. F. *et al.* (2002) "Imaging atherosclerotic plaque inflammation with [18F]-fluorodeoxyglucose positron emission tomography," *Circulation*. Circulation, 105(23), pp. 2708–2711. doi: 10.1161/01.CIR.0000020548.60110.76.

Rudd, J. H. F. *et al.* (2009) "Relationships among regional arterial inflammation, calcification, risk factors, and biomarkers: A prospective fluorodeoxyglucose positron-emission tomography/computed tomography imaging study," *Circulation: Cardiovascular Imaging*. Circ Cardiovasc Imaging, 2(2), pp. 107–115. doi: 10.1161/CIRCIMAGING.108.811752.

Rumberger, J. A. and Kaufman, L. (2003) "A rosetta stone for coronary calcium risk stratification: Agatston, volume, and mass scores in 11,490 individuals," *American Journal of Roentgenology*. American Roentgen Ray Society, 181(3), pp. 743–748. doi: 10.2214/ajr.181.3.1810743.

Rutland, M., Que, L. and Hassan, I. M. (2000) "'FUR' - One size suits all," *European Journal of Nuclear Medicine*. Springer, 27(11), pp. 1708–1713. doi: 10.1007/s002590000337.

Ruwanpathirana, T., Owen, A. and Reid, C. M. (2015) "Review on Cardiovascular Risk Prediction," *Cardiovascular Therapeutics*. Blackwell Publishing Ltd, 33(2), pp. 62–70. doi: 10.1111/1755-5922.12110.

Saba, L. *et al.* (2014) "Semiautomated analysis of carotid artery wall thickness in MRI," *Journal of Magnetic Resonance Imaging*. John Wiley and Sons Inc., 39(6), pp. 1457–1467. doi: 10.1002/jmri.24307.

Saba, L. *et al.* (2019) "CT and MR Imaging of Carotid Wall and Plaque," *Journal of Neurosonology and Neuroimaging*. Korean Society of Neurosonology, 11(2), pp. 115–125. doi: 10.31728/jnn.2019.00062.

Sadeghi, M. M. *et al.* (2010) "Imaging atherosclerosis and vulnerable plaque," *Journal of Nuclear Medicine*. NIH Public Access, p. 51S. doi: 10.2967/jnumed.109.068163.

De Saint-Hubert, M. *et al.* (2009) "Molecular imaging of cell death," *Methods*. Methods, pp. 178–187. doi: 10.1016/j.ymeth.2009.03.022.

Sakaguchi, M. *et al.* (2016) "New insights into spotty calcification and plaque rupture in acute coronary syndrome: an optical coherence tomography study," *Heart and Vessels*. Springer Tokyo, 31(12), pp. 1915–1922. doi: 10.1007/s00380-016-0820-3.

Sanduleanu, S. *et al.* (2020) "Hypoxia pet imaging with [18f]-hx4—a promising next-generation tracer," *Cancers*. MDPI AG. doi: 10.3390/cancers12051322.

Sarwar, N. *et al.* (2007) "Triglycerides and the risk of coronary heart disease: 10 158 Incident cases among 262 525 participants in 29 Western prospective studies," *Circulation*. Circulation, 115(4), pp. 450–458. doi: 10.1161/CIRCULATIONAHA.106.637793.

Satomi, T. *et al.* (2013) "Comparison of contrast agents for atherosclerosis imaging using cultured macrophages: FDG versus ultrasmall superparamagnetic iron oxide," *Journal of Nuclear Medicine*. Society of Nuclear Medicine, 54(6), pp. 999–1004. doi: 10.2967/jnumed.112.110551.

Schaar, J. A. *et al.* (2003) "Characterizing Vulnerable Plaque Features with Intravascular Elastography," *Circulation*. Circulation, 108(21), pp. 2636–2641. doi: 10.1161/01.CIR.0000097067.96619.1F.

Shepherd, P. R. and Kahn, B. B. (1999) "Glucose transporters and insulin action: Implications for insulin resistance and diabetes mellitus," *New England Journal of Medicine*. N Engl J Med, pp. 248–257. doi: 10.1056/NEJM199907223410406.

Shi, X. *et al.* (2020) "Calcification in Atherosclerotic Plaque Vulnerability: Friend or Foe?," *Frontiers in Physiology*. Frontiers Media S.A. doi: 10.3389/fphys.2020.00056.

Singh, S. K. *et al.* (2008) "The connection between C-reactive protein and atherosclerosis," *Annals of Medicine*. NIH Public Access, pp. 110–120. doi: 10.1080/07853890701749225.

Skeoch, S. and Bruce, I. N. (2015) "Atherosclerosis in rheumatoid arthritis: Is it all about inflammation?," *Nature Reviews Rheumatology*. Nature Publishing Group, pp. 390–400. doi: 10.1038/nrrheum.2015.40.

Slijkhuis, W., Mali, W. and Appelman, Y. (2009) "A historical perspective towards a non-invasive treatment for patients with atherosclerosis," *Netherlands Heart Journal*. Springer, pp. 140–144. doi: 10.1007/BF03086236.

Soret, M., Bacharach, S. L. and Buvat, I. (2007) "Partial-volume effect in PET tumor imaging," *Journal of Nuclear Medicine*. J Nucl Med, pp. 932–945. doi: 10.2967/jnumed.106.035774.

Srinivas, S. M. *et al.* (2009) "A recovery coefficient method for partial volume correction of PET images," *Annals of Nuclear Medicine*. Ann Nucl Med, 23(4), pp. 341–348. doi: 10.1007/s12149-009-0241-9.

Tabas, I., Williams, K. J. and Borén, J. (2007) "Subendothelial lipoprotein retention as the initiating process in atherosclerosis: Update and therapeutic implications," *Circulation*. Lippincott Williams & Wilkins, pp. 1832–1844. doi: 10.1161/CIRCULATIONAHA.106.676890.

Tarkin, J. M. *et al.* (2017) "Detection of Atherosclerotic Inflammation by 68Ga-

DOTATATE PET Compared to [18F]FDG PET Imaging," *Journal of the American College of Cardiology*. Elsevier USA, 69(14), pp. 1774–1791. doi: 10.1016/j.jacc.2017.01.060.

Tawakol, A. *et al.* (2006) "In Vivo 18F-Fluorodeoxyglucose Positron Emission Tomography Imaging Provides a Noninvasive Measure of Carotid Plaque Inflammation in Patients," *Journal of the American College of Cardiology*. J Am Coll Cardiol, 48(9), pp. 1818–1824. doi: 10.1016/j.jacc.2006.05.076.

Thilo, C. *et al.* (2011) "Can Non-calcified Coronary Artery Plaques Be Detected on Non-contrast CT Calcium Scoring Studies?," *Academic Radiology*. Acad Radiol, 18(7), pp. 858–865. doi: 10.1016/j.acra.2011.02.019.

Torzewski, M. *et al.* (2000) "C-reactive protein in the arterial intima: Role of C-reactive protein receptor-dependent monocyte recruitment in atherogenesis," *Arteriosclerosis, Thrombosis, and Vascular Biology*. Lippincott Williams and Wilkins, 20(9), pp. 2094–2099. doi: 10.1161/01.ATV.20.9.2094.

Trivedi, R. A. *et al.* (2006) "Identifying inflamed carotid plaques using in vivo USPIO-enhanced MR imaging to label plaque macrophages," *Arteriosclerosis, Thrombosis, and Vascular Biology*. Lippincott Williams & Wilkins, 26(7), pp. 1601–1606. doi: 10.1161/01.ATV.0000222920.59760.df.

Uetani, T. *et al.* (2010) "The Association Between Plaque Characterization by CT Angiography and Post-Procedural Myocardial Infarction in Patients With Elective Stent Implantation," *JACC: Cardiovascular Imaging*. JACC: Cardiovascular Imaging, 3(1), pp. 19–28. doi: 10.1016/j.jcmg.2009.09.016.

Ulzheimer, S. and Kalender, W. A. (2003) "Assessment of calcium scoring performance in cardiac computed tomography," *European Radiology*. Springer Verlag, pp. 484–497. doi: 10.1007/s00330-002-1746-y.

Van Der Valk, F. M. *et al.* (2015) "In vivo imaging of hypoxia in atherosclerotic plaques in humans," *JACC: Cardiovascular Imaging*. Elsevier Inc., pp. 1340–1341. doi: 10.1016/j.jcmg.2014.12.015.

Van Velzen, J. E. *et al.* (2011) "Comprehensive assessment of spotty calcifications on computed tomography angiography: Comparison to plaque characteristics on intravascular ultrasound with radiofrequency backscatter analysis," *Journal of Nuclear Cardiology*. J Nucl Cardiol, 18(5), pp. 893–903. doi: 10.1007/s12350-011-9428-2.

Vemulapalli, S. *et al.* (2007) "Cell therapy in murine atherosclerosis: In vivo imaging with high-resolution helical SPECT," *Radiology*. Radiology, 242(1), pp. 198–207. doi: 10.1148/radiol.2421051461.

Virmani, R. *et al.* (2006) "Pathology of the Vulnerable Plaque," *Journal of the American College of Cardiology*. J Am Coll Cardiol. doi: 10.1016/j.jacc.2005.10.065.

Vöö, S. *et al.* (2016) "Imaging intraplaque inflammation in carotid atherosclerosis with 18F-fluorocholine positron emission tomography-computed tomography," *Circulation: Cardiovascular Imaging*. Lippincott Williams and Wilkins, 9(5). doi: 10.1161/CIRCIMAGING.115.004467.

Westerlind, H. *et al.* (2019) "Siblings of patients with rheumatoid arthritis are at increased risk of acute coronary syndrome," *Annals of the Rheumatic Diseases*. BMJ Publishing Group, 78(5), pp. 683–687. doi: 10.1136/annrheumdis-2018-214828.

Williams, K. J. and Tabas, I. (1995) "The response-to-retention hypothesis of early atherogenesis," *Arteriosclerosis, Thrombosis, and Vascular Biology*. Lippincott Williams and Wilkins, pp. 551–562. doi: 10.1161/01.atv.15.5.551.

Williams, K. J. and Tabas, I. (1998) "The response-to-retention hypothesis of atherogenesis reinforced," *Current Opinion in Lipidology*. Curr Opin Lipidol, pp. 471–474. doi: 10.1097/00041433-199810000-00012.

Wu, H. *et al.* (2018) "Cysteine protease cathepsins in atherosclerotic cardiovascular diseases," *Journal of Atherosclerosis and Thrombosis*. Japan Atherosclerosis Society, pp. 111–123. doi: 10.5551/jat.RV17016.

Yia-Herttuala, S. *et al.* (1989) "Evidence for the presence of oxidatively modified low density lipoprotein in atherosclerotic lesions of rabbit and man," *Journal of Clinical Investigation*. American Society for Clinical Investigation, 84(4), pp. 1086–1095. doi: 10.1172/jci114271.

Yoo, J. S. *et al.* (2015) "SPECT/CT imaging of high-risk atherosclerotic plaques using integrin-binding RGD dimer peptides," *Scientific Reports*. Nature Publishing Group, 5(1), pp. 1–11. doi: 10.1038/srep11752.

Zhang, F. *et al.* (2019) "Spotty Calcium on Cervicocerebral Computed Tomography Angiography Associates With Increased Risk of Ischemic Stroke," *Stroke*. Lippincott Williams and Wilkins, 50(4), pp. 859–866. doi: 10.1161/STROKEAHA.118.023273.

Zhao, Y. *et al.* (2007) "Comparison of 99mTc-annexin A5 with 18F-FDG for the detection of atherosclerosis in ApoE−/− mice," *European Journal of Nuclear Medicine and Molecular Imaging*, 34(11), pp. 1747–1755. doi: 10.1007/s00259-007-0433-2.